

**ANALYTICAL AND FINITE ELEMENT SOLUTIONS FOR
AN ELASTIC MATRIX WITH TWO-DIMENSIONAL
NANOSCALE INHOMOGENEITIES**

By

Lian Tian

B. S., University of Science and Technology of China, P. R. China, 2003

**A THESIS SUBMITTED IN PARTIAL FULLFILLMENT OF
THE REQUIREMENTS FOR THE DEGREE OF**

MASTER OF APPLIED SCIENCE

in

**THE FACULTY OF GRADUATE STUDIES
(MECHANICAL ENGINEERING)**

THE UNIVERSITY OF BRITISH COLUMBIA

June 2006

© Lian Tian, 2006

Abstract

A new frontier of research at the interface of material science and mechanics of solids has emerged with the current focus on the development of nanomaterials such as nanotubes, nanowires and nanoparticles. As the dimensions of a structure approach the nanoscale, its properties can be size-dependent. The classical continuum theory, however, does not admit an intrinsic size, and is not applicable to the analysis of nanoscale materials and structures. Mechanics of nanomaterials-based composites can be understood by incorporating the effects of surface and interfacial energy. A fundamental problem in the study of behaviour of such materials is the examination of size-dependent elastic field of an elastic matrix with nanoscale inhomogeneities. Classical inhomogeneity problems have a rich history since the celebrated work of Eshelby. However, the classical solutions cannot be applied to study nanoscale inhomogeneity problems and new solutions accounting for surface/interface energy have to be derived.

This thesis therefore presents an analytical scheme and a finite element formulation to study the size-dependent elastic field of an elastic matrix containing two-dimensional nanoscale inhomogeneities. The Gurtin-Murdoch surface/interface elasticity model is applied to incorporate the surface/interface energy effects. By using the complex potential technique of Muskhelishvili, a closed-form analytical solution is obtained for the elastic field of a nanoscale circular inhomogeneity in an infinite matrix under arbitrary remote loading and a uniform eigenstrain. In the case of an elliptical inhomogeneity, the analytic potential functions are obtained approximately. A new finite element formulation that takes into account the surface stress effects is presented. Elastic field is found to depend on the characteristic dimensions of the inhomogeneity, surface elastic constants and surface residual stress. A striking feature of the new solutions is the existence of singular elastic fields below some dimensions of the inhomogeneity. This phenomenon requires careful further investigation. Eshelby tensor of a nanoscale circular inhomogeneity in an infinite matrix due to a uniform eigenstrain is uniform but becomes size-dependent; however, the tensor is size-dependent and non-uniform in the case of an elliptical inhomogeneity.

Table of Contents

Abstract	ii
Table of Contents	iii
List of Tables	v
List of Figures	vi
List of Symbols	x
Acknowledgements	xi
1. Introduction	1
1.1 Nanotechnology.....	1
1.2 Nanoscale Mechanics.....	3
1.3 Review of Surface Elasticity Model.....	5
1.4 Review of Classical and Modern Inhomogeneity Problems.....	10
1.5 Scope of the Current Work.....	11
2. Elastic Field of an Infinite Matrix with a Nanoscale Circular Inhomogeneity ...14	
2.1 Problem Description and Basic Equations.....	14
2.2 Formulation of Inhomogeneity Problem.....	15
2.3 Numerical Results for Elastic Field Around a Circular Hole.....	22
2.4 Numerical Results for Elastic Field of a Circular Inhomogeneity.....	29
3. Elastic Field of an Infinite Matrix with a Nanoscale Elliptical Inhomogeneity ...33	
3.1 Problem Description.....	33
3.2 Solution of Elastic Field.....	34
3.3 Numerical Results for Elastic Field Around an Elliptical Hole.....	42
3.4 Numerical Results for Elastic Field of an Elliptical Inhomogeneity.....	50
4. 2-D Finite Element Analysis of Nanoscale Inhomogeneity Problems56	
4.1 Finite Element Formulation.....	56
4.2 Finite Element Simulation of Inhomogeneity Problems.....	62
4.2.1 Elastic Field Around a Hole in a Finite Plate.....	62
4.2.2 Elastic Field of a Finite Plate with Two Circular Inhomogeneities.....	72
4.2.3 Elastic Field Around a Circular Hole in a Finite Anisotropic Plate.....	76
5. Summary and Conclusions	79

5.1 Summary and Major Findings.....	79
5.2 Suggestions for Future Work.....	81
Bibliography.....	83
Appendices.....	88
Appendix A.....	88
Appendix B.....	92
Appendix C.....	92
Appendix D.....	94

List of Tables

Table 2.1	Surface elastic constants. Units are N/m.....	22
-----------	---	----

List of Figures

Figure 1.1	Potential benefits of nanoscience & nanotechnology.....	3
Figure 2.1	A nanoscale circular inhomogeneity in an infinite matrix.....	14
Figure 2.2	Variation of stress concentration factor at $\theta = 0$	24
Figure 2.3	Nondimensional hoop stress along the hole surface ($R_0 = 5\text{nm}$).....	25
Figure 2.4	Nondimensional radial displacement along the hole surface.....	26
Figure 2.5	Variation of nondimensional hoop and radial stresses along the x_1 - direction for different K^S ($R_0 = 5\text{nm}$; $d=0$)	27
Figure 2.6	Variation of nondimensional hoop and radial stress components along the x_1 -direction for a hole with residual surface stress ($\tau^0 \neq 0$; $d=0$).....	29
Figure 2.7	Variation of nondimensional interfacial hoop stress at $\theta = 0$ with loading ratio or inhomogeneity radius (solid lines for matrix and dash lines for inhomogeneity).....	30
Figure 2.8	Nondimensional hoop stress along the inhomogeneity/matrix interface (solid lines for matrix and dash lines for inhomogeneity).....	31
Figure 2.9	Variation of nondimensional interfacial hoop stress due to an eigenstrain ε^* with inhomogeneity radius (solid lines and left Y-axis for matrix, and dash lines and right Y-axis for inhomogeneity).....	32
Figure 3.1	A nanoscale elliptical inhomogeneity in an infinite matrix.....	33
Figure 3.2	Conformal mapping from z-plane to ξ -plane.....	36
Figure 3.3	Variation of stress concentration factor at $\theta = 0$ with hole size R and K^S ($a/b=1.5$) under uniaxial loading $\sigma_{yy}^\infty = \sigma_0$	44
Figure 3.4	Variation of stress concentration factor at $\theta = 0$ with hole size R and K^S ($a/b=3$) under uniaxial loading $\sigma_{yy}^\infty = \sigma_0$	46
Figure 3.5	Variation of nondimensional tangential stress along the hole surface with $R=6\text{nm}$ ($a/b=1.5$).....	47
Figure 3.6	Variation of nondimensional normal displacement along the hole surface for different K^S ($a/b=1.5$; $R=6\text{nm}$).....	48

Figure 3.7	Variation of stress components, σ_{22} and σ_{11} , along the x_1 -direction for different K^S under uniaxial loading $\sigma_{yy}^\infty = \sigma_0$ ($a/b=1.5$; $R = 6\text{nm}$)...49
Figure 3.8	Variation of stress components, σ_{22} and σ_{11} , along the x_1 -direction for a hole with residual surface stress under uniaxial loading $\sigma_{yy}^\infty = \sigma_0$ ($a/b=1.5$; $\tau^0 \neq 0$).....50
Figure 3.9	Variation of the nondimensional tangential stress at $\theta = 0$ with the inhomogeneity size R and K^S ($a/b=1.5$) under uniaxial loading ($\sigma_{yy}^\infty = \sigma_0$): solid lines for matrix and dash lines for inhomogeneity.....51
Figure 3.10	Variation of the nondimensional tangential stress at $\theta = 0$ with the inhomogeneity size R and K^S ($a/b=3$) under uniaxial loading ($\sigma_{yy}^\infty = \sigma_0$): solid lines for matrix and dash lines for inhomogeneity.....52
Figure 3.11	Variation of nondimensional tangential stress along the interface with $R=5\text{nm}$ and $a/b=1.5$: solid lines for matrix and dash lines for inhomogeneity.....53
Figure 3.12	Variation of the nondimensional tangential stress at $\theta = 0$ on the interface with the inhomogeneity size R and K^S ($a/b=1.5$) under a uniform dilatational eigenstrain ε^* (solid lines for matrix and dash lines for inhomogeneity).....54
Figure 3.13	Variation of nondimensional strains along the interface in an inhomogeneity for different values of K^S and R under a uniform dilatational eigenstrain.....55
Figure 4.1	Nanoscale arbitrarily shaped inhomogeneities in a matrix material.....57
Figure 4.2	Surface coordinates (n, t) and Cartesian coordinates (x, y).....59
Figure 4.3	A nanoscale elliptical hole in a finite plate.....63
Figure 4.4	Comparison of analytical and finite element hoop stress solutions (dash lines for analytical solution of infinite plate and solid lines for finite plate with $2R/l=0.05$ and $2R/h=0.05$).....64

Figure 4.5	Variation of nondimensional hoop stress at $\theta = 0$ of a finite plate with R	65
Figure 4.6	Variation of nondimensional hoop stress at hole surface with θ	66
Figure 4.7	Variation of nondimensional hoop stress at $\theta = 0$ with $2R/l$ ($2R/h=0.1$; $R=5\text{nm}$ for $K^S > 0$ and $R=30\text{nm}$ for $K^S < 0$).....	66
Figure 4.8	Variation of nondimensional tangential stress of an elliptical hole with R and θ ($a/b=1.5$).....	67
Figure 4.9	Variation of nondimensional hoop stress at $\theta = 0$ with $2a/l$ ($2b/h=0.1$; $R=5\text{nm}$ for $K^S > 0$ and $R=30\text{nm}$ for $K^S < 0$).....	68
Figure 4.10	A nanoscale circular hole in a semi-infinite plate.....	69
Figure 4.11	Variation of nondimensional hoop stress at $\theta = \pm \pi/2$ with hole radius for two different D/R values ($D/R=2$ and 1.1).....	70
Figure 4.12	Variation of nondimensional hoop stress on hole surface with angle θ ($D/R=2$ and 1.1).....	71
Figure 4.13	Variation of nondimensional hoop stress with D/R ($R=5\text{nm}$ for $K^S > 0$ and $R=22\text{nm}$ for $K^S < 0$).....	72
Figure 4.14	Two circular inhomogeneities in a finite plate.....	73
Figure 4.15	Variation of nondimensional interfacial hoop stress with radius and angle ($D/R=2$; Solid lines for matrix and dash lines for inhomogeneity).....	74
Figure 4.16	Variation of nondimensional interfacial hoop stress with radius and angle ($D/R=1.1$; Solid lines for matrix and dash lines for inhomogeneity).....	75
Figure 4.17	Variation of nondimensional hoop stress with D/R ($R=5\text{nm}$ for $K^S > 0$ and $R=7\text{nm}$ for $K^S < 0$; Solid lines for $\theta = \pi$ and dash lines for $\theta = 0$)...76	
Figure 4.18	Variation of nondimensional hoop stress on hole surface at $\theta = 0$ with R ($2R/l=0.05$ and $2R/h=0.05$).....	77

Figure 4.19	Variation of nondimensional hoop stress along hole surface with θ ($2R/l=0.05$ and $2R/h=0.05$).....	77
Figure 4.20	Variation of nondimensional normal displacement with θ ($2R/l=0.05$ and $2R/h=0.05$; Solid lines for anisotropic case and dash lines for isotropic case).....	78

List of Symbols

a	Length of semi-major axis of ellipse
b	Length of semi-minor axis of ellipse
d	Loading ratio
E	Young's modulus
K^S	Surface elastic modulus defined as $2\mu^S + \lambda^S - \tau^0$
R_0	Radius or Curvature Radius
R	Radius or Average of lengths of semi-major and semi-minor axes of ellipse
$S_{\alpha\beta\gamma\delta}$	Surface elastic constant tensor
u_i	Displacement component in the i -direction
U^B	Bulk elastic strain energy
U^S	Surface elastic strain energy
W	Potential energy of external loads
γ	Surface free energy
$\tau_{\alpha\beta}^0$	Surface stress tensor under unstrained condition
τ^0	Residual surface stress under unstrained condition
σ_{ij}	Stress component
λ, μ	Lamé constants
λ^S, μ^S	Surface Lamé constants
λ_M, μ_M	Lamé constants of matrix
λ_1, μ_1	Lamé constants of inhomogeneity
ν	Poisson's ratio
ν_M	Poisson's ratio of matrix
ν_1	Poisson's ratio of inhomogeneity
Π	Total potential energy

Acknowledgements

I wish to express my greatest appreciation and gratitude to my advisor, Professor Nimal Rajapakse, for suggesting the topic of this thesis, and for his patient guidance and continuous support which enabled me to continue this work and complete the thesis. I also gratefully acknowledge the support from Professor Nimal Rajapakse's research grant from the Natural Sciences and Engineering Research Council of Canada.

I would also like to express my sincere thanks to the members of my thesis committee, Professor Mohamed Gadala and Professor Mu Chiao, for their kind help and for spending their time reading my thesis and make valuable comments.

I also want to thank my parents, my sisters and my friends for their constant support, encouragement and help.

Chapter 1

INTRODUCTION

1.1 Nanotechnology

In 1959, Nobel Laureate physicist Richard Feynman gave a now famous lecture, “There is plenty of room at the bottom” [1]. He stimulated his audience with the possibility that in future one could manipulate and control at the atomic level and create new materials, structures and devices. Nanotechnology is concerned with the development of such nanomaterials, nanostructures and nanodevices. Feynman’s lecture laid the foundation stone to conceptualize and develop the research base for nanotechnology. As science and technology advance, there has been a great demand for new materials with better properties for applications in various advanced technology developments. As a result of several decades of research and development, nanoscale materials and structures can now be fabricated and instruments such as scanning tunneling microscopes and atomic force microscopes have been invented for nanostructure measurement, characterization and manipulation. In 1999, another Nobel Laureate chemist Richard Smalley presented his views on nanotechnology: “We are about to be able to build things that work on the smallest possible length scales, atom by atom with the ultimate level of finesse. These little nanothings, and the technology that assembles and manipulates them – nanotechnology – will revolutionize our industries, and our lives [2]”. Nanoscience and nanotechnology are now attracting considerable interest and investment in order to develop revolutionary new applications in a wide range of disciplines.

So what are exactly ‘nano’, nanoscale materials and structures, etc? ‘Nano’ means a billionth, and a nanometer (nm) is 10^{-9} m which is roughly four times the diameter of an individual atom. Ten nanometers is about 1,000 times smaller than the diameter of a human hair [3]. Nanostructured or nanoscale materials mean materials that have at least one of the overall dimensions in the nanometer range (about 1 nm to 100 nm), such as

nanoparticles, nanowires and nanofilms. They are intermediate in size between atomic/molecular and microscopic structures. By assembling these nanoscale materials and structures, it is possible to manufacture nanocomposites, nanodevices and nanosystems with desired properties and functions.

What are the potential advantages of nanoscale materials and structures? How can nanoscience and nanotechnology affect our lives? Nanomaterials and nanodevices are based on fundamentally new molecular organization and they exhibit novel physical, chemical, and biological properties and phenomena. The assembly of the nanometer-scale components into large structures can produce nanocomposites, nanodevices and nanosystems with unique properties and functions. As shown in Fig. 1.1, the impact of nanoscience and nanotechnology is pervasive [3,4]. In information technology, nanoscale materials and structures have already found their way into information processing devices: faster sensors for signal acquisition and smaller size devices for denser information storage, etc. For medicine and patient care applications, it may be possible to produce new nanoparticle-based systems for drug delivery and nanosensors for early detection of diseases. In aeronautics and space exploration, potential applications include nanoinstrumentation for microspacecrafts and thermal barriers and wear-resistant nanostructured coatings. For environment and energy, nanotechnology can be used to develop semiconductor nanoparticles for efficient solar cells, reactive metal fine powders for groundwater decontamination, and nanoscale catalysis for increasing the efficiency of chemical reactions and combustion. In materials and manufacturing applications, nanostructured ceramics can be both harder and less brittle than currently available ceramics and nanoscale reinforcements in polymer composites can have greatly improved mechanical properties. Lighter, stronger and programmable materials, wear-resistant tires, tougher coatings, flame-retardant plastics, self-repairing materials and biologically inspired materials can be imagined. It is quite apparent that nanoscale materials and structures can provide mankind with significant benefits covering a wide range of applications.

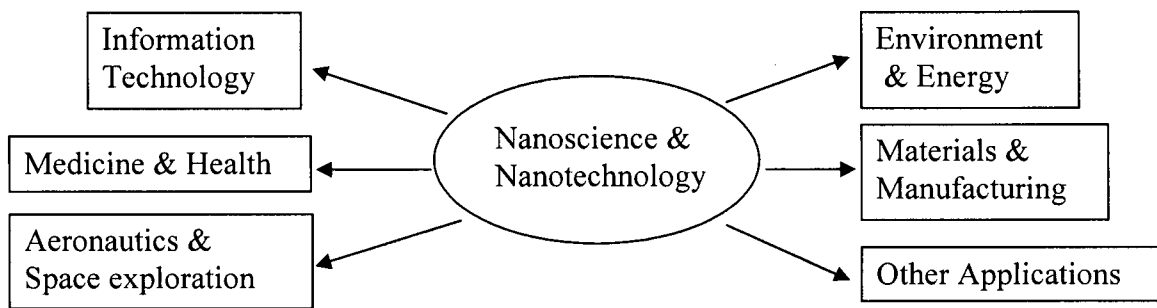


Fig. 1.1 Potential benefits of nanoscience & nanotechnology.

1.2 Nanoscale Mechanics

Before larger scale industrial application of nanoscale materials and nanostructures, it is necessary to have a comprehensive fundamental understanding of all aspects of their behaviour so that functionally and economically better designs can be achieved. Nanoscale mechanics, which deals with the study of mechanical properties and mechanical response of nanoscale materials and structures, is an important part of nanoscience and nanotechnology. Many applications of nanoscale materials and structures require knowledge of their deformation and stress field, strength, and fracture. For example, a carbon nanotube used as tip of a scanning probe microscope can be resistant to damage due to its flexibility [5]; Nanocomposites are expected to have higher stiffness and strength than classical composites due to nanoscale effects such as surface energy [3]. There are challenging issues in inelastic deformation and fracture of materials in the development of nanodevices, biopolymers, and hybrid bio-abio systems [6].

Different from continuum mechanics, which deals with bulk materials (usually applicable at length scales greater than 20 microns) and molecular dynamics which deal with behaviour at the molecular levels, nanoscale mechanics is concerned with objects with such characteristic lengths that neither the atomistic nor continuum models are applicable. In fact, nanoscale mechanics is now progressing in the direction of extending the concepts and methods of traditional continuum mechanics and bridging those with the effects at the molecular levels [7]. Such approaches are now known as multi-scale

modeling and involve consideration and combining of effects that occur at different length scales.

As concepts in continuum mechanics are well known in the mechanics community, it is useful to summarize the key features of the molecular dynamics/atomistic models. Different from the continuum mechanics in which the material is considered as a continuum, the atomistic models deal with the motion of atoms and simulate the behaviour of a nanoscale object by a cluster of atoms. The motion of atoms is governed by Newton's second law in which the atomic forces are derived from the interatomic potentials. The key issue is to determine the effective interatomic potentials efficiently and accurately. Molecular dynamic (MD) models are currently limited in applications due to heavy computing requirements.

An interesting class of problems in nanoscale mechanics deals with nanoscale inhomogeneities in materials. In practical terms, these include defects and reinforcements. Nanoparticles, nanowires, nanotubes, etc used in nanocomposites or quantum dots and wires used in semiconductor applications are good examples of nanoscale inhomogeneities [8]. It is well known that elastic field of quantum dots in a semiconductor device or nanoscale inhomogeneities in a composite can significantly influence the properties of a device or composite. Natural biological materials (e.g., nacre, bone), which are nanocomposites of soft proteins and brittle minerals, are very hard and tough, and by studying their behaviour at nanoscale it would be possible to develop bio-inspired materials in the laboratory [9]

As in the case of classical inhomogeneity problems, the mechanical field and effective material properties need to be determined for nanoscale inhomogeneity problems. The classical concepts of continuum mechanics need to be modified to account for effects that exist at the nanoscale. A significant such effect is the surface effect. For nanoscale problems, the ratio of surface to volume is high, and the effect of surface energy cannot be neglected. Several questions arise here. How can the surface energy

effects be included in the modeling of the inhomogeneity problems? How can atomistic structure and properties be included in such models? Is the behaviour of a nanoscale inhomogeneity vastly different from a macroscale inhomogeneity? These are a few questions that motivated the present study and to conduct research to examine the mechanical field of nanoscale inhomogeneities.

1.3 Review of Surface Elasticity Model

The surface/interface effects can be easily seen at the atomic scale, and this has been clearly pointed out and explained by Streitz et al. [10] and Dingreville et al. [11]. Due to different local environment, atoms at or near a free surface or interface have different equilibrium positions than do atoms in the bulk of a material. As a result, the energy of these atoms is, in general, different from that of the atoms in the bulk. The excess energy associated with the surface/interface atoms is called surface/interfacial free energy. The properties of a material, which are sensitive to the atomic positions or energies, are affected by the surface/interfacial free energy associated with these atoms at or near the surface/interface. For a material in which the number of atoms near the surface/interface is small compared to the total number of atoms, the surface/interface effects are insignificant and often can be neglected. For nanoscale structures, however, the surface/interface effects can be important due to the high ratio of surface/interface area to volume.

Nanoscale materials may exhibit novel phenomena such as higher elastic modulus and mechanical strength compared to the conventional materials due to the surface/interface energy effects. The ratio of surface free energy γ (J/m^2) and Young's modulus E (J/m^3), γ/E , is dimensional (m) and points to some other inherent parameter of a material [12]. This intrinsic length scale is usually small, in the nanometer range or even smaller. When a material or a constituent of a composite has one characteristic length comparable to the intrinsic scale, the surface free energy can play an important role on the properties of the material, and thus the properties become size-dependent. Many experiments have reported such size-dependent behavior. For example, atomic

force microscopy is used to determine the Young's modulus, strength and toughness of nanorods and nanotubes [13] and elastic modulus of nanowires [14]. Unlike bulk material elements, the measured effective elastic properties are highly dependent on the size of the nanostructure. Similar behavior is observed for nanocomposites. Singh et al. [15] investigated the toughness of nanoparticle-reinforced composites with varied particle sizes. More recently, Cadek et al. [16] measured the tensile modulus of nanotube-reinforced polymer composites. The above experimental studies reported that the mechanical properties depend on the size of the reinforcements and the surface area per unit volume.

To explain the size-dependent behavior at the nanoscale, several researchers have performed atomistic computer simulations. Sun and Zhang used a semi-continuum model [17] and Liang et al. used the embedded-atom-method inter-atomic potentials [18] to study elastic constants of plate-like nanomaterials and nanowires respectively, and reported the size-dependency of the elastic constants. Ji and Gao [9] explained the high toughness and strength of biological nano-composites through the virtual internal bond model and demonstrated the important role of embedded nanoscale minerals in such materials. Many simulation methods such as ab initio molecular dynamics, Monte Carlo simulations, classical empirical inter-atomic potentials have been developed to compute the properties of nanoscale materials and structures. These computer simulation methods, though very powerful, are often too complex and can model materials only in small scale as they need substantial computing power and are therefore not attractive in engineering applications.

Extension of continuum concepts to nanoscale is considered an attractive option by engineers because of the complexities associated with the molecular dynamics/atomistic models and the associated high computing cost. The surface (or interface)/inter-phase energy based concepts have been introduced to extend the classical continuum theories. It is assumed that the two homogeneous phases are separated by a layer which is defined as an inter-phase or a dividing surface/interface. In the concept of

inter-phase, a system is considered to be made of three phases—the two bulk phases and an inter-phase. The inter-phase has a finite volume and the boundaries of the inter-phase are usually chosen to be at locations at which the properties of atoms are no longer varying significantly with position [11]. It is pointed out that, in the analytical or numerical analysis of boundary-value problems of composites, it is convenient to replace the inter-phase model by a proper surface/interface model [19]. In the concept of a surface/interface model, the two bulk phases are considered to be separated by a single dividing surface, and the surface is assumed to be a mathematical layer of zero-thickness. A surface stress tensor exists on the surface layer owing to the surface/interfacial free energy. The displacement and/or stress discontinuities are assumed at the interface. In the case of nanoscale materials and structures, the surface/interface stress model has become an attractive option because the surface/interface contribution to the property of the material can be accounted and the surface/interface stress can properly represent the effect of the surface/interfacial energy.

Gibbs [20] first introduced the concepts of surface/interface energy and surface stress. In the Gibbs's formalism of thermodynamics [20], a quantity, γ , called surface free energy, is defined to represent the reversible work per unit area due to creating a new surface. Gibbs [20] also pointed out that in the case of solids, there is a different type of quantity, called the surface stress that is associated with the reversible work per unit area needed to elastically stretch a pre-existing surface. From the thermodynamics of solid surfaces, the relationship between the surface stress and the surface free energy has been derived as [21,22]

$$\sigma_{\alpha\beta} = \gamma\delta_{\alpha\beta} + \partial\gamma/\partial\varepsilon_{\alpha\beta}, \quad (1.1)$$

where $\sigma_{\alpha\beta}$ and $\varepsilon_{\alpha\beta}$ denote the surface stress and strain, respectively, and δ_{ij} is the Kronecker delta. It should be noted that the surface stress tensor is a 2D quantity in the tangent plane of the surface and the strain normal to the surface is excluded in Eq. (1.1). Thus, the Greek indices take the value of 1 or 2. In the right-hand side of Eq. (1.1), the first term has no explicit variation of the strain, but the second term indicates a variation

of the surface free energy with respect to surface strain. Nix and Gao [23] presented an atomistic interpretation of the interface stress and showed that Eq. (1.1) is an expression in the Eulerian frame of reference and the first term does not appear in the embedded Lagrangian coordinates.

Eq. (1.1) can be rewritten by introducing a set of surface elastic constants. Miller and Shenoy [24] and Shenoy [25] suggested a linear constitutive equation of the following form:

$$\sigma_{\alpha\beta} = \tau_{\alpha\beta}^0 + S_{\alpha\beta\gamma\delta} \varepsilon_{\gamma\delta}, \quad (1.2)$$

where $\tau_{\alpha\beta}^0$ is the surface stress when the bulk is unstrained, and $S_{\alpha\beta\gamma\delta}$ is the fourth order surface elastic constant tensor. In general, there are at most six independent elastic constants for a crystal surface. The number of independent elastic constants can be reduced when a surface possesses geometric symmetry [25]. For an isotropic surface, Gurtin and Murdoch [26] and Gurtin et al. [27] proposed the following generic and simple expression for surface stress-strain relation.

$$\sigma_{\alpha\beta} = \tau^0 \delta_{\alpha\beta} + (\lambda^S + \tau^0) \varepsilon_{\gamma\gamma} \delta_{\alpha\beta} + 2(\mu^S - \tau^0) \varepsilon_{\alpha\beta}, \quad (1.3)$$

where λ^S and μ^S are the surface Lamé constants and τ^0 is the residual surface stress under unstrained conditions.

The surface elastic constants are quite different from the bulk elastic constants and have to be known before applying the surface stress model. With the assumption of isotropy, Gurtin and Murdoch [28] computed some sample values of the surface moduli. By using molecular dynamics, Dingreville et al. [11] presented the calculation of the surface elastic constants with surface energy. A systematic study of the surface elastic constants has been performed by Shenoy [25] and their values can be calculated from atomistic simulations. It is found that the surface elastic constants tensor $S_{\alpha\beta\gamma\delta}$ need not be positive definite. Therefore, the quadratic form $S_{\alpha\beta\gamma\delta} \varepsilon_{\alpha\beta} \varepsilon_{\gamma\delta}$ may be negative, but it does not violate the basic thermodynamic postulates. Shenoy [25] pointed out that a

surface region with a special atomic structure cannot exist without the bulk and the total energy (bulk + surface) still satisfies the positive definite condition. At present, the determination of surface elastic constants by experiments seems to be a challenging task and requires further efforts to address some fundamental challenges [25].

In general, the surface/interface properties are anisotropic and depend on the crystallographic direction of the surface/interface, and thus surfaces/interfaces in solids usually have anisotropic stresses [25,27,29]. However, as pointed out by Weissmüller and Cahn [29], “obtaining empirical database to determine fully the interface stress would be an enormous undertaking out of proportion to its usefulness”. Moreover, one can assume that the interface has isotropic stress and it is still meaningful to use suitable averages of the interface stress [29,30]. Therefore, the isotropic assumption of surface/interface stress is considered acceptable in the study of surface/interface effects and to illustrate the key features of physical behaviour [31-33].

It is noted that the surface/interface stress model is only an idealization of a complex problem. In fact, the surface/interface region contains several layers of atoms which have different properties from that of atoms in the bulk. Therefore, the surface/interface stress model is valid if and only if the bulk material is much larger than the size of several layers of atoms [11]. If the bulk material contains only a small number of atoms which is comparable to that of the atoms at or near the surface/interface, the validity of macroscopic thermodynamic quantities such as surface free energy is questionable and the applicability of surface/interface stress model can be challenged [11].

The presence of surface/interface stresses results in a jump of traction from one bulk phase to the other and results in a non-classical stress boundary condition. This boundary condition and the surface stress-strain relations together with the equilibrium equations of bulk body form a coupled system of field equations. The displacement at the interface is assumed to be continuous or discontinuous in the literature. For the first kind

of deformation, the two homogeneous bulk phases are perfectly bonded, but for the second kind, slip or imperfect bonding exists at the interface.

1.4 Review of Classical and Modern Inhomogeneity Problems

Elastic materials containing single or multiple holes, inhomogeneities and eigenstrain regions are commonly known as inhomogeneity problems in mechanics literature. Such problems have a wide range of practical applications including the determination of effective properties of composites, mechanical fields due to phase transformations in materials, stress concentration factors, etc. Inhomogeneity problems have been studied extensively in micromechanics for several decades since the celebrated work of Eshelby [34-36]. The books by Mura [37], Nemat-Nasser and Hori [38], and Marko and Preziosi [39] have provided compressive reviews of the micromechanics of heterogeneous materials. The above references deal exclusively with the classical inhomogeneity problems based on continuum mechanics.

Nowadays, an inhomogeneity can be fabricated with dimensions of the order of 1-100nm by taking advantage of nanotechnology. Research on modern inhomogeneity problems is emerging and experimental, theoretical and computational tools are used to examine this class of problems. An interesting research topic in nanomechanics is the study of elastic field of nanoscale inhomogeneities in an elastic matrix. Due to high surface/interface to volume ratio of nanoscale inhomogeneities, it is necessary to incorporate the surface/interface effects which are neglected in the classical solution. The surface stress model has been employed to study modern inhomogeneity problems. Yang [40] obtained closed-form solutions of the effective shear moduli and bulk modulus of composite with dilute nanocavities when considering only constant surface stress (or surface free energy), and found that the solutions are a function of the surface free energy, size of the nanocavity and the surface stress effect only influences the elastic field around the hole surface. By considering the surface stress without a residual stress, Duan et al. [33] examined the effective bulk and shear moduli of a solid containing nano-inhomogeneities and showed that the effective properties depend on the surface elastic

constants. Sharma et al. [31] presented a closed-form expression of the size-dependent elastic state of a spherical nano-inhomogeneity under far-field triaxial loading and a dilatational eigenstrain by applying the Gurtin-Murdoch model with both residual surface stress and strain-dependent surface stress. Sharma and Ganti [32] studied Eshelby's tensor of a nano-inhomogeneity undergoing a dilatational eigenstrain and pointed out that only inhomogeneities with a constant curvature admit a uniform elastic state. Duan et al. [41] extended the Eshelby formalism for a nanoscale spherical inhomogeneity subjected to an arbitrary uniform eigenstrain (not dilatational) by considering the surface/interface effects and demonstrated that the Eshelby and stress concentration tensors are, in general, not uniform inside the inhomogeneity but are position-dependent and size-dependent. While the present thesis was in the final completion, Gao et al. [42] reported the extension of the classical finite element method (FEM) by introducing surface elements to take into account the surface effect and then applied the method to investigate the interaction between two nanovoids and effective moduli of nanoporous materials. It is noted that all the above studies assumed that both bulk and surfaces/interfaces are elastically isotropic.

1.5 Scope of the Current Work

Based on the above introduction and literature survey, it is found that nanoscale materials and structures have attracted significant interest due to their potential use in the development of materials with novel and improved properties. Inhomogeneity problems at the nanoscale have become an important research topic with significant impact on advanced materials development based on nanotechnology. Recent research has incorporated the surface/interface effects by applying the surface/interface stress model to study the mechanical properties and behavior of an inhomogeneity-matrix system. However, studies on practically useful inhomogeneity shapes (elliptic and spheroidal inhomogeneities), multiple inhomogeneities, non-symmetric loading, etc have not yet appeared in the literature. Therefore, this thesis tries to fill a part of this gap by focusing on the study of two-dimensional inhomogeneity problems at the nanoscale. The main objective of the thesis is to provide a comprehensive theoretical analysis of a two-

dimensional elastic matrix containing a dilute distribution of nanoscale circular/elliptical inhomogeneities under arbitrary loading and investigate the elastic field of the inhomogeneity and matrix. A finite element scheme is also presented to analyze finite plate with an inhomogeneity and more complex geometries such as two interacting inhomogeneities problems.

Chapter 2 presents the details of the derivation of an analytical solution for elastic field of a nanoscale circular inhomogeneity embedded in an infinite isotropic elastic matrix. Perfect bonding is assumed at the inhomogeneity-matrix interface. The Gurtin-Murdoch surface stress model is applied to take into account the surface stress effects. Muskhelishvili's complex potential approach is extended for the first time to solve this class of problems with a non-classical boundary condition. The closed-form solution derived in this thesis corresponds to a far-field uniform biaxial traction and a uniform eigenstrain in the inhomogeneity. Selected numerical results are presented for the elastic field around a circular hole and the inhomogeneity-matrix interface. Chapter 3 considers an inhomogeneity having the shape of an ellipse. Similar to the case of circular inhomogeneity, displacement continuity at the interface is assumed and the Gurtin-Murdoch model is used. By using the conformal mapping and the complex variable technique of Muskhelishvili, infinite series expressions of analytic potential functions are obtained approximately. Selected numerical results are then presented for the elastic field around an elliptical hole and an inhomogeneity-matrix interface.

In Chapter 4, a finite element scheme is developed to study more complex inhomogeneity problems. The present approach, although developed independently of Gao. et al. [42], is conceptually identical. However, this thesis presents a more careful validation of the FEM scheme by using the analytical solution for elliptical inhomogeneity and examining other special features such as the instability of elastic field for negative value of surface elastic constants. So in Chapter 4, the finite element formulation is first presented to incorporate the surface/interface stress effect. The finite element solution is then verified by considering the stress field around a circular hole in a

large plate under tension and comparing the results with the theoretical solution derived in Chapter 2. The elastic field around a circular/elliptical hole in a finite plate is studied by using the finite element scheme by taking into account the surface stress effects. To study the interaction between inhomogeneities, the elastic field of a finite plate with two nanoscale circular inhomogeneities is also investigated. Finally, an example of anisotropic case is presented. Chapter 5 presents a summary of the thesis, major findings of the current study and suggestions for future work.

Chapter 2

ELASTIC FIELD OF AN INFINITE MATRIX WITH A NANOSCALE CIRCULAR INHOMOGENEITY

2.1 Problem Description and Basic Equations

In this chapter, a two-dimensional problem of the elastic field solution for an infinite matrix containing nanoscale circular inhomogeneities at dilute distribution is considered. The surface effects need to be incorporated due to the nanoscale dimensions of the inhomogeneities. The inhomogeneities are assumed to be so far apart that their interaction can be neglected. Thus the problem is simplified to an infinite matrix containing a single nanoscale circular inhomogeneity. In the current study, the matrix is subjected to uniform far-field tractions σ_{11}^{∞} , σ_{22}^{∞} and σ_{12}^{∞} and a uniform eigenstrain ε^* is prescribed in the inhomogeneity (Fig. 2.1). The matrix and inhomogeneity materials are assumed to be linearly elastic, homogeneous and isotropic with Lamé constants λ_M , μ_M and λ_I , μ_I , respectively. Note that the subscripts M and I are used to identify quantities associated with the matrix and inhomogeneity respectively. The inhomogeneity, with its center at the origin of the coordinate system, has radius R_0 as shown in Fig. 2.1.

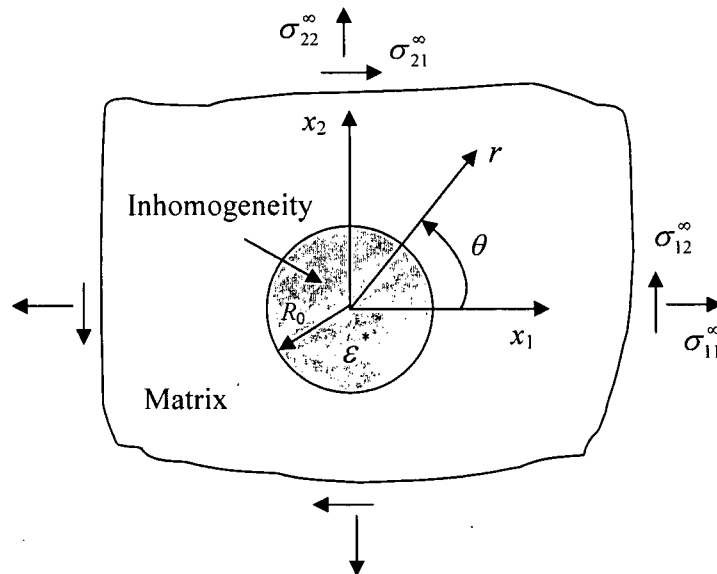


Fig. 2.1 A nanoscale circular inhomogeneity in an infinite matrix.

For plane problems of classical elasticity, Muskhelishvili [43] provided an analytical solution by using the complex potential functions method. Muskhelishvili's approach is used to study the current problem. The displacement and stress components in Cartesian and polar coordinates, (x_1, x_2, x_3) and (r, θ, x_3) respectively, can be expressed in terms of two analytic functions $\phi(z)$ and $\psi(z)$ as [43]:

$$2\mu(u_r + iu_\theta) = e^{-i\theta} [\kappa\phi(z) - z\overline{\phi'(z)} - \overline{\psi(z)}], \quad (2.1)$$

$$\sigma_{rr} + \sigma_{\theta\theta} = 2[\phi'(z) + \overline{\phi'(z)}], \quad (2.2)$$

$$\sigma_{rr} - i\sigma_{r\theta} = \phi'(z) + \overline{\phi'(z)} - e^{i2\theta} [\bar{z}\phi''(z) + \psi'(z)], \quad (2.3)$$

$$2\mu(u_1 + iu_2) = \kappa\phi(z) - z\overline{\phi'(z)} - \overline{\psi(z)}, \quad (2.4)$$

$$\sigma_{11} + \sigma_{22} = 2[\phi'(z) + \overline{\phi'(z)}], \quad (2.5)$$

$$\sigma_{22} - \sigma_{11} + 2i\sigma_{12} = 2[\bar{z}\phi''(z) + \psi'(z)], \quad (2.6)$$

where u_i and σ_{ij} are displacement and stress components respectively, $z = x_1 + ix_2 = re^{i\theta}$, $\kappa = 3 - 4\nu$ for plane strain and $(3 - \nu)/(1 + \nu)$ for plane stress, and μ and ν are the shear modulus and Poisson's ratio, respectively. The overbar in Eqs. (2.1)-(2.6) represents the complex conjugate, and the prime denotes differentiation with respect to the variable z .

2.2 Formulation of Inhomogeneity Problem

Assume that there is perfect bonding at the inhomogeneity-matrix interface, then the displacements are continuous at the interface:

$$(u_r + iu_\theta)_M = (u_r + iu_\theta)_I + (u_r + iu_\theta)_I^*, \quad \text{at } r = R_0, \quad (2.7)$$

where the last term is the displacement induced by the prescribed uniform dilatational eigenstrain ε^* , i.e., $\varepsilon_{11}^* = \varepsilon_{22}^* = \varepsilon^*$, and $(u_r + iu_\theta)_I|_{r=R_0} = R_0\varepsilon^*$.

The surface traction on the inhomogeneity-matrix interface is discontinuous due to the surface stress effect. The inhomogeneity and matrix phases are assumed to be separated by a single dividing interface layer with zero thickness and surface stress exists

on this layer owing to the surface/interfacial free energy. This interface layer has different elastic properties from that of the bulk. For isotropic bulk and interface, the following field equations and constitutive relations can be established based on the theory proposed by Gurtin and Murdoch [26] and Gurtin et al. [27]:

In the bulk (matrix and inhomogeneity):

$$\sigma_{ij,j}^B = 0, \quad \sigma_{ij}^B = \lambda \delta_{ij} \varepsilon_{kk} + 2\mu \varepsilon_{ij}, \quad (2.8)$$

On the surface/interface:

$$\llbracket \sigma_{\beta\alpha}^B n_\beta \rrbracket + \sigma_{\beta\alpha,\beta}^S = 0, \quad (2.9)$$

$$\llbracket \sigma_{ji}^B n_i n_j \rrbracket = \sigma_{\alpha\beta}^S k_{\alpha\beta}, \quad (2.10)$$

$$\sigma_{\beta\alpha}^S = \tau^0 \delta_{\beta\alpha} + 2(\mu^S - \tau^0) \varepsilon_{\beta\alpha} + (\lambda^S + \tau^0) \varepsilon_{\gamma\gamma} \delta_{\beta\alpha}, \quad (2.11)$$

where superscripts B and S are used to denote the quantities corresponding to bulk (matrix and inhomogeneity) and surface/interface; σ_{ij} and ε_{ij} denote stress and strain, respectively; λ and μ are the bulk Lamé constants; δ_{ij} is the Kronecker delta; n_i is the normal vector on the surface; λ^S and μ^S are the surface Lamé constants; τ^0 is the residual surface stress under unstrained conditions; $k_{\alpha\beta}$ is the curvature tensor of the surface/interface and $\llbracket * \rrbracket = (*)_M - (*)_I$ denotes the jump across the matrix-inhomogeneity interface. It should be noted that the surface stress tensor is a 2D quantity and the strain normal to the surface is excluded in Eq. (2.11). Thus, the Greek indices take the value of 1 or 2, while Latin subscripts adopt values from 1 to 3.

In the bulk, the equilibrium equations and constitutive relation are the same as those in the classical elasticity. On the surface, the surface stress [Eq. (2.11)] is a sum of a residual stress and a linear function of surface strain, and the surface Lamé constants are different from that of the bulk. Eq. (2.9) and (2.10) are the equilibrium equations in the tangential plane and normal direction of the interface respectively. The presence of surface stress results in a non-classical stress boundary condition. When no surface stress is considered, these equations reduce to the classical traction continuity equations. In the (r, θ, x_3) coordinate [x_3 is the direction perpendicular to the (r, θ) -plane], Eqs. (2.9) and (2.10) can be written as:

On the surface/interface:

$$\text{In } \theta\text{-direction: } \quad \left[\left[\sigma_{r\theta}^B \right] \right] + \frac{\partial \sigma_{\theta\theta}^S}{R_0 \partial \theta} + \frac{\partial \sigma_{3\theta}^S}{\partial x_3} = 0, \quad (2.12)$$

$$\text{In } x_3\text{-direction: } \quad \left[\left[\sigma_{r3}^B \right] \right] + \frac{\partial \sigma_{33}^S}{\partial x_3} + \frac{\partial \sigma_{\theta 3}^S}{R_0 \partial \theta} = 0, \quad (2.13)$$

$$\text{In } r\text{-direction: } \quad \left[\left[\sigma_{rr}^B \right] \right] = \frac{\sigma_{\theta\theta}^S}{R_0}. \quad (2.14)$$

For plane problems, $\sigma_{r3}^B = \sigma_{3\theta}^S = \sigma_{\theta 3}^S = 0$ and the derivatives with respect to x_3 are zero. Thus, Eq. (2.13) is automatically satisfied. Eqs. (2.12) and (2.14) can be expressed in the following complex variable form:

$$\left[\left[\sigma_{rr}^B - i \sigma_{r\theta}^B \right] \right] = \frac{\sigma_{\theta\theta}^S}{R_0} + i \frac{\partial \sigma_{\theta\theta}^S}{R_0 \partial \theta}. \quad (2.15)$$

The left-hand side of Eq. (2.15) can be written in terms of potential functions by using Eq. (2.3). For the right-hand side, the surface stress is:

$$\sigma_{\theta\theta}^S = \tau^0 + 2(\mu^S - \tau^0)\varepsilon_{\theta\theta} + (\lambda^S + \tau^0)(\varepsilon_{33} + \varepsilon_{\theta\theta}). \quad (2.16)$$

The elastic strain $\varepsilon_{\theta\theta}$ at the surface can be obtained from the following equations:

$$\varepsilon_{\theta\theta} + \varepsilon_{rr} = \frac{1}{Q} \left(\phi'(z) + \overline{\phi'(z)} \right) \Big|_{r=R_0}, \quad (2.17)$$

$$\varepsilon_{\theta\theta} - \varepsilon_{rr} + i\varepsilon_{r\theta} = \frac{1}{\mu} \left[\bar{z}\phi''(z) + \psi'(z) \right] e^{i2\theta} \Big|_{r=R_0}. \quad (2.18)$$

Here, $Q = \lambda + \mu$ for plane strain and $Q = \mu(3\lambda + 2\mu)/(\lambda + 2\mu)$ for plane stress. Therefore,

$$\varepsilon_{\theta\theta} = \frac{1}{2Q} \left[\phi'(z) + \overline{\phi'(z)} \right] + \frac{1}{4\mu} \left[\bar{z}\phi''(z) + \psi'(z) \right] e^{2i\theta} + \frac{1}{4\mu} \left[z\phi''(z) + \overline{\psi'(z)} \right] e^{-2i\theta} \Big|_{r=R_0}. \quad (2.19)$$

Note that the strain $\varepsilon_{\theta\theta}$ is continuous at the interface because of the continuous displacement at the interface. In the following derivation, the strain $\varepsilon_{\theta\theta}$ is calculated from the matrix. Note that $\varepsilon_{33} = 0$ for plane strain and $\varepsilon_{33} = \nu(\varepsilon_{rr} + \varepsilon_{\theta\theta})/(\nu - 1) \Big|_{r=R_0}$ for plane stress. Because of the discontinuity of the strain ε_{33} at the interface for plane stress, the mean strain is used, i.e.,

$$\varepsilon_{33} = \frac{1}{2} [(\varepsilon_{33})_M + (\varepsilon_{33})_I]_{r=R_0} \quad (2.20)$$

$(\varepsilon_{33})_M$ can be obtained by using Eq. (2.17). Due to the eigenstrain effect, $(\varepsilon_{33})_I$ is,

$$(\varepsilon_{33})_I = \frac{\nu_1}{\nu_1 - 1} [(\varepsilon_{rr} + \varepsilon_{\theta\theta})_I^e + 2\varepsilon^*], \quad (2.21)$$

where $(\varepsilon_{rr} + \varepsilon_{\theta\theta})_I^e$ is the elastic strain in the inhomogeneity, which can be obtained from Eq. (2.17).

From the above discussion, we have to obtain the complex potential functions which should satisfy the boundary conditions. To simplify the expression in the following derivation, introduce a non-dimensional complex variable ξ such that:

$$z = m(\xi) = R_0 \xi, \quad \xi = r_0 e^{i\theta}, \quad r_0 = r/R_0. \quad (2.22)$$

Note that at the interface $r_0 = 1$, and $\phi(\xi) = \phi(m(\xi))$ and $\psi(\xi) = \psi(m(\xi))$. The complex potentials $\phi_M(\xi)$, $\phi_I(\xi)$, $\psi_M(\xi)$ and $\psi_I(\xi)$ corresponding to the matrix and inhomogeneity are now expanded into the following Laurent series form:

$$\phi_M(\xi) = A\xi + \sum_{n=1}^{\infty} A_n \xi^{-n}, \quad \psi_M(\xi) = B\xi + \sum_{n=1}^{\infty} B_n \xi^{-n}, \quad (2.23)$$

$$\phi_I(\xi) = \sum_{n=1}^{\infty} F_n \xi^n, \quad \psi_I(\xi) = \sum_{n=1}^{\infty} G_n \xi^n. \quad (2.24)$$

Note that the constant terms have been omitted in Eqs. (2.23) and (2.24) since they represent the rigid body displacements and have no effect on the stress distribution. In Eq. (2.23), A and B are real and complex numbers respectively characterizing the remote stress field. In view of Eqs. (2.5) and (2.6),

$$\sigma_{11}^{\infty} + \sigma_{22}^{\infty} = \frac{4A}{R_0}, \quad \sigma_{22}^{\infty} - \sigma_{11}^{\infty} + 2i\sigma_{12}^{\infty} = \frac{2B}{R_0}, \quad (2.25)$$

where σ_{11}^{∞} , σ_{22}^{∞} and σ_{12}^{∞} are the far-field stresses which in the case of our study are assumed to be:

$$\sigma_{22}^{\infty} = \sigma_0, \quad \sigma_{11}^{\infty} = d\sigma_0, \quad \sigma_{12}^{\infty} = 0. \quad (2.26)$$

Here, d is a real number characterizing the loading ratio $\sigma_{11}^{\infty}/\sigma_{22}^{\infty}$. In the present case, both A and B are real numbers. Note that $d=1$ and $d=0$ refer to biaxial and uniaxial loadings, respectively, while $d=-1$ represents pure shear loading.

The following set of equations is obtained by substituting Eqs. (2.1), (2.23) and (2.24) into Eq. (2.7) and equating the coefficients of $e^{in\theta}$.

$$0 = -2\bar{F}_2, \quad \frac{\mu_1}{\mu_M}(\kappa_M A_1 - B) = -3\bar{F}_3 - \bar{G}_1,$$

$$\frac{\mu_1}{\mu_M} \kappa_M A_{n+1} = -(n+3)\bar{F}_{n+3} - \bar{G}_{n+1}, \quad (n=1, 2, 3\dots), \quad (2.27)$$

$$\frac{\mu_1}{\mu_M}(\kappa_M A - A - \bar{B}_1) = \kappa_1 F_1 - \bar{F}_1 + 2\mu_1 R_0 \varepsilon^*, \quad -\frac{\mu_1}{\mu_M} \bar{B}_2 = \kappa_1 F_2,$$

$$\frac{\mu_1}{\mu_M}(n\bar{A}_n - \bar{B}_{n+2}) = \kappa_1 F_{n+2}, \quad (n=1, 2, 3\dots). \quad (2.28)$$

Substitution of Eqs. (2.3), (2.16), (2.23) and (2.24) into Eq. (2.15) yields:

$$2A + B_1 - (F_1 + \bar{F}_1) = \tau^0 + 4\Lambda_5 \mu_1 R_0 \varepsilon^* - \Lambda_1 B_1 - \Lambda_1 \bar{B}_1 + 2(\Lambda_1 + \Lambda_3)\Lambda_2 A + \Lambda_4 \Lambda_5 (F_1 + \bar{F}_1),$$

$$2B_2 - 2\bar{F}_2 = \Lambda_1 B_2 + 4\Lambda_4 \Lambda_5 \bar{F}_2,$$

$$-\bar{A}_1 - B + 3F_3 + G_1 = -\Lambda_1 B - 2\Lambda_1 \bar{A}_1 + 3\Lambda_1 \bar{B}_3 + (\Lambda_1 + \Lambda_3)\Lambda_2 \bar{A}_1 - 3\Lambda_4 \Lambda_5 F_3,$$

$$-A_1 + B_3 - \bar{F}_3 = \Lambda_1 \bar{B} + 2\Lambda_1 A_1 - 3\Lambda_1 B_3 - (\Lambda_1 + \Lambda_3)\Lambda_2 A_1 + 3\Lambda_4 \Lambda_5 \bar{F}_3,$$

$$-\bar{A}_{n+1} + (n+3)F_{n+3} + G_{n+1} = -\Lambda_1(n+1)(n+2)\bar{A}_{n+1} + \Lambda_2(\Lambda_1 + \Lambda_3)(n+1)\bar{A}_{n+1}$$

$$\quad + \Lambda_1(n+3)\bar{B}_{n+3} - (n+3)\Lambda_4 \Lambda_5 F_{n+3}, \quad (n=1, 2, 3\dots),$$

$$-(n+1)A_{n+1} + B_{n+3} - \bar{F}_{n+3} = \Lambda_1(n+1)(n+2)A_{n+1} - \Lambda_2(\Lambda_1 + \Lambda_3)(n+1)A_{n+1}$$

$$\quad - \Lambda_1(n+3)B_{n+3} + (n+3)\Lambda_4 \Lambda_5 \bar{F}_{n+3}, \quad (n=1, 2, 3\dots), \quad (2.29)$$

where

$$\Lambda_1 = \frac{K^S}{4\mu_M R_0}, \quad \Lambda_2 = \frac{2\mu_M}{Q_M}, \quad K^S = 2\mu^S + \lambda^S - \tau^0, \quad \Lambda_4 = \frac{2\mu_1}{Q_1},$$

$$\Lambda_3 = 0 \text{ for plane strain and } \frac{\lambda^S + \tau^0}{4\mu_M R_0} \frac{\nu_M}{\nu_M - 1} \text{ for plane stress,}$$

$$\Lambda_5 = 0 \text{ for plane strain and } \frac{\lambda^S + \tau^0}{4\mu_1 R_0} \frac{\nu_1}{\nu_1 - 1} \text{ for plane stress.} \quad (2.30)$$

Note that all the parameters Λ_1 , Λ_3 and Λ_5 are defined as some quantity divided by the inhomogeneity radius R_0 . These quantities only depend on the material properties of the bulk and interface, and hence represent the intrinsic length scales.

The solution of Eqs. (2.27)-(2.29) yields,

$$A_1 = \frac{(-c_1 + c_2 - c_3 + 3\Lambda_4\Lambda_5c_6)B}{d_1 + \kappa_M c_2 + d_2 + 3\Lambda_4\Lambda_5d_3}, \quad A_{n+1} = 0, \quad (n=1, 2, 3\dots), \quad (2.31)$$

$$B_1 = \frac{\Lambda_7\tau^0 + 2(2\Lambda_5\Lambda_7 - c_7)\mu_1 R_0 \varepsilon^* + 2(\Lambda_7c_4 + \Lambda_6\Lambda_8c_7)A}{\Lambda_6c_7 + \Lambda_7c_1}, \quad B_2 = 0,$$

$$B_3 = \frac{(c_4 + c_5 - c_3 + 3\Lambda_4\Lambda_5c_6)B}{d_1 + \kappa_M c_2 + d_2 + 3\Lambda_4\Lambda_5d_3}, \quad B_{n+3} = 0, \quad (n=1, 2, 3\dots), \quad (2.32)$$

$$F_1 = \frac{-\Lambda_6\tau^0 + 2\Lambda_6(c_1\Lambda_8 - c_4)A - 2(2\Lambda_5\Lambda_6 + c_1)\mu_1 R_0 \varepsilon^*}{2(\Lambda_6c_7 + \Lambda_7c_1)}, \quad F_2 = 0,$$

$$F_3 = \frac{\Lambda_6}{\kappa_1} \frac{(-c_1 + c_2 - c_4 - c_5)B}{d_1 + \kappa_M c_2 + d_2 + 3\Lambda_4\Lambda_5d_3}, \quad F_{n+3} = 0, \quad (n=1, 2, 3\dots), \quad (2.33)$$

$$G_1 = -\Lambda_6 \left(\frac{\kappa_M(-c_1 + c_2 - c_3 + 3\Lambda_4\Lambda_5c_6)B}{d_1 + \kappa_M c_2 + d_2 + 3\Lambda_4\Lambda_5d_3} - B \right) - \frac{3\Lambda_6}{\kappa_1} \frac{(-c_1 + c_2 - c_4 - c_5)B}{d_1 + \kappa_M c_2 + d_2 + 3\Lambda_4\Lambda_5d_3},$$

$$G_{n+1} = 0, \quad (n=1, 2, 3\dots), \quad (2.34)$$

where

$$\begin{aligned} \Lambda_6 &= \mu_1/\mu_M, & \Lambda_7 &= (\kappa_1 - 1)/2, & \Lambda_8 &= (\kappa_M - 1)/2, \\ c_1 &= 1 + 2\Lambda_1, & c_2 &= \Lambda_6(1 + 3\Lambda_1), & c_3 &= \Lambda_6(1 - \Lambda_1 - \Lambda_6)/\kappa_1, & c_4 &= \Lambda_2(\Lambda_1 + \Lambda_3) - 1, \\ c_5 &= \Lambda_6[1 - \Lambda_2(\Lambda_1 + \Lambda_3) + 2\Lambda_1 + \kappa_M\Lambda_1], & c_6 &= \Lambda_6(\Lambda_6 - 1)/\kappa_1, & c_7 &= 1 + \Lambda_4\Lambda_5, \\ d_1 &= 1 + 4\Lambda_1 + \Lambda_2(\Lambda_1 + \Lambda_3), & d_2 &= \Lambda_6[1 + \Lambda_1 + \Lambda_2(\Lambda_1 + \Lambda_3) + \kappa_M\Lambda_6]/\kappa_1, \\ d_3 &= \Lambda_6(1 + \kappa_M\Lambda_6)/\kappa_1. \end{aligned} \quad (2.35)$$

The complete elastic field is explicitly given by Eqs. (2.1)-(2.6) together with Eqs. (2.23), (2.24) and (2.30)-(2.35). After some manipulation, the stresses along the interface are:

In the matrix:

$$\sigma_{\theta\theta} = \frac{2A - B_1}{R_0} + \frac{(B - 3B_3) \cos 2\theta}{R_0},$$

$$\begin{aligned}\sigma_{rr} &= \frac{2A + B_1}{R_0} + \frac{(-4A_1 - B + 3B_3) \cos 2\theta}{R_0}, \\ \sigma_{r\theta} &= \frac{(-2A_1 + B + 3B_3) \sin 2\theta}{R_0},\end{aligned}\quad (2.36)$$

In the inhomogeneity:

$$\begin{aligned}\sigma_{\theta\theta} &= \frac{2F_1}{R_0} + \frac{(12F_3 + G_1) \cos 2\theta}{R_0}, \quad \sigma_{rr} = \frac{2F_1}{R_0} - \frac{G_1 \cos 2\theta}{R_0}, \\ \sigma_{r\theta} &= \frac{(6F_3 + G_1) \sin 2\theta}{R_0}.\end{aligned}\quad (2.37)$$

Note that due to the surface/interface stress effects, $\Lambda_1(\Lambda_3, \Lambda_5) \neq 0$ and $\tau^0 \neq 0$, and the stress state depends on the size of the inhomogeneity R_0 as the coefficients A_1, B_1, B_3, F_1, F_3 , and G_1 in Eqs. (2.31)-(2.34) are nonlinear functions of R_0 . When R_0 is quite larger than the intrinsic scales, these parameters Λ_1, Λ_3 and Λ_5 are very closed to zero, and the surface effects will only depend on constant surface stress τ^0 . When R_0 is comparable to the intrinsic length, Λ_1, Λ_3 and Λ_5 are large and the surface effects would be important. When no surface/interface stresses exist, i.e., $\Lambda_1 = \Lambda_3 = \Lambda_5 = 0$ and $\tau^0 = 0$, the above results reduce to the classical solution in which the elastic state is size-independent. The shear and radial stresses are equal on either side of the interface in the classical case and,

$$\begin{aligned}\sigma_{r\theta} &= \frac{\Lambda_6(1 + \kappa_M)(1 - d)\sigma_0 \sin 2\theta}{2(1 + \kappa_M\Lambda_6)}, \\ \sigma_{rr} &= \frac{\Lambda_6(1 + \Lambda_8)(1 + d)\sigma_0 - 4\mu_1\varepsilon^*}{2(\Lambda_6 + \Lambda_7)} - \frac{\Lambda_6(1 + \kappa_M)(1 - d)\sigma_0 \cos 2\theta}{2(1 + \kappa_M\Lambda_7)}.\end{aligned}\quad (2.38)$$

Hoop stress on the interface are different and given by,

In the matrix:

$$\sigma_{\theta\theta} = \frac{(\Lambda_6 + 2\Lambda_7 - \Lambda_6\Lambda_8)(1 + d)\sigma_0 + 4\mu_1\varepsilon^*}{2(\Lambda_6 + \Lambda_7)} + \frac{(4 - 3\Lambda_6 + \kappa_M\Lambda_6)(1 - d)\sigma_0 \cos 2\theta}{2(1 + \kappa_M\Lambda_6)}, \quad (2.39)$$

In the inhomogeneity:

$$\sigma_{\theta\theta} = \frac{(\Lambda_6 + \Lambda_6\Lambda_8)(1 + d)\sigma_0 - 4\mu_1\varepsilon^*}{2(\Lambda_6 + \Lambda_7)} + \frac{\Lambda_6(1 + \kappa_M)(1 - d)\sigma_0 \cos 2\theta}{2(1 + \kappa_M\Lambda_6)}. \quad (2.40)$$

As can be seen from Eqs. (2.38)-(2.40), the stress state is independent of R_0 in the classical solution. Note that the above solution reduces to the special case that the inhomogeneity is a hole by setting the shear modulus of the inhomogeneity μ_1 to be zero.

2.3 Numerical Results for Elastic Field Around a Circular Hole

Selected numerical results are presented in this and next section based on the surface elastic constants obtained from past studies. Experiments have been performed to determine the surface stress which has an order of 1 N/m [14,44,45,etc.], but the surface elastic constants are difficult to be measured and no results are available at present. The embedded atom method was used by Miller and Shenoy [24] and Shenoy [25] to determine the surface elastic constants. Their results indicated that the surface elastic constants depend on the material type and the surface crystal orientation as shown in Table 2.1 for isotropic surface. Although the surface properties are generally anisotropic, it is assumed that isotropic case is sufficient to illustrate the main features of the size-dependent response. The plane strain case in which the surface effect is represented by the parameters K^S and τ^0 is investigated in the numerical study without loss of any generality. While the following numerical results are not to provide very accurate values, the study is to show the main behavior with surface effects. In the calculations, unless specified otherwise, $K^S = \pm 10\text{N/m}$, $(\lambda^S + \tau^0) = \pm 10\text{N/m}$ and τ^0 is between -1N/m and 1N/m .

Table 2.1 Surface elastic constants. Units are N/m.

Surface	μ^S	λ^S	τ^0	K^S	$\lambda^S + \tau^0$
Al [100]	-5.4251	3.4939	0.5689	-7.9253	4.0628
Al [111]	-0.3760	6.8511	0.9108	5.1882	7.7619
Ni [111]	-0.6729	-1.8585	-0.1153	-3.0730	-1.9738

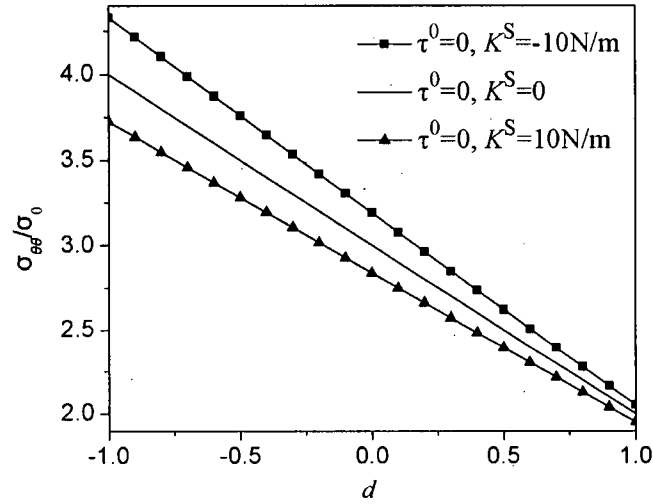
In this section, an infinite plane of aluminum containing a circular hole under far-field loading is considered. The bulk elastic constants for aluminum are: $\lambda_M = 58.17\text{ GPa}$, $\mu_M = 26.13\text{ GPa}$ [46].

Based on the analysis presented in the previous section, hoop stress (plane strain) at $\theta = 0$ on hole surface is given by:

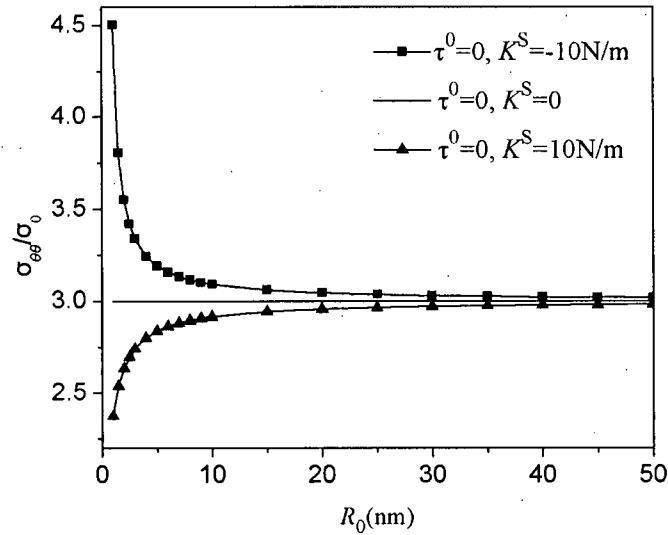
$$\sigma_{\theta\theta} = (3-d)\sigma_0 - \left[\frac{\frac{1}{2}(\Lambda_1\Lambda_2 + 2\Lambda_1)(1+d)}{1+2\Lambda_1} + \frac{3(\Lambda_1\Lambda_2 + 2\Lambda_1)(1-d)}{1+4\Lambda_1 + \Lambda_1\Lambda_2} \right] \sigma_0 - \frac{\tau^0/R_0}{1+2\Lambda_1}. \quad (2.41)$$

Note that the first term is the classical elasticity result and the last two terms represent the surface stress effects and contain non-linear terms of R_0 . The first two terms are linear with respect to the loading magnitude while the third term is independent of external loading and linear with respect to the residual surface stress τ^0 . When $d=1$, i.e., under radially symmetric loading, the result is the same as that obtained by Sharma and Ganti [32]. Following the classical definition, a stress concentration factor can be defined for a hole by normalizing hoop stress at $\theta = 0$ by the remote loading magnitude when $\tau^0 = 0$.

The effect of the surface elastic constant, $K^S = 2\mu^S + \lambda^S - \tau^0$, is first studied by setting $\tau^0 = 0$. In this case based on Eq. (2.41), hoop stress concentration factor ($\sigma_{\theta\theta}/\sigma_0$) is independent of the loading value σ_0 . Fig. 2.2 (a) shows the stress concentration factor for various values of far-field loading ratio d for a hole with radius $R_0 = 5\text{nm}$. Stress concentration factor varies linearly with d and is slightly increased or decreased compared to the classical result ($\tau^0 = 0, K^S = 0$) depending on whether K^S is negative or positive. The influence of K^S appears to be more prominent when d is negative. Fig. 2.2 (b) shows the stress concentration factor for various values of the radius of the hole. The classical solution in which $\tau^0 = 0$ and $K^S = 0$ is, as expected, independent of the radius, while the surface stress effects cause the stress concentration factor to be highly size-dependent especially when the radius is less than 10nm. The stress concentration factor increases or decreases rapidly when the cavity radius is less than 10nm depending on whether K^S is negative or positive. Surface stress effect is negligible when the hole radius is over 15nm and the stress concentration factor is equal to the classical elasticity solution. Similar behavior is observed for other values of d as well.



(a) Radius of the hole $R_0 = 5\text{nm}$



(b) Loading ratio $d=0$

Fig. 2.2. Variation of stress concentration factor at $\theta = 0$.

Variation of nondimensional hoop stress $[\sigma_{\theta\theta}(R_0, \theta)/\sigma_0]$ along the hole surface is shown in Fig. 2.3 with hole radius of 5nm when $\tau^0 = 0$. The results are shown only from $\theta = 0$ to $\theta = \pi/2$ since the elastic field is symmetric with respect to both x and y coordinates. Fig. 2.3 (a) shows the result for the case of uniaxial loading in y -direction ($d=0$) when $\tau^0 = 0$. At $\theta = 0$, the nondimensional stress is reduced for positive K^S and increased for negative K^S compared to the classical result; Opposite behavior is

observed at $\theta = \pi/2$. Similar result can be seen for $d=-1$ which represents pure shear loading [Fig. 2.3 (b)]. Under biaxial loading ($d=1$), the elastic field is radially symmetric and the hoop stress does not vary along the hole. Positive or negative K^S decreases or increases the nondimensional hoop stress and the surface effects can be seen from Fig.2.2 (a) at $d=1$. For other values of loading ratio d , the loading can be seen as a combination of shear and uniaxial loadings when d is negative or biaxial and uniaxial loadings when d is positive.

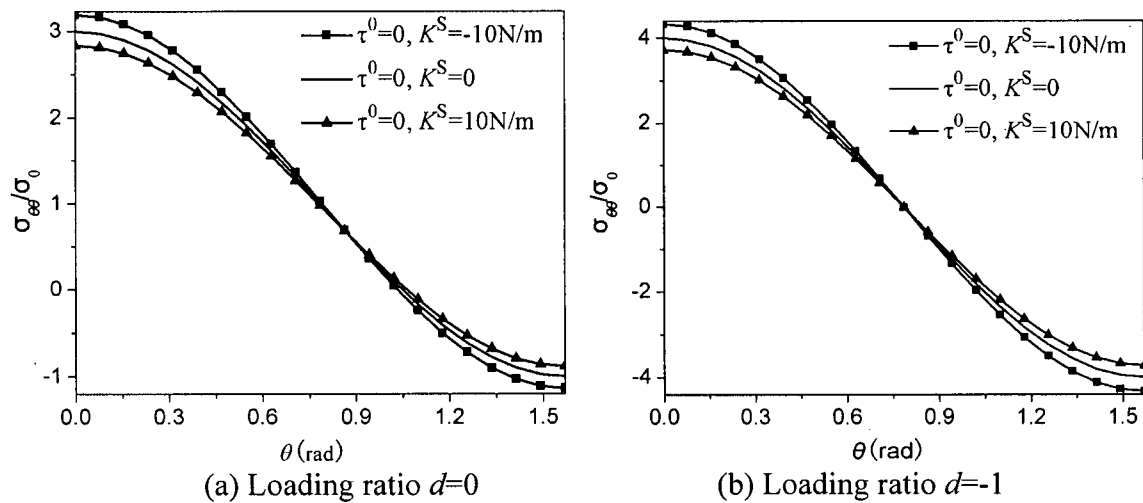
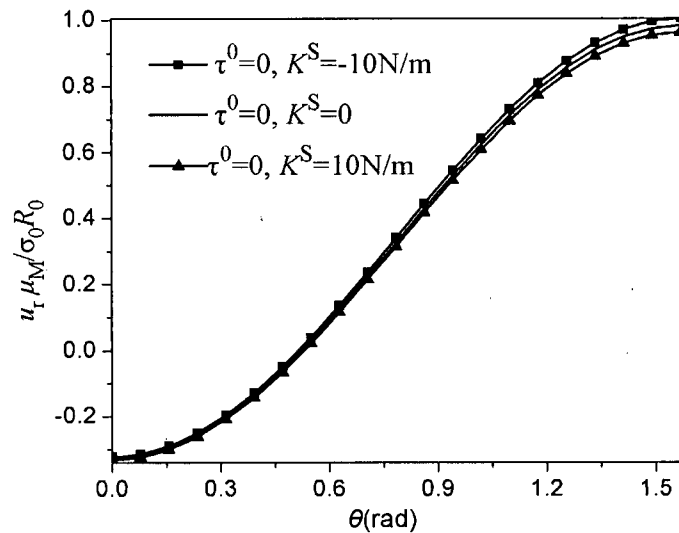


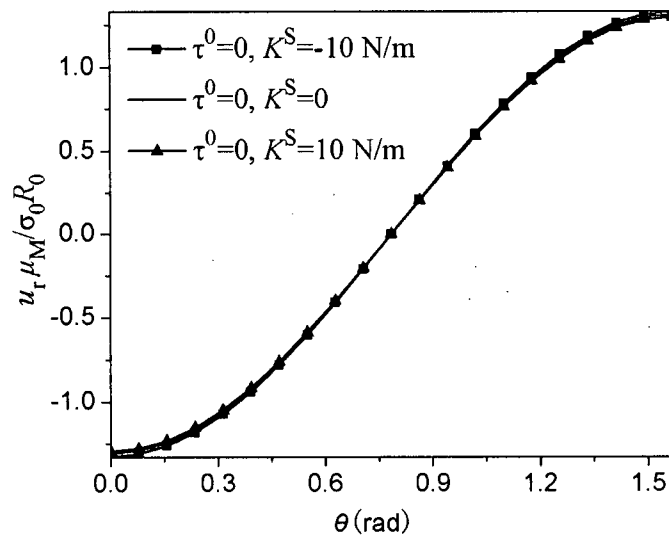
Fig. 2.3. Nondimensional hoop stress along the hole surface ($R_0 = 5\text{nm}$).

Fig. 2.4 shows the nondimensional radial displacement (normalized by $\sigma_0 R_0 / \mu_M$) along the hole with $R_0 = 5\text{nm}$ when $\tau^0 = 0$. Under uniaxial loading in y -direction [Fig. 2.4 (a)], the nondimensional displacement is increased for positive K^S and decreased for negative K^S . When $\sigma_0 > 0$, a positive K^S causes the hole to shrink while a negative K^S causes the hole to expand; opposite phenomena are observed when $\sigma_0 < 0$. Under biaxial loading ($d=1$), the displacement does not vary along the hole and the surface effects are the similar to that under uniaxial loading. Under pure shear loading ($d=-1$), different behavior is observed as shown in Fig. 2.4 (b). When the classical displacement is positive, the displacement is decreased for positive K^S and increased for negative K^S . When the classical displacement is negative, an opposite surface effect is

seen for the same sign of K^S . As a result, no matter whether $\sigma_0 > 0$ or $\sigma_0 < 0$, a positive K^S maintains the circular shape of the hole while a negative K^S distort its shape. These behaviors imply that there exists local hardening or softening in the vicinity of the hole and this is consistent with other studies on the elastic moduli of nanoplate and nanobeam [24,47] and the surface stress effect on a solid containing a nano-scale spherical cavity [33,48].



(a) Loading ratio $d=0$



(b) Loading ratio $d=-1$

Fig. 2.4 Nondimensional radial displacement along the hole surface.

Figure 2.5 shows the variation of nondimensional hoop stress and radial stress along positive x_1 -direction. The surface stress effect is evident near the hole surface but diminishes quite rapidly as x_1 increases especially in the case of hoop stress. Figure 2.5 (b) shows that when compared to the classical solution, the nondimensional radial stress is larger near the hole surface and slightly smaller far from the hole for positive values of K^S . Opposite behavior is noted for negative values of K^S .

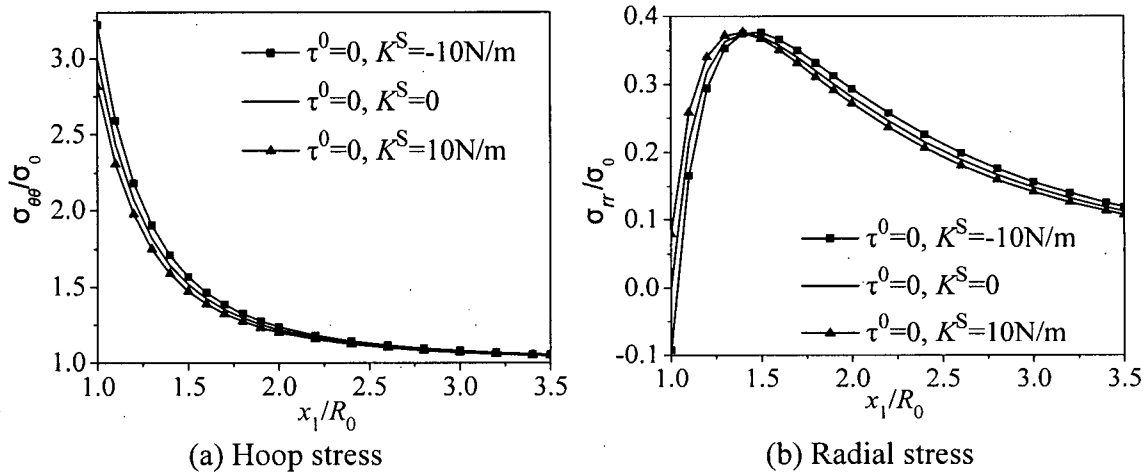


Fig. 2.5 Variation of nondimensional hoop and radial stresses along the x_1 -direction for different K^S ($R_0 = 5\text{nm}$; $d=0$).

Behaviour similar to that shown in Fig 2.2- 2.5 is observed for the case of plane stress. For plane stress, Λ_3 in Eq. (2.30) is nonzero and depends on the surface parameter ($\lambda^S + \tau^0$). In the numerical calculation, $\pm 10\text{N/m}$ is used for this surface parameter. It is noted that the stresses are very close (the difference is less than 4%) to plane strain solutions with K^S equal to 10N/m or -10N/m , and the difference in displacements is little larger (more than 4%).

Consider next only the influence of residual stress τ^0 (the surface stress is a constant value τ^0) on the elastic field of a plane containing a hole. With $\Lambda_1 = \Lambda_3 = 0$, the hoop stress at the hole surface is

$$\sigma_{\theta\theta} = [(1+d) + 2(1-d)\cos 2\theta]\sigma_0 - \tau^0/R_0, \quad (2.42)$$

and the radial displacement at the hole surface is

$$u_r = \frac{\sigma_0 R_0}{\mu_M} \left[\frac{(\kappa_M + 1)(3d - 1)}{8} - \frac{(1 - d) \cos 2\theta}{2} \right] - \frac{\tau^0}{2\mu_M}. \quad (2.43)$$

Note that Eqs. (2.42) and (2.43) apply to both plane stress and plane strain cases. Two second terms on the right hand sides of Eqs. (2.42) and (2.43) are independent of the magnitude of remote loading and correspond to stress due to the residual surface stress. As σ_0 would appear in the denominator of the second term on the right hand side of Eq. (2.42), a stress concentration factor of the classical form is not defined when $\tau^0 \neq 0$. It can be seen that the effect of τ^0 is independent of the loading ratio d and the angle θ . It is clear from Eq. (2.42) that circumferential dependence of hoop stress along the hole surface is given by the classical elasticity solution minus a constant term that is linearly proportional to τ^0 and inversely proportional to hole radius. The radial displacement is also linearly proportional to τ^0 [Eq. (2.43)] and it is obvious that the residual stress τ^0 can increase or decrease the radial displacement depending on the sign of τ^0 . Therefore, the residual stress also causes local hardening or softening around the hole and this is also observed for a solid with a spherical hole [40].

To show the effect of τ^0 on the stresses along x_1 -axis, let $\sigma_{\theta\theta}^C$ and σ_{rr}^C denote hoop and radial stresses corresponding to the classical elasticity solution respectively and let $\sigma_{\theta\theta}^S$ and σ_{rr}^S denote hoop and radial stresses due to the residual surface stress. Fig. 2.6 shows the variation of $\sigma_{\theta\theta}^C$ and σ_{rr}^C normalized by σ_0 and $\sigma_{\theta\theta}^S$ and σ_{rr}^S normalized by τ^0/R_0 along the positive x_1 -direction under uniaxial loading. Again, the residual surface stress shows significant influence on stress field in the vicinity of the hole surface. Its effect is negligible at a distant greater than four times the hole radius. Note that $\sigma_{\theta\theta}^S$ and σ_{rr}^S along x_1 are proportional to $-\frac{\tau^0}{R_0} \left(\frac{x_1}{R_0} \right)^{-2}$ and $\frac{\tau^0}{R_0} \left(\frac{x_1}{R_0} \right)^{-2}$ respectively when $K^S = 0$.

Hence, the nondimensional stress components due to τ^0 shown in Fig.2.6 are independent of the radius R_0 .

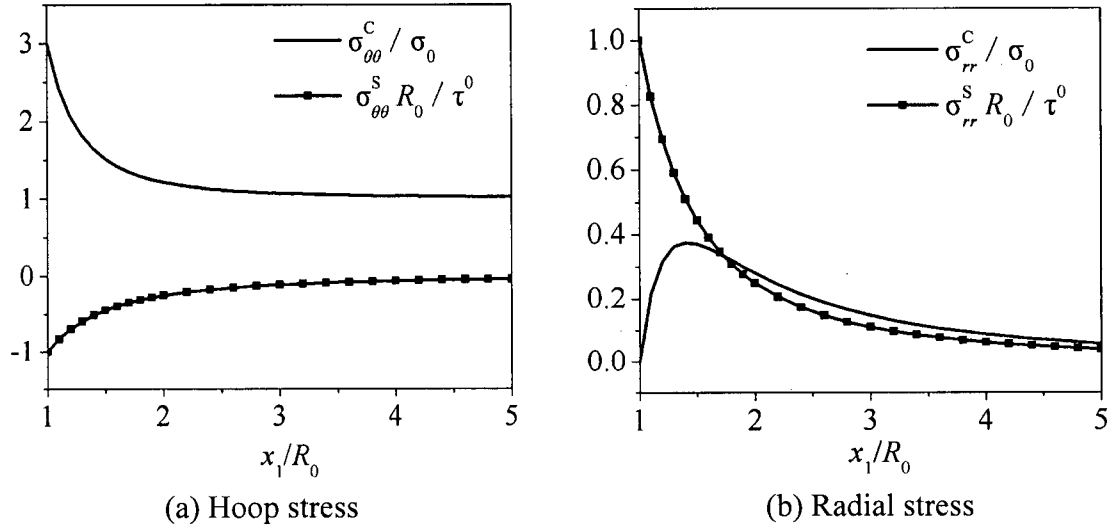


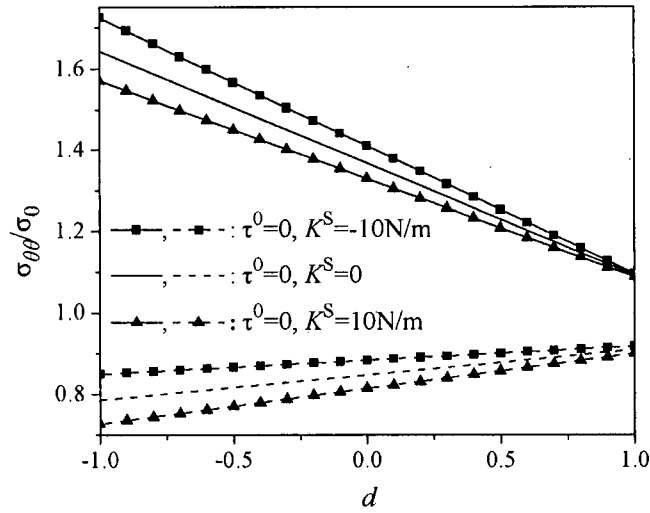
Fig. 2.6 Variation of nondimensional hoop and radial stress components along the x_1 -direction for a hole with residual surface stress ($\tau^0 \neq 0$; $d=0$).

2.4 Numerical Results for Elastic field of a Circular Inhomogeneity

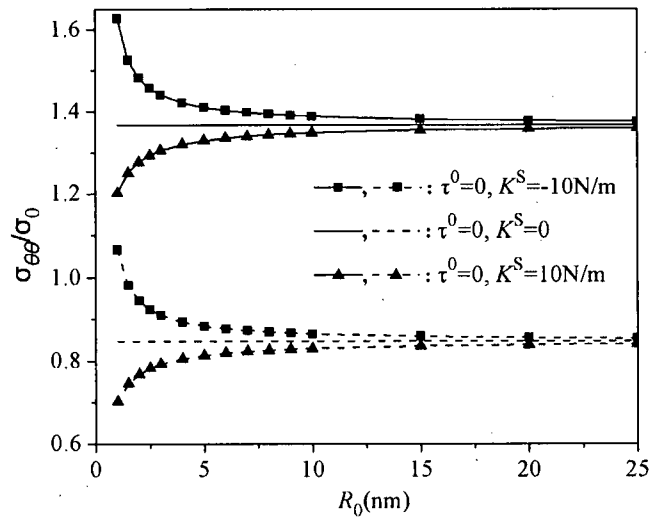
In recent years, quantum dot and wire structures have attracted considerable attention due to their potential application in nanotechnology [8]. It is also well known that mechanical and opto-electronic properties of nanocomposites are significantly influenced by the elastic field of the inhomogeneities. It is therefore important to understand the elastic field of a nanoscale inhomogeneity in a matrix material. To show the surface/interface effect on the elastic field, a matrix-inhomogeneity system made out of InAs/GaAs is considered in this section. The bulk Lamé constants used are: $\lambda_1 = 50.66 \text{ GPa}$, $\mu_1 = 19.0 \text{ GPa}$ for InAs, and $\lambda_M = 64.43 \text{ GPa}$, $\mu_M = 32.9 \text{ GPa}$ for GaAs [49].

Consider first the case of a GaAs plane subjected to far-field loading with no eigenstrain in the InAs inhomogeneity. Hoop stress at the point $\theta = 0$ on the interface is investigated. Fig. 2.7 (a) shows the nondimensional interfacial hoop stress of the inhomogeneity and the matrix for various values of d . The results are similar to that of a circular hole [Fig. 2.2 (a)] and the effect of K^S is slightly more prominent in the inhomogeneity than in the matrix. When $d=-1$ and $K^S = 10 \text{ N/m}$, the differences between the present and the classical results are 7% for the inhomogeneity and 4.5% for the matrix. Fig. 2.7 (b) shows the nondimensional hoop stress for different values of the

inhomogeneity radius with loading ratio $d=0$. Similar to the case of a circular hole, the surface stress effect is significant when the inhomogeneity radius is less than 10nm. Similar behavior can be observed for other values of d as well.



(a) Inhomogeneity radius $R_0 = 5$ nm

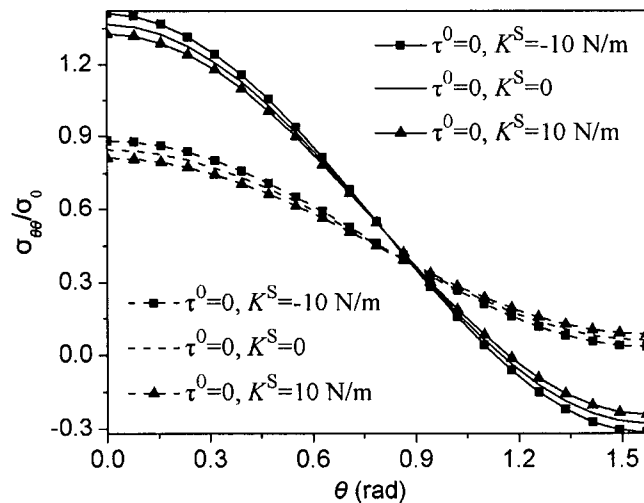


(b) Loading ratio $\alpha=0$

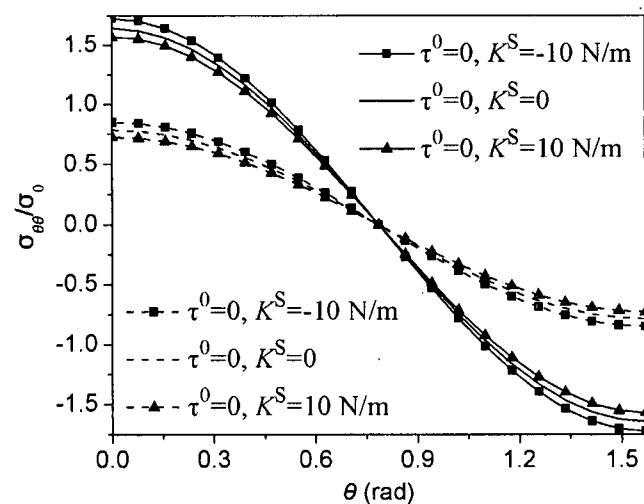
Fig. 2.7 Variation of nondimensional interfacial hoop stress at $\theta = 0$ with loading ratio or inhomogeneity radius (solid lines for matrix and dash lines for inhomogeneity).

Fig. 2.8 shows the nondimensional hoop stress along the inhomogeneity-matrix interface with $R_0 = 5$ nm. The surface stress effects are similar to the case of a circular hole. For $d=0$ and $d=-1$, a positive (negative) K^S decreases (increases) the stress at $\theta = 0$

and increases (decreases) the stress at $\theta = \pi/2$ in both matrix and inhomogeneity. Under biaxial loading ($d=1$), the stress is radially symmetric and increases or decreases depending on the sign of K^S . The solutions for displacements are also very similar to the case of a circular hole.



(a) Loading ratio $d=0$



(b) Loading ratio $d=-1$

Fig. 2.8 Nondimensional hoop stress along the inhomogeneity/matrix interface (solid lines for matrix and dash lines for inhomogeneity).

The influence of eigenstrain ε^* in the inhomogeneity is now considered in the absence of far-field loading. In this case, the stress field is radially symmetric and there is

no shear stress. It is noted that Eshelby's tensor is uniform in this case but also size-dependent due to surface stress effect. Fig. 2.9 shows the nondimensional hoop stress $\sigma_{\theta\theta}/\mu_1\varepsilon^*$ at the inhomogeneity-matrix interface. The nondimensional hoop stress is tensile in the matrix, while it is compressive in the inhomogeneity. In the classical case, hoop stress in the inhomogeneity and matrix have the same absolute value but opposite signs. Size-dependent behavior of hoop stress is clearly evident for an inhomogeneity with a radius smaller than 15nm.

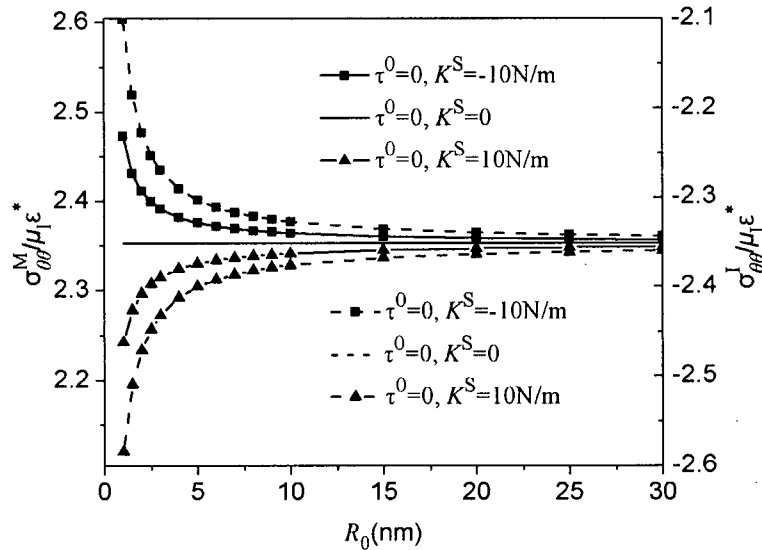


Fig. 2.9 Variation of nondimensional interfacial hoop stress due to an eigenstrain ε^* with inhomogeneity radius (solid lines and left Y-axis for matrix, and dash lines and right Y-axis for inhomogeneity).

Not presented here are the results for an inhomogeneity/matrix system subjected to both far-field loading and an eigenstrain in the inhomogeneity. However, it can be seen from Eqs. (2.31)-(2.34) that the elastic field components are linear functions of eigenstrain ε^* and loading ratio d (or A and B) and the superposition principle can be employed to obtain the solution. The effect of τ^0 is not discussed here for an eigenstrain. It is clear from Eqs. (2.36) and (2.37) that the effect of τ^0 is very similar to the case of a circular hole. In addition, the solution for plane stress is very close to that of plane strain for a prescribed eigenstrain.

Chapter 3

ELASTIC FIELD OF AN INFINITE MATRIX WITH A NANOSACLE ELLIPTICAL INHOMOGENEITY

3.1 Problem Description

In this chapter, a two-dimensional problem of the elastic field solution for a matrix material containing nanoscale elliptical inhomogeneities at dilute distribution is considered. As in Chapter 2, the surface stress effects need to be incorporated and the interaction between inhomogeneities is neglected. This problem can be idealized as an infinite plane containing a single nanoscale elliptical inhomogeneity. The case of an elliptical inhomogeneity is more practically useful than a circular inclusion. On the other hand, the solution for an elliptical inhomogeneity cannot be expressed in closed-form and the salient feature of the elastic field can only be studied by numerical means.

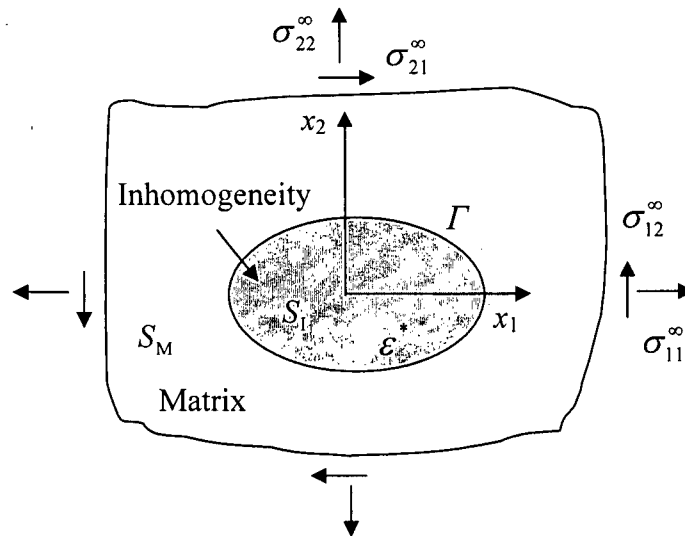


Fig. 3.1. A nanoscale elliptical inhomogeneity in an infinite matrix.

In the current study, the plane is subjected to uniform far-field tractions σ_{11}^∞ , σ_{22}^∞ and σ_{12}^∞ and a prescribed uniform eigenstrain ε^* in the inhomogeneity (Fig. 3.1), and the matrix and inhomogeneity materials are assumed to be linearly elastic, homogeneous and

isotropic with Lamé constants λ_M, μ_M and λ_1, μ_1 , respectively. The matrix occupies a region denoted by S_M , and the inhomogeneity, with the center at the origin of the coordinate system, occupies a region denoted by S_I . The ellipse Γ represents the matrix-inhomogeneity interface.

3.2 Solution of Elastic Field

The complex potential function method of Muskhelishvili [43] is employed to study the two-dimensional inhomogeneity problem under consideration. For plane problems, the displacement and stress components in Cartesian coordinates (x_1, x_2, x_3) can be expressed in terms of two analytic functions $\phi(z)$ and $\psi(z)$ as shown in Eqs. (2.4)-(2.6). At the interface Γ , the boundary displacements and tractions can be written in the normal-tangential coordinates (n, t) as:

$$2\mu(u_n + iu_t) = \left[\kappa\phi(z) - z\overline{\phi'(z)} - \overline{\psi(z)} \right] e^{-i\alpha}, \quad (3.1)$$

$$\sigma_{nn} - i\sigma_{nt} = \phi'(z) + \overline{\phi'(z)} - \left[\bar{z}\phi''(z) + \psi'(z) \right] e^{2i\alpha}, \quad (3.2)$$

where t is the unit tangent, and n is the outward unit normal at the interface which in complex form is $e^{i\alpha}$ (where α is the angle between the normal direction n and the positive x_1 -axis).

Assume that there is perfect bonding at the inhomogeneity-matrix interface, then the displacements are continuous at the interface:

$$(u_n + iu_t)_M = (u_n + iu_t)_I + (u_n + iu_t)_I^*, \quad \text{on } \Gamma, \quad (3.3)$$

where the last term is the displacement induced by the prescribed uniform dilatational eigenstrain ε^* , i.e., $\varepsilon_{11}^* = \varepsilon_{22}^* = \varepsilon^*$, and:

$$(u_n + iu_t)_I^* = z\varepsilon^* e^{-i\alpha}, \quad \text{on } \Gamma. \quad (3.4)$$

The surface traction on the inhomogeneity-matrix interface is discontinuous due to the surface stress effect. For isotropic bulk and interface, the field equations and constitutive relations based on the theory proposed by Gurtin and Murdoch [26] and Gurtin et al. [27] are given in Eqs. (2.8)-(2.11). In the (n, t, x_3) coordinates [x_3 is the

direction perpendicular to the (n, t) -plane], the equilibrium equations (2.9) and (2.10) can be written as:

On the surface/interface Γ :

$$\text{In } t\text{-direction: } \left[\left[\sigma_{nt}^B \right] \right] + \frac{\partial \sigma_{tt}^S}{\partial t} + \frac{\partial \sigma_{3t}^S}{\partial x_3} = 0, \quad (3.5)$$

$$\text{In } x_3\text{-direction: } \left[\left[\sigma_{n3}^B \right] \right] + \frac{\partial \sigma_{33}^S}{\partial x_3} + \frac{\partial \sigma_{t3}^S}{\partial t} = 0, \quad (3.6)$$

$$\text{In } n\text{-direction: } \left[\left[\sigma_{nn}^B \right] \right] = \frac{\sigma_{tt}^S}{R_0}, \quad (3.7)$$

where R_0 is the curvature radius. For plane problems, $\sigma_{n3}^B = \sigma_{3t}^S = \sigma_{t3}^S = 0$ and the derivatives with respect to x_3 are zero. Thus Eq. (3.6) is automatically satisfied. Eqs. (3.5) and (3.7) can be expressed in the following complex variable form:

$$\left[\left[\sigma_{nn}^B - i \sigma_{nt}^B \right] \right] = \frac{\sigma_{tt}^S}{R_0} + i \frac{\partial \sigma_{tt}^S}{\partial t}. \quad (3.8)$$

The left-hand side of Eq. (3.8) can be obtained from Eq. (3.2). For the right-hand side, the surface normal stress in the tangential direction is:

$$\sigma_{tt}^S = \tau^0 + 2(\mu^S - \tau^0)\varepsilon_{tt} + (\lambda^S + \tau^0)(\varepsilon_{33} + \varepsilon_{tt}), \quad \text{on } \Gamma. \quad (3.9)$$

Special attention is required when calculating the strain ε_{33} at the interface, because the strain at either side of the interface can be different even though the displacement is continuous as assumed. Thus the interface has associated with it two interface stresses. Here, the average of the two interface stresses is taken as this is consistent with the case of a spherical inhomogeneity in which the interface stress is continuous and only one interface stress or the average of the two is used in Eq. (3.8) [32]. In the case of a hole, there is only one interface stress, or more exactly, the surface stress, and only this stress appears in the right-hand side of Eq. (3.8).

Tangential elastic strain at the surface ε_{tt} can be obtained from the following equations:

$$\varepsilon_{tt} + \varepsilon_{nn} = \varepsilon_{11} + \varepsilon_{22} = \frac{1}{Q} \left(\phi'(z) + \overline{\phi'(z)} \right), \quad \text{on } \Gamma, \quad (3.10)$$

$$\varepsilon_{ii} - \varepsilon_{mm} + 2i\varepsilon_{im} = (\varepsilon_{22} - \varepsilon_{11} + 2i\varepsilon_{12})e^{2i\alpha} = \frac{1}{\mu} [\bar{z}\phi''(z) + \psi'(z)]e^{2i\alpha}, \quad \text{on } \Gamma. \quad (3.11)$$

Here, $Q = \lambda + \mu$ for plane strain and $\mu(3\lambda + 2\mu)/(\lambda + 2\mu)$ for plane stress. Therefore,

$$\varepsilon_{ii} = \frac{1}{2Q} (\phi'(z) + \overline{\phi'(z)}) + \frac{1}{4\mu} [\bar{z}\phi''(z) + \psi'(z)]e^{2i\alpha} + \frac{1}{4\mu} [z\overline{\phi''(z)} + \overline{\psi'(z)}]e^{-2i\alpha}. \quad (3.12)$$

In the matrix, the elastic strain ε_{ii} is also the actual strain. In the inhomogeneity, due to the eigenstrain effect, $(\varepsilon_{ii})_I = (\varepsilon_{ii})_I^e + \varepsilon^*$, where $(\varepsilon_{ii})_I^e$ is the elastic strain in the inhomogeneity which can be obtained from Eq. (3.12).

For the other strain in Eq. (3.8), $\varepsilon_{33} = 0$ for plane strain in both matrix and inhomogeneity, and for plane stress $(\varepsilon_{33})_M = \nu_M(\varepsilon_{mm} + \varepsilon_{ii})_M^e / (\nu_M - 1)$ in the matrix and $(\varepsilon_{33})_I = \nu_I[(\varepsilon_{mm} + \varepsilon_{ii})_I^e + 2\varepsilon^*] / (\nu_I - 1)$ in the inhomogeneity. Here $(\varepsilon_{mm} + \varepsilon_{ii})_M^e$ and $(\varepsilon_{mm} + \varepsilon_{ii})_I^e$ are the elastic strain in the matrix and inhomogeneity respectively which can be obtained by using Eq. (3.10).

Following Muskhelishvili [43] and England [50], introduce the following mapping function to simplify the geometry of the problem (Fig. 3.2):

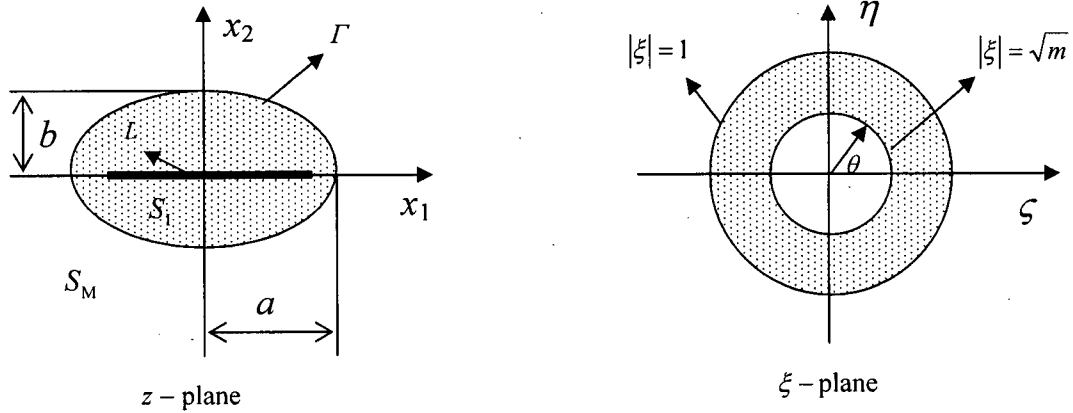


Fig. 3.2. Conformal mapping from z -plane to ξ -plane.

$$z = m(\xi) = R\left(\xi + \frac{m}{\xi}\right), \quad \sqrt{m}\xi = \frac{z}{l} \left\{ 1 + \left[1 - \left(\frac{l}{z}\right)^2 \right]^{1/2} \right\}, \quad \xi = \zeta + i\eta = re^{i\theta}. \quad (3.13)$$

Here,

$$R = \frac{a+b}{2}, \quad m = \frac{1-a/b}{1+a/b} \quad \text{and} \quad l = \sqrt{a^2 - b^2}, \quad (3.14)$$

where a and b are the length of semi-axes of the ellipse and $0 \leq m \leq 1$.

When $m=0$ the ellipse becomes a circle and in the limit $m=1$ it becomes a crack. The mapping function transforms region S_M into the exterior region of the unit circle ($|\xi| = 1$) and region S_I into an annular region between the unit circle and a circle of radius $|\xi| = \sqrt{m}$. Here the region S_I is imagined to be cut along the line $L = \{(x_1, 0) : -l \leq x_1 \leq l\}$ which is transformed into the circle with radius $|\xi| = \sqrt{m}$.

Assume that there are no singularity points in the region S_I , then $\phi_1(z)$ and $\psi_1(z)$ must be holomorphic in region S_I and

$$\phi_1(z) = \phi_1(\bar{z}), \quad \psi_1(z) = \psi_1(\bar{z}), \quad z \in L. \quad (3.15)$$

Consequently, the conditions (3.15) ensure that $\phi_1(z)$ and $\psi_1(z)$ are analytic functions throughout the region S_I .

Now take $\phi(\xi) = \phi(m(\xi))$, and $\psi(\xi) = \psi(m(\xi))$ in the mapped ξ -plane. Therefore, the conditions (3.15) become:

$$\phi_1(\xi) = \phi_1(\bar{\xi}), \quad \psi_1(\xi) = \psi_1(\bar{\xi}), \quad \forall \xi : |\xi| = \sqrt{m}. \quad (3.16)$$

The complex potentials $\phi_M(\xi)$, $\phi_1(\xi)$, $\psi_M(\xi)$ and $\psi_1(\xi)$ corresponding to the matrix and inhomogeneity are now expanded into the following Laurent series form.

$$\phi_M(\xi) = A\xi + \sum_{n=1}^{\infty} A_n \xi^{-n}, \quad \psi_M(\xi) = B\xi + \sum_{n=1}^{\infty} B_n \xi^{-n}, \quad (3.17)$$

$$\phi_1(\xi) = \sum_{n=1}^{\infty} (E_n \xi^n + F_n \xi^{-n}), \quad \psi_1(\xi) = \sum_{n=1}^{\infty} (G_n \xi^n + H_n \xi^{-n}). \quad (3.18)$$

Note that the constant terms have been omitted in Eqs. (3.17) and (3.18) since they represent the rigid body displacements and have no effect on the stress distribution. A and B are given constants characterizing the remote stress field. In view of Eqs. (2.5) and (2.6),

$$\sigma_{11}^{\infty} + \sigma_{22}^{\infty} = \frac{2(A + \bar{A})}{R}, \quad \sigma_{22}^{\infty} - \sigma_{11}^{\infty} + 2i\sigma_{12}^{\infty} = \frac{2B}{R}, \quad (3.19)$$

where σ_{11}^{∞} , σ_{22}^{∞} and σ_{12}^{∞} are the far-field stresses.

According to England [50], the imaginary part of A is related to the rotation ω_{∞} at infinity and,

$$\omega_{\infty} = (1 + \kappa) \text{Im}(A) / 2\mu. \quad (3.20)$$

In the current problem, the rotation is zero, so that:

$$A = \bar{A}. \quad (3.21)$$

Following Stagni [51] and Shen et al. [52], introduce an auxiliary functions $\Omega(\xi)$ and a new auxiliary function $\Theta(\xi)$ such that,

$$\Omega(\xi) = \frac{\overline{m(1/\bar{\xi})}}{m'(\xi)} \phi'(\xi) + \psi(\xi), \quad (3.22)$$

$$\Theta(\xi) = \Omega'(\xi) m'(\xi) - \phi'(\xi) \left[\overline{m(1/\bar{\xi})} \right]. \quad (3.23)$$

The auxiliary functions $\Omega_M(\xi)$, $\Theta_M(\xi)$, $\Omega_1(\xi)$ and $\Theta_1(\xi)$ corresponding to the matrix and inhomogeneity can also be expanded into Laurent series as:

$$\Omega_M(\xi) = C\xi + C_0 + \sum_{n=1}^{\infty} C_n \xi^{-n}, \quad \Theta_M(\xi) = \left(D\xi + D_0 + \sum_{n=1}^{\infty} D_n \xi^{-n} \right) R, \quad (3.24)$$

$$\Omega_1(\xi) = L_0 + \sum_{n=1}^{\infty} (L_n \xi^n + M_n \xi^{-n}), \quad \Theta_1(\xi) = \left[O_0 + \sum_{n=1}^{\infty} (O_n \xi^n + P_n \xi^{-n}) \right] R. \quad (3.25)$$

Eq. (3.24) combined with Eqs. (3.17), (3.22) and (3.23) leads to the following relations:

$$C = mA + B, \quad C_0 = 0, \quad (3.26)$$

$$D = 0, \quad D_0 = B,$$

$$D_1 = 0, \quad D_2 = -Cm - C_1 + A + mA_1, \quad D_3 = -2C_2 + 2mA_2,$$

$$D_{n+3} = -(n+2)C_{n+2} + mnC_n + m(n+2)A_{n+2} - nA_n, \quad (n=1, 2, 3\dots). \quad (3.27)$$

Eq. (3.25) combined with Eqs. (3.18) and (3.23) gives the following relations between the coefficients O_n , P_n and E_n , F_n , L_n and M_n .

$$O_0 = -3mL_3 + L_1 + 3E_3 - mE_1,$$

$$O_n = -(n+3)mL_{n+3} + (n+1)L_{n+1} + (n+3)E_{n+3} - (n+1)mE_{n+1}, \quad (n=1, 2, 3\dots), \quad (3.28)$$

$$P_1 = -2mL_2 + 2E_2, \quad P_2 = -mL_1 - M_1 + E_1 + mF_1, \quad P_3 = -2M_2 + 2mF_2,$$

$$P_{n+3} = nmM_n - (n+2)M_{n+2} - nF_n + (n+2)mF_{n+2}, \quad (n=1, 2, 3\dots). \quad (3.29)$$

Furthermore, the conditions (3.16) combined with Eqs. (3.18), (3.22) and (3.25) yield the following relations.

$$F_n = m^n E_n, \quad H_n = m^n G_n, \quad M_n = m^n L_n + nm^{n-1}(1-m^2)E_n. \quad (3.30)$$

Using Eqs. (3.1), (3.4) and (3.22), the continuity of displacement across the interface, Eq. (3.3), can be expressed as:

$$\frac{1}{2\mu_M} [\kappa_M \phi_M(\xi) - \overline{\Omega_M(\xi)}] = \frac{1}{2\mu_1} [\kappa_1 \phi_1(\xi) - \overline{\Omega_1(\xi)}] + m(\xi)\varepsilon^*. \quad (3.31)$$

Noting that $\xi = e^{i\theta}$ on the interface, substitute Eqs. (3.17), (3.18), (3.24) and (3.25) into Eq. (3.31) and equate the coefficients of $e^{in\theta}$ to the following relations.

$$L_0 = 0, \quad \Lambda_3(\kappa_M A - \overline{C_1}) = \kappa_1 E_1 - \overline{M_1} + 2\mu_1 R \varepsilon^*,$$

$$\Lambda_3(-\overline{C_{n+1}}) = \kappa_1 E_{n+1} - \overline{M_{n+1}}, \quad (n=1, 2, 3, \dots), \quad (3.32)$$

$$\Lambda_3(\kappa_M A_1 - \overline{C}) = \kappa_1 F_1 - \overline{L_1} + 2\mu_1 R m \varepsilon^*,$$

$$\Lambda_3 \kappa_M A_{n+1} = \kappa_1 F_{n+1} - \overline{L_{n+1}}, \quad (n=1, 2, 3, \dots). \quad (3.33)$$

where $\Lambda_3 = \mu_1 / \mu_M$.

To solve the present problem, it is required to obtain the coefficients including A_n , C_n , D_n , E_n , L_n , O_n and P_n . Once these are known, the other coefficients (B_n , F_n , H_n and M_n) can be determined. Based on the above analysis, D_n can be expressed in terms of A_n and C_n from Eq. (3.27); E_n and L_n can be expressed in terms of A_n and C_n from Eqs. (3.30), (3.32) and (3.33); O_n and P_n can be expressed in terms of E_n and L_n from Eqs. (3.28)-(3.30), and thus in terms of A_n and C_n . The only unknown coefficients are therefore A_n and C_n . Additional relations between the unknowns can be obtained from the boundary condition (3.8) as follows.

In the ξ -plane, following England [50],

$$e^{2i\alpha} = \frac{\xi m'(\xi)}{\overline{\xi m'(\xi)}}, \quad e^{i\alpha} = \frac{\xi m'(\xi)}{|\xi m'(\xi)|}; \quad \xi = e^{i\theta} \text{ on } \Gamma, \quad (3.34)$$

and the derivatives with respect to the tangential direction t can be expressed as:

$$\frac{\partial}{\partial t} = \frac{\partial}{\partial z} \frac{\partial z}{\partial t} + \frac{\partial}{\partial \bar{z}} \frac{\partial \bar{z}}{\partial t} = \frac{\partial}{\partial \xi} \frac{1}{\frac{\partial z}{\partial \xi}} \frac{\partial z}{\partial t} + \frac{\partial}{\partial \bar{\xi}} \frac{1}{\frac{\partial \bar{z}}{\partial \bar{\xi}}} \frac{\partial \bar{z}}{\partial t}, \quad (3.35)$$

$$\frac{\partial z}{\partial t} = ie^{i\alpha}, \quad \frac{\partial \bar{z}}{\partial t} = -ie^{-i\alpha}. \quad (3.36)$$

In the ξ -plane, Eq. (3.2) becomes:

$$\sigma_{nn} - i\sigma_{nt} = \frac{\phi'(\xi)}{m'(\xi)} + \frac{\overline{\phi'(\xi)}}{\overline{m'(\xi)}} - \left\{ \left(\frac{\phi''(\xi)m'(\xi) - \phi'(\xi)m''(\xi)}{[m'(\xi)]^2} \right) \frac{\overline{m'(\xi)}}{m'(\xi)} + \frac{\psi'(\xi)}{m'(\xi)} \right\} e^{2i\theta}, \text{ on } \Gamma.$$

Multiplying the above expression by the (non-vanishing) factor $\overline{m'(\xi)}$, and eliminating $\psi'(\xi)$ by using Eq. (3.22), yields,

$$\overline{m'(\xi)}[\sigma_{nn} - i\sigma_{nt}] = \overline{\phi'(\xi)} - e^{2i\theta} \Omega'(\xi). \quad (3.37)$$

The right-hand side of Eq. (3.8) is written as:

$$\frac{\sigma_{nn}^S}{R_0} + i \frac{\partial \sigma_{nt}^S}{\partial t} = \frac{\frac{1}{2}[(\sigma_{nn}^S)_M + (\sigma_{nn}^S)_I]}{R_0} + i \frac{\partial \left[\frac{1}{2}(\sigma_{nt}^S)_M + \frac{1}{2}(\sigma_{nt}^S)_I \right]}{\partial t}. \quad (3.38)$$

Eq. (3.38) are derived in Appendix A by substituting the interface stresses (3.9) into the above equation and multiplying the resulting expression by a factor $\frac{m'(\xi)\overline{m'(\xi)}/R}{m'(\xi)/R}$.

Consequently, by combining Eqs. (3.17), (3.18), (3.24), (3.25), (3.37) and (A.5), Eq. (3.8) becomes:

$$\begin{aligned} & \sum_{n=1}^{\infty} n(C_n - \bar{E}_n - M_n) e^{-i(n-1)\theta} + A - Ce^{2i\theta} - \sum_{n=1}^{\infty} n(\bar{A}_n - \bar{F}_n - L_n) e^{i(n+1)\theta} \\ &= \frac{1}{m'(\xi)/R} \frac{1}{|\overline{m'(\xi)}/R|^3} [g_0 + h_0 + (g_1 + h_1)e^{-i\theta} + (g_2 + h_2)e^{i\theta} + (g_3 + h_3)e^{-2i\theta} \\ & \quad + (g_4 + h_4)e^{2i\theta} + (g_5 + h_5)e^{-3i\theta} + (g_6 + h_6)e^{3i\theta} + h_7e^{-4i\theta} + h_8e^{4i\theta}] \end{aligned}$$

$$\left. + \sum_{n=1}^{\infty} S_n e^{i(n+3)\theta} + \sum_{n=1}^{\infty} T_n e^{-i(n+3)\theta} + \sum_{n=1}^{\infty} U_n e^{i(n+4)\theta} + \sum_{n=1}^{\infty} V_n e^{-i(n+4)\theta} \right]. \quad (3.39)$$

Here, the coefficients g_0 , g_n ($n=1,2,\dots,6$), h_n ($n=1,2,\dots,8$), S_n , T_n , U_n and V_n are defined in Appendix A.

It can be seen that these coefficients are functions of the nondimensional parameters Λ_1 and Λ_4 or Λ_5 and Λ_6 which are defined as the ratios of the intrinsic lengths to the characteristic length of the material (the inhomogeneity size), and therefore, these parameters and the residual stress τ^0 represent the surface effects.

Next, employing a method similar to that used by Shen et al. [53], $1/|m'(\xi)/R|^3$ can be expanded into an infinite series of the following form (see Appendix C).

$$\frac{1}{|m'(\xi)/R|^3} = \frac{1}{(1-m)^3} (1+b^* \sin^2 \theta)^{-3/2}, \quad b^* = \frac{4m}{(1-m)^2}, \quad (3.40)$$

$$\begin{aligned} (1+b^* \sin^2 \theta)^{-3/2} &= I_0 + \sum_{k=1}^{\infty} I_{2k} (e^{i2k\theta} + e^{-i2k\theta}) \\ &\cong I_0 + \sum_{k=1}^{J-1} I_{2k} (e^{i2k\theta} + e^{-i2k\theta}) + I_{2J} \frac{e^{i2J\theta} + e^{-i2J\theta} - m(e^{i2(J-1)\theta} + e^{i2(1-J)\theta})}{(1-me^{2i\theta})(1-me^{-2i\theta})}. \end{aligned} \quad (3.41)$$

Eq. (3.41) can be rewritten as:

$$(1+b^* \sin^2 \theta)^{-3/2} \cong \frac{1}{(1-me^{2i\theta})(1-me^{-2i\theta})} \left[f_0 + \sum_{k=1}^J f_{2k} (e^{i2k\theta} + e^{-i2k\theta}) \right], \quad (3.42)$$

where

$$\begin{aligned} f_0 &= (1+m^2)I_0 - 2mI_2, \\ f_{2k} &= (1+m^2)I_{2k} - mI_{2k-2} - mI_{2k+2}, \quad (k=1, 2, \dots, J-1), \\ f_{2J} &= I_{2J} - mI_{2J-2}. \end{aligned} \quad (3.43)$$

Take the denominator $(1-me^{2i\theta})(1-me^{-2i\theta})$ into the first term of the right-hand side of Eq. (3.39), i.e., $\frac{1}{m'(\xi)/R}$, and expand it into power series of the following form

(see Appendix D):

$$\frac{1}{m'(\xi)/R} \frac{1}{(1-me^{2i\theta})(1-me^{-2i\theta})} = \frac{1}{(1-m^2)^2} \left[\sum_{n=1}^{\infty} m^n e^{i2n\theta} + 1 + \sum_{n=1}^{\infty} (m^n + (1-m^2)nm^n) e^{-i2n\theta} \right]. \quad (3.44)$$

Thereafter, using Eqs. (3.40), (3.42) and (3.44), Eq. (3.39) becomes

$$\begin{aligned} & \sum_{n=1}^{\infty} n(C_n - \bar{E}_n - M_n) e^{-i(n-1)\theta} + A - Ce^{2i\theta} - \sum_{n=1}^{\infty} n(\bar{A}_n - \bar{F}_n - L_n) e^{i(n+1)\theta} \\ &= \frac{1}{(1-m)^3(1-m^2)^2} \left[\sum_{n=1}^{\infty} m^n e^{i2n\theta} + 1 + \sum_{n=1}^{\infty} (m^n + (1-m^2)nm^n) e^{-i2n\theta} \right] \\ & \times \left[f_0 + \sum_{k=1}^J f_{2k} (e^{i2k\theta} + e^{-i2k\theta}) \right] \left[g_0 + h_0 + (g_1 + h_1)e^{-i\theta} + (g_2 + h_2)e^{i\theta} + (g_3 + h_3)e^{-2i\theta} \right. \\ & \quad \left. + (g_4 + h_4)e^{2i\theta} + (g_5 + h_5)e^{-3i\theta} + (g_6 + h_6)e^{3i\theta} + h_7 e^{-4i\theta} + h_8 e^{4i\theta} \right. \\ & \quad \left. + \sum_{n=1}^{\infty} S_n e^{i(n+3)\theta} + \sum_{n=1}^{\infty} T_n e^{-i(n+3)\theta} + \sum_{n=1}^{\infty} U_n e^{i(n+4)\theta} + \sum_{n=1}^{\infty} V_n e^{-i(n+4)\theta} \right]. \quad (3.45) \end{aligned}$$

By equating the coefficients of $e^{in\theta}$ in Eq. (3.45), the relationships between the unknown coefficients can be obtained. This yields a sufficient number of equations to solve for the unknown coefficients. Depending on the level of accuracy required, different values of J and the number of the coefficients in the power series, i.e., n , are chosen.

3.3 Numerical Results for Elastic Field Around an Elliptical Hole

Selected numerical results for plane strain case are presented in this and ensuing sections. The surface/interface effects are represented by the residual surface stress, τ^0 , and parameter, K^S (or τ^0 , Λ_1 and Λ_6), and the values of these parameters for numerical calculation are same as in Chapter 2, i.e., $K^S = \pm 10$ N/m and τ^0 is between -1 N/m and 1 N/m. The number of the terms in the infinite series representation of the complex potential functions is chosen so that the error in the numerical calculation is maintained below 1%. This is achieved by increasing the number of terms in the series representation until the difference between two consecutive sums is less than 1%. Accuracy of the numerical calculations is checked by setting the surface elastic constants and residual

surface stress to negligibly small values and comparing the resulting numerical solutions with the classical elasticity solution for an elliptical hole in an infinite plane subjected to remote uni-axial tension. It is found that the two solutions agree very closely.

In this section, an infinite plane of aluminum containing an elliptical hole under far-field loading is considered. The effect of the surface elastic constant, $K^S = 2\mu^S + \lambda^S - \tau^0$, is first studied by setting $\tau^0 = 0$. In this case, the stress concentration factor, $\sigma_{\theta\theta} / \sigma_0$, at $\theta = 0$ is independent of the magnitude of the applied loading. Fig. 3.3 shows the stress concentration factor for various hole sizes $R [(a+b)/2]$ under uniaxial loading with $a/b = 1.5$. As expected the classical solution in which $\tau^0 = 0$ and $K^S = 0$ is independent of the hole size, while the surface stress effects cause the stress concentration factor to be size-dependent especially when R is less than 20nm. The stress concentration factor increases or decreases when $K^S < 0$ or $K^S > 0$. The difference between the classical and current results can reach 27% when $R = 1\text{nm}$ for $K^S > 0$. The surface stress effects are negligible when R is over 40nm and the stress concentration factor is equal to the classical elasticity solution. This behavior is similar to that of the circular case and of the spherical case [31]. However, for $K^S < 0$, the stress is found to become highly oscillatory and singular at some values for R less than 6nm. It is noted that this unstable phenomenon does not happen for $K^S > 0$ in which case the stress becomes smaller as R decreases.

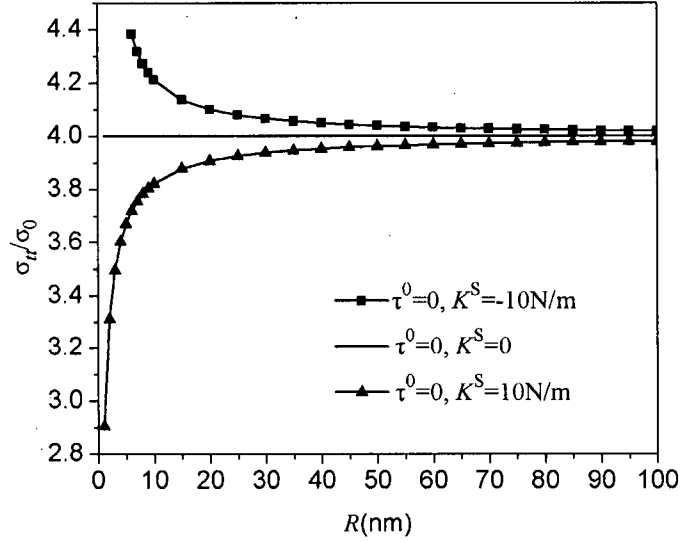


Fig. 3.3. Variation of stress concentration factor at $\theta = 0$ with hole size R and K^S ($a/b=1.5$) under uniaxial loading $\sigma_{yy}^\infty = \sigma_0$.

It is proposed to further investigate this phenomenon by considering the case of a circular hole under uniaxial or biaxial loading. Closed form of analytical solution for the plane strain case is:

$$\frac{\sigma_{\theta\theta}}{\sigma_0} = \frac{1+d}{2} + \frac{1-d}{2} \cos 2\theta - \frac{\frac{1}{2}(\Lambda_1\Lambda_2 - 1)(1+d) + \tau^0/\sigma_0 R_0}{1+2\Lambda_1} - \frac{\frac{3}{2}(\Lambda_1\Lambda_2 - 1)(1-d)}{1+4\Lambda_1 + \Lambda_1\Lambda_2} \cos 2\theta, \quad (3.46)$$

$$\frac{\sigma_{rr}}{\sigma_0} = \frac{1+d}{2} - \frac{\frac{1}{2}(\Lambda_1\Lambda_2 - 1)(1+d) + \tau^0/\sigma_0 R_0}{1+2\Lambda_1} + \frac{(\Lambda_1\Lambda_2 + 2\Lambda_1)(1-d)}{1+4\Lambda_1 + \Lambda_1\Lambda_2} \cos 2\theta, \quad (3.47)$$

$$\begin{aligned} \frac{u_r}{\sigma_0 R_0 / \mu_M} &= \frac{(\kappa_M + 1)(1+d)}{8} - \frac{\frac{1}{2}(\Lambda_1\Lambda_2 - 1)(1+d) + \tau^0/\sigma_0 R_0}{2(1+2\Lambda_1)} - \frac{(1-d)}{4} \cos 2\theta \\ &\quad - \frac{\frac{1}{4}(\kappa_M + 1)(1+2\Lambda_1)(1-d)}{1+4\Lambda_1 + \Lambda_1\Lambda_2} \cos 2\theta - \frac{\frac{1}{4}(\Lambda_1\Lambda_2 - 1)(1-d)}{1+4\Lambda_1 + \Lambda_1\Lambda_2} \cos 2\theta, \end{aligned} \quad (3.48)$$

$$\frac{u_\theta}{\sigma_0 R_0 / \mu_M} = \frac{1-d}{4} \sin 2\theta - \frac{\frac{1}{4}(1-\kappa_M)(1-d)(1+2\Lambda_1)}{1+4\Lambda_1 + \Lambda_1\Lambda_2} \sin 2\theta - \frac{\frac{1}{4}(\Lambda_1\Lambda_2 - 1)(1-d)}{1+4\Lambda_1 + \Lambda_1\Lambda_2} \sin 2\theta. \quad (3.49)$$

Here, σ_0 is the loading stress and R_0 is the radius of the circular hole and $d = 0$ for uniaxial loading and $d = 1$ for biaxial loading. When $K^S < 0$, Λ_1 ($\Lambda_1 = K^S/4\mu_M R_0$ for circular case, see Chapter 2) is negative. Therefore, the denominators containing Λ_1 in Eqs. (3.46)-(3.49) can be zero for certain radii resulting in singular stress and displacement fields. The corresponding radii are very small, less than 1nm, for the values of K^S corresponding to aluminum. A similar phenomenon exist for the elliptical case, however, there appear to be many hole sizes R which induce singular stresses. Some of these R values can be relatively large ($>5\text{nm}$) depending on the geometry of the ellipse, surface elastic constant K^S and elastic properties of the matrix material. Such unstable behavior should not occur in experiments involving real materials because of the plastic properties of nanoscale materials. This implies that Gurtin-Murdoch model has some restrictions when applied to solve situations involving negative K^S values.

Fig. 3.4 shows the stress concentration factor for various hole sizes R with $a/b = 3$ under uniaxial loading. The result is similar to the case of $a/b = 1.5$. However, the effect of the surface elastic constants K^S is more noticeable. The stress concentration factor shows high size-dependency when R is less than 40nm. The difference between the classical and the current results can reach 40% when $R = 1\text{nm}$ for $K^S > 0$. The stress for $K^S < 0$ is unstable below 15nm. It is noted that the results are similar for other values of a/b , and as the value of a/b increases, the effect of the surface elastic constant K^S becomes more pronounced and the value of R below which the stress is unstable when $K^S < 0$ increases.

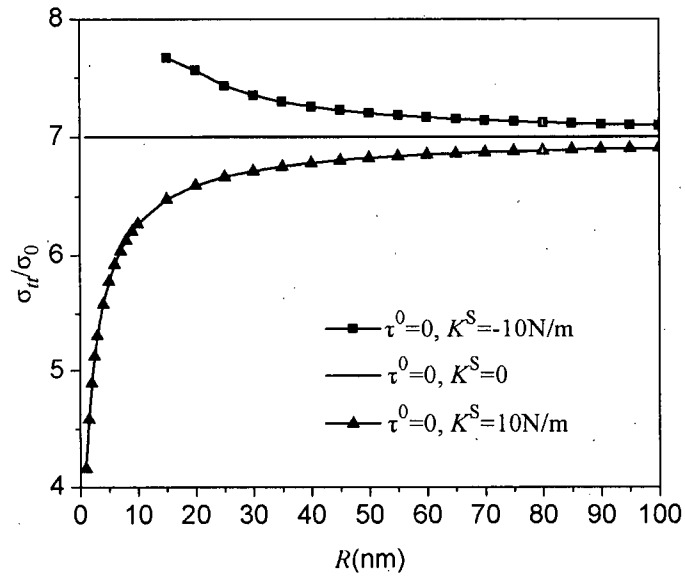


Fig. 3.4. Variation of stress concentration factor at $\theta = 0$ with hole size R and K^S ($a/b=3$) under uniaxial loading $\sigma_{yy}^\infty = \sigma_0$.

Fig. 3.5 shows the nondimensional tangential stress $[\sigma_u(R, \theta)/\sigma_0]$ along the hole with $R=6\text{nm}$ and $a/b=1.5$. The result is shown from $\theta = 0$ to $\theta = \pi/2$ due to symmetry. Under biaxial loading as shown in Fig. 3.5 (a), the nondimensional tangential stress is decreased for positive K^S and increased for negative K^S for the whole surface. Different behavior is observed under uniaxial loading as shown in Fig. 3.5 (b). At $\theta = 0$, the nondimensional tangential stress is reduced for positive K^S and increased for negative K^S , but opposite behavior can be seen at $\theta = \pi/2$. Similar result as uniaxial loading can be observed for shear loading. It is noted that these results are similar to the case of a circular hole.

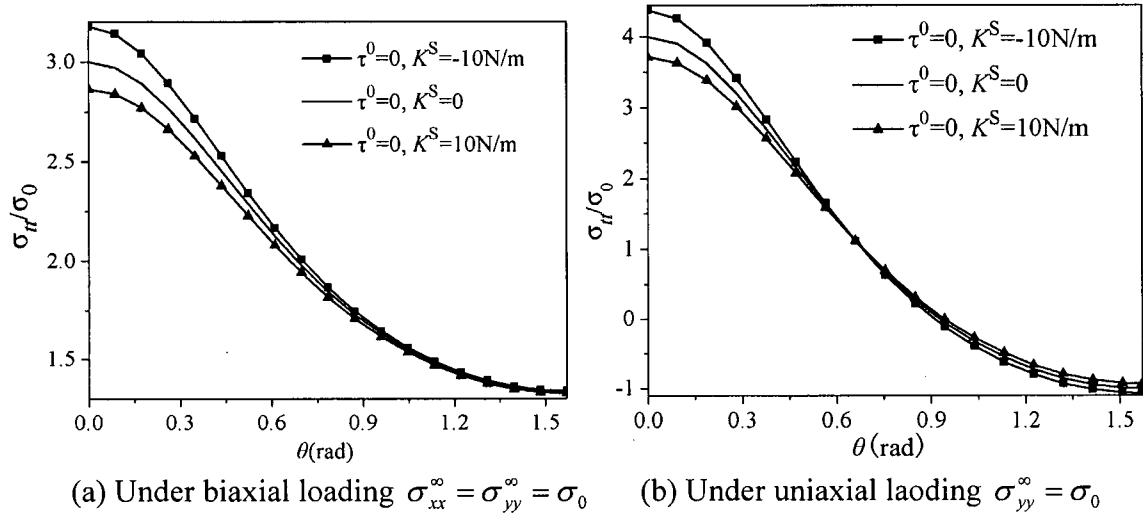
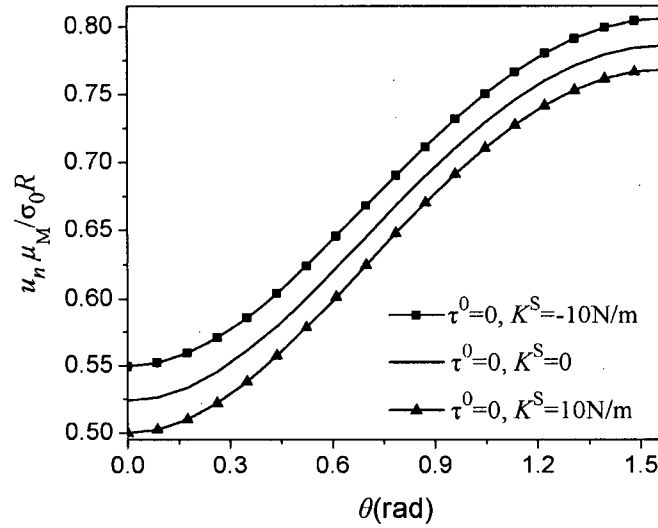
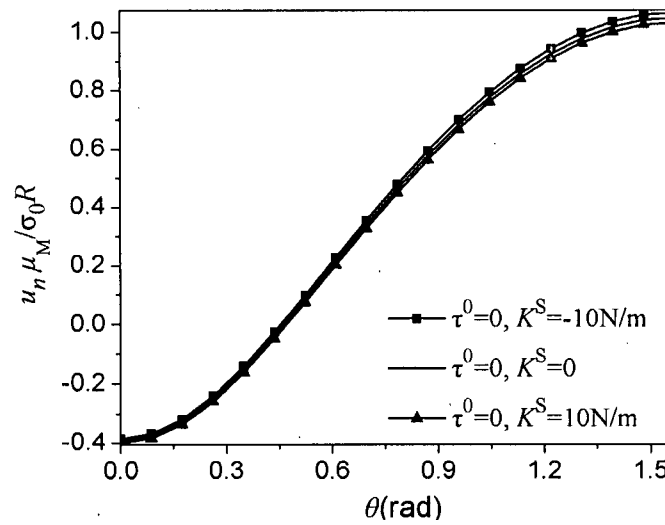


Fig. 3.5. Variation of nondimensional tangential stress along the hole surface with $R=6\text{nm}$ ($a/b=1.5$).

Fig. 3.6 shows the nondimensional normal displacement (normalized by $\sigma_0 R / \mu_M$) along the hole surface for $a/b=1.5$ and $R=10\text{nm}$ under biaxial and uniaxial loading. It can be seen that positive values of surface elastic constant K^S cause the hole to shrink when compared to the classical case (no surface stress effect) while a negative K^S causes the hole to expand more. Similar behavior can be observed in the case of uniaxial loading. Under pure shear loading (figure not shown), the absolute value of normal displacement is decreased or increased when $K^S > 0$ or $K^S < 0$. This is similar to the case of a circular hole. As a result, when K^S is positive the shape of the hole is relatively unchanged while for a negative K^S more shear distortion of the hole takes place. Therefore, the surface elastic constant (K^S) causes local hardening or softening around the hole. A larger positive K^S introduces a larger hardening zone, while smaller negative value of K^S (larger absolute value) introduces a larger softening zone.



(a) Under biaxial loading ($\sigma_{xx}^\infty = \sigma_{yy}^\infty = \sigma_0$)



(b) Under uniaxial loading ($\sigma_{yy}^\infty = \sigma_0$)

Fig. 3.6. Variation of nondimensional normal displacement along the hole surface for different K^S ($a/b=1.5$; $R=6\text{nm}$).

Fig.3.7 shows the variation of stresses σ_{22} and σ_{11} along the positive x_1 -direction. The surface stress effect is significant only near the hole surface but diminishes quite rapidly as x_1 increases especially in the case of σ_{22} . Fig. 3.7 (b) shows that, when compared to the classical solution, the nondimensional stress σ_{11}/σ_0 is higher near the

hole surface but slightly smaller far from the hole for positive values of K^S . Opposite behavior is noted for negative values of K^S . The behavior is similar to the case of a circular hole (Chapter 2).

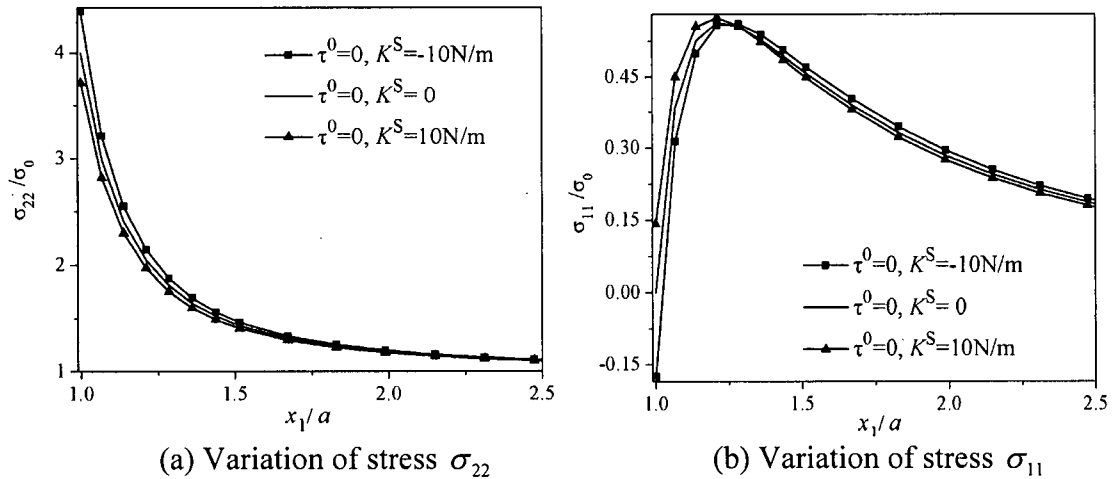


Fig. 3.7. Variation of stress components, σ_{22} and σ_{11} , along the x_1 -direction for different K^S under uniaxial loading $\sigma_{yy}^{\infty} = \sigma_0$ ($a/b=1.5$; $R = 6\text{nm}$).

It is noted that similar phenomena are observed for the case of plane stress and other values of a/b . For plane stress, Λ_4 in Eq. (A.2) is nonzero and depends on the surface parameter ($\lambda^S + \tau^0$). When $\pm 10\text{N/m}$ are used in the numerical calculation for this surface parameter, it can be seen that the results of stresses and displacements for plane stress are very close to that of plane strain for the same parameter K^S (10 N/m or -10 N/m) and the same value of a/b .

Consider next the influence of residual stress τ^0 on the elastic field of a plane containing an elliptical hole by setting $K^S = 0$ (or $\Lambda_1 = 0$). As expected, the effect of τ^0 is similar to that in the case of circular hole as τ^0 behaviors like a loading and is independent of the applied remote loading. The numerical solutions for stress do not show any instability problem with respect to τ^0 . This behaviour can be easily confirmed

from Eq. (2.42) or Eq. (3.46) for the circular case as the denominators cannot be equal to zero.

To show the effect of residual stress, τ^0 , let σ_{22}^C and σ_{11}^C denote the stress components corresponding to the classical elasticity solution respectively, and let σ_{22}^S and σ_{11}^S denote the stress components due to the residual surface stress τ^0 . Fig. 3.8 shows the variation of σ_{22}^C and σ_{11}^C normalized by σ_0 and σ_{22}^S and σ_{11}^S normalized by τ^0/R along the positive x_1 -direction under uniaxial loading when $a/b=1.5$. The residual surface stress shows a significant influence on stress field only in the vicinity of the hole surface. Its effect is negligible at a distant greater than four times the major semi-axis. Note that nondimensional stress components due to τ^0 shown in Fig. 3.8 are independent of R .

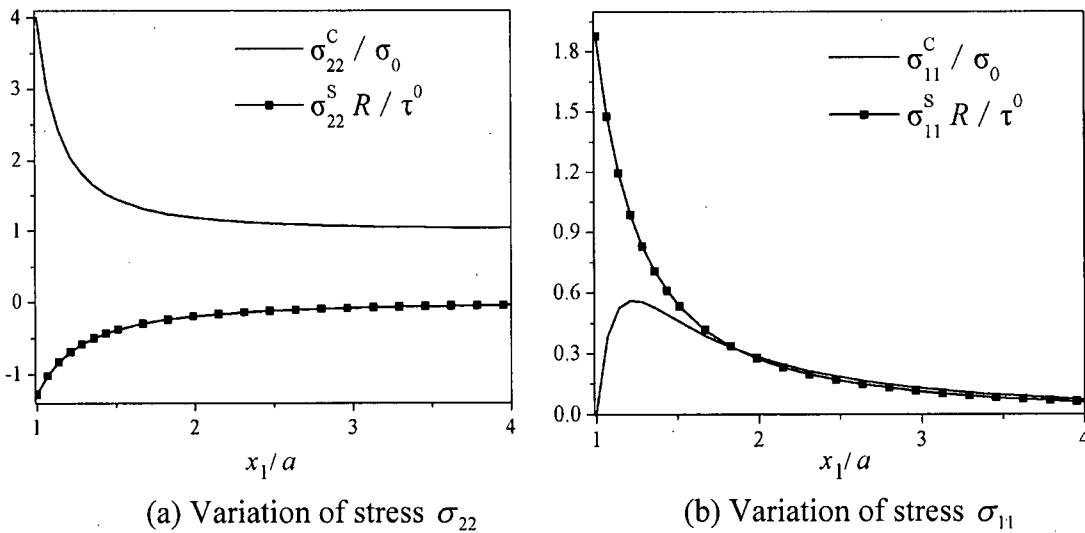


Fig. 3.8. Variation of stress components, σ_{22} and σ_{11} , along the x_1 -direction for a hole with residual surface stress under uniaxial loading $\sigma_{yy}^\infty = \sigma_0$ ($a/b=1.5; \tau^0 \neq 0$).

3.4 Numerical Results for Elastic Field of an Elliptical Inhomogeneity

This section presents results for elastic field of an infinite plane containing a nanoscale elliptical inhomogeneity in the case of plane strain. To show the

surface/interface effect on the elastic field, a matrix-inhomogeneity system made out of InAs/GaAs is considered.

Consider first the case of a GaAs plane subjected to far-field loading with no eigenstrain in the InAs inhomogeneity. The tangential stress σ_{tt} at the point $\theta = 0$ on the interface is investigated. Figs. 3.9 and 3.10 show the nondimensional tangential stress for various values of R with $a/b=1.5$ and $a/b=3$, respectively. The nondimensional tangential stresses in both the inhomogeneity and matrix are increased and decreased when $K^S < 0$ and $K^S > 0$ respectively. The effect of K^S is slightly more prominent in the inhomogeneity than in the matrix. For example, when $R=1\text{nm}$ and $K^S = 10\text{N/m}$ in the case of $a/b=1.5$, the differences between the present and the classical results are 25.5% for the inhomogeneity and 17.5% for the matrix. Similar to the case of an elliptical hole (Figs. 3.3 and 3.4), the effect of K^S is more pronounced as the value of a/b increases. Stresses in both the matrix and inhomogeneity for $K^S < 0$ become unstable below a certain value of R depending on the value of a/b .

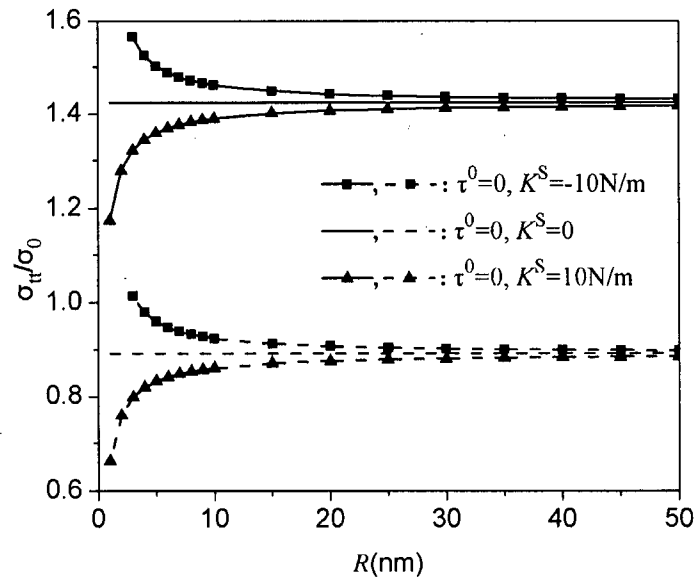


Fig. 3.9. Variation of the nondimensional tangential stress at $\theta = 0$ with the inhomogeneity size R and K^S ($a/b=1.5$) under uniaxial loading ($\sigma_{yy}^\infty = \sigma_0$): solid lines for matrix and dash lines for inhomogeneity.

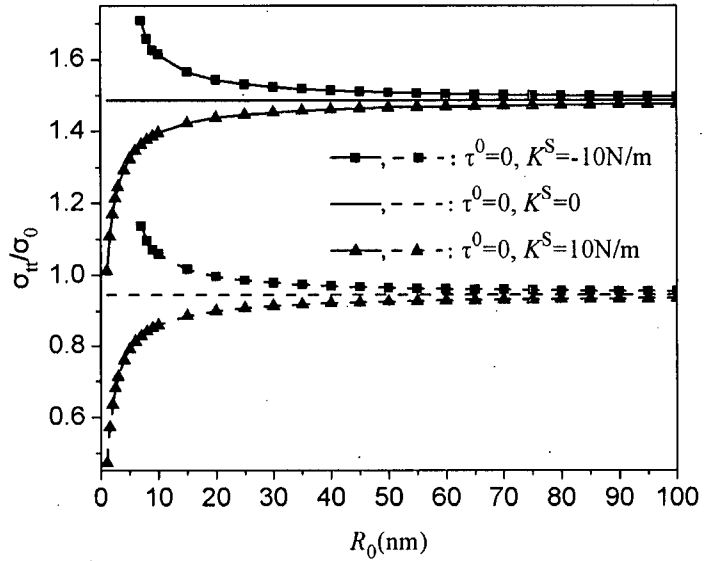
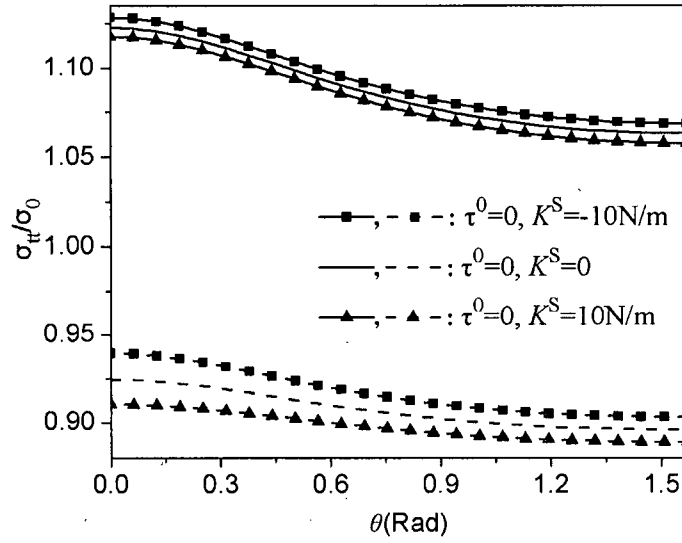
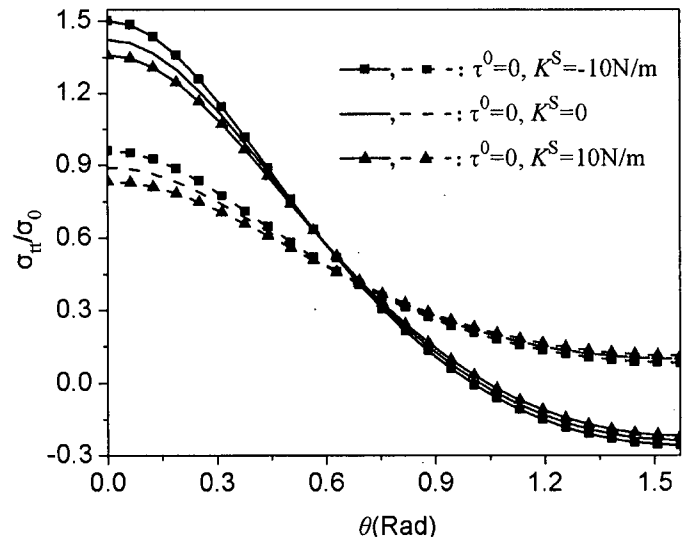


Fig. 3.10. Variation of the nondimensional tangential stress at $\theta = 0$ with the inhomogeneity size R and K^S ($a/b=3$) under uniaxial loading ($\sigma_{yy}^\infty = \sigma_0$): solid lines for matrix and dash lines for inhomogeneity.

Fig. 3.11 shows the nondimensional tangential stress along the inhomogeneity-matrix interface when $R=5\text{nm}$ and $a/b=1.5$. Under biaxial loading, the nondimensional stresses in both matrix and inhomogeneity are increased or decreased when $K^S < 0$ or $K^S > 0$. Under uniaxial loading, however, the nondimensional stresses in both matrix and inhomogeneity are decreased at $\theta = 0$ and increased at $\theta = \pi/2$ when $K^S > 0$; however, opposite behavior is observed for $K^S < 0$. The behavior of the tangential stress under pure shear loading is similar to the case of uniaxial loading. Therefore, the surface effect is the same as the cases of an elliptical hole and of a circular inhomogeneity. The results of displacements, which are not shown here, is also very similar to the case of an elliptical hole.



(a) Under biaxial loading $\sigma_{xx}^{\infty} = \sigma_{yy}^{\infty} = \sigma_0$



(b) Under uniaxial loading $\sigma_{yy}^{\infty} = \sigma_0$

Fig. 3.11. Variation of nondimensional tangential stress along the interface with $R=5\text{nm}$ and $a/b=1.5$: solid lines for matrix and dash lines for inhomogeneity.

The influence of eigenstrain, ε^* , in the inhomogeneity is now considered in the absence of far-field loading. Fig. 3.12 shows the nondimensional tangential stress $\sigma_{tt}/\mu_1\varepsilon^*$ on the interface between the inhomogeneity and the matrix for various values of R when $a/b=1.5$. The results are similar to Fig. 3.9. The size-dependent

behaviour of the stress field is evident for an inhomogeneity with R smaller than 15nm. Again, the effect of K^S is slightly more pronounced in the inhomogeneity than in the matrix and stress is unstable for $K^S < 0$ when R is below 3nm.

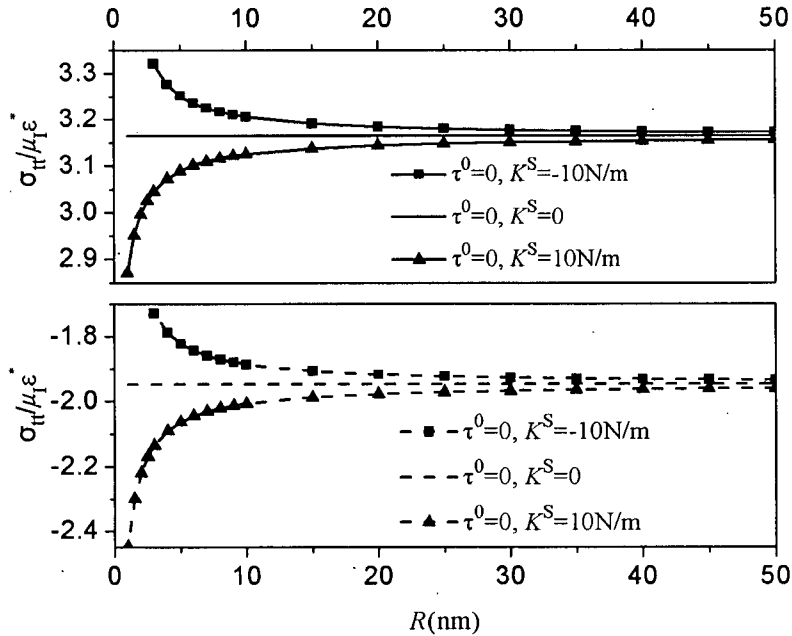


Fig. 3.12. Variation of the nondimensional tangential stress at $\theta = 0$ on the interface with the inhomogeneity size R and K^S ($a/b=1.5$) under a uniform dilatational eigenstrain ϵ^* (solid lines for matrix and dash lines for inhomogeneity).

Now consider Eshelby's problem in the presence of surface/interface effects. Eshelby [34] obtained a uniform elastic field for an ellipsoidal inhomogeneity under a uniform eigenstrain in the classical case. As shown in Fig. 3.13, the nondimensional normal strains in the x_1 -direction and x_2 -direction are no longer uniform and vary along the interface (in the inhomogeneity, $\epsilon = \epsilon^e + \epsilon^*$, where ϵ is the actual strain and ϵ^e is the elastic strain). As the inhomogeneity becomes smaller (e.g., $R=10\text{nm}$), the effect of K^S and the non-uniformity of the elastic field are more prominent. The non-uniformity of strain field is more obvious as a/b increases and more surface stress effects can be observed for ϵ_{22}^e than ϵ_{11}^e . Similar behavior is observed for shear strain. Therefore, the Eshelby's tensor in the current case is size-dependent and non-uniform for an elliptical

inhomogeneity, which is consistent with the result obtained by Sharma and Ganti [32] for an inhomogeneity with non-constant curvature. Similar results are observed for other values of a/b . The effect of τ^0 is not discussed here, but it can be expected that this effect is very similar to the case of an elliptical hole. In addition, the numerical results for plane stress case are very similar to that of plane strain.

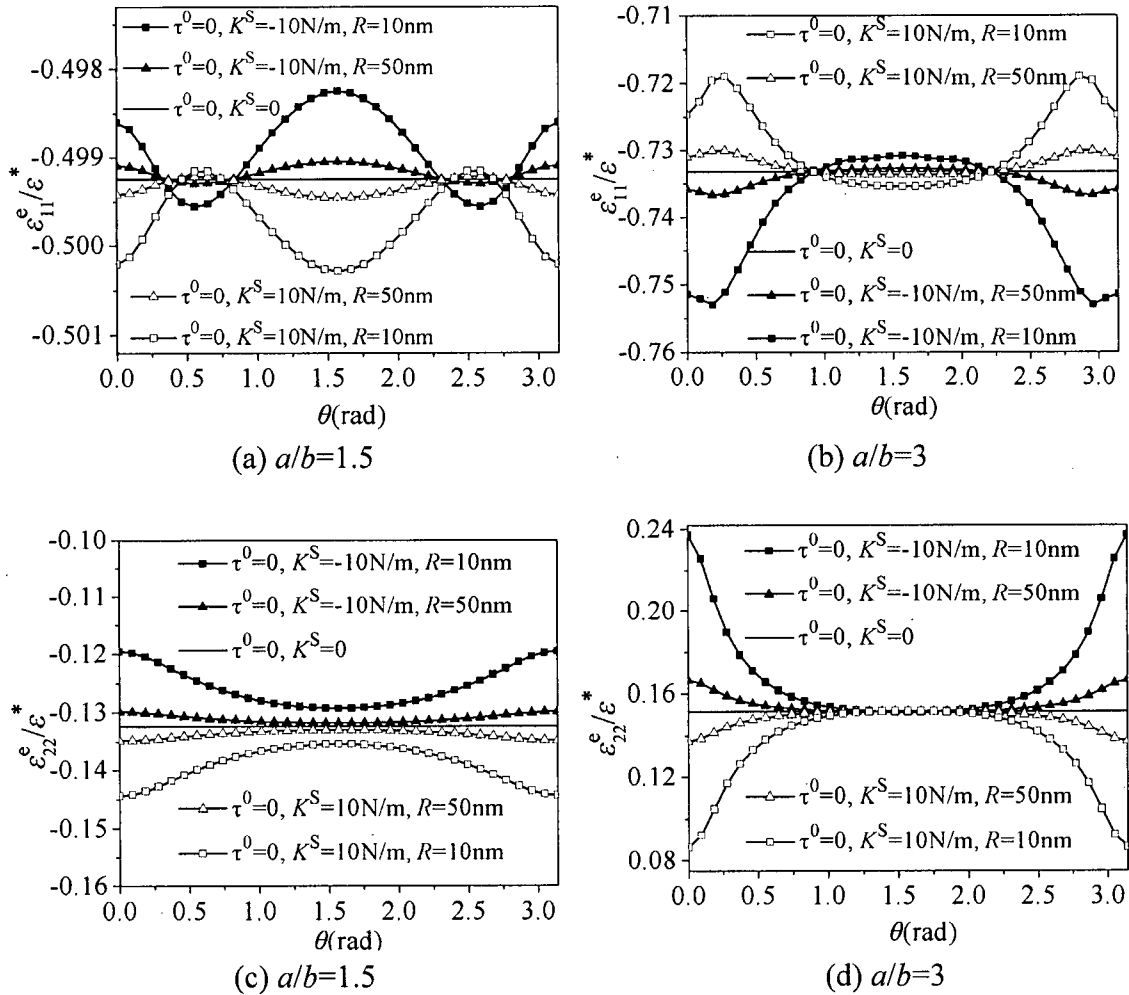


Fig. 3.13. Variation of nondimensional strains along the interface in an inhomogeneity for different values of K^S and R under a uniform dilatational eigenstrain.

Chapter 4

2-D FINITE ELEMENT ANALYSIS OF NANOSCALE INHOMOGENEITY PROBLEMS

4.1 Finite Element Formulation

In this chapter, the classical finite element method (FEM) is extended to develop a new formulation that takes into account the surface stress effects. The finite element scheme is thereafter applied to study the elastic field of a finite plate with a single nanoscale inhomogeneity or two interacting nanoscale inhomogeneities. The advantage of the finite element method when compared to the analytical methods used in Chapters 2 and 3 is that it can be easily applied to solve more complex nanoscale mechanics problems such as arbitrarily shaped inhomogeneities, anisotropic matrix and inhomogeneity materials, and unit cells containing multiple inhomogeneities.

This section presents the detailed derivation of a displacement-based, two-dimensional finite element formulation for a Gurtin-Murdoch type continuum with surface stress effects by using variational methods. The problem under consideration is schematically shown in Fig. 4.1 and a Cartesian coordinate (x, y) [z is the third axis perpendicular to the (x, y) -plane] is used in the analysis. The matrix and inhomogeneities materials have no body forces and are linearly elastic, homogeneous and anisotropic. As the present study is concerned with two-dimensional problems, the surface stress constitutive equations are isotropic. The inhomogeneities are in the nanometer range and can be arbitrarily shaped. Perfect bonding condition is assumed at the inhomogeneity-matrix interface. The matrix-inhomogeneity system is subjected to external loads on the outer surface S of the matrix materials and/or a prescribed eigenstrain in the inhomogeneities.

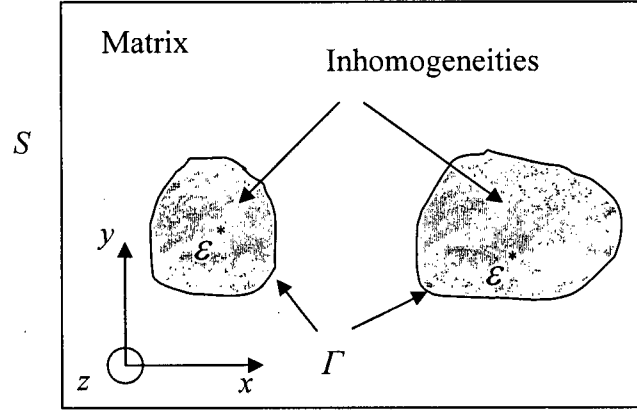


Fig. 4.1 Nanoscale arbitrarily shaped inhomogeneities in a matrix material.

The total potential energy Π of the system under consideration consists of the bulk elastic strain energy U^B of the material system, the potential energy of external loads W and the surface elastic strain energy U^S . Therefore,

$$\Pi = U^B + U^S + W, \quad (4.1)$$

where U^B and W can be calculated from the classical equations as:

$$U^B = \int_{V_M} \int \sigma_{ij}^B d\varepsilon_{ij} dV + \int_{V_I} \int \sigma_{ij}^B d\varepsilon_{ij} dV, \quad (4.2)$$

and

$$W = - \int_S \{u\}^T \{T\} dS, \quad (4.3)$$

Here, the superscript B denotes quantities corresponding to the bulk (both the matrix and inhomogeneities); the superscript T denotes the transpose of a matrix or vector; V_M and V_I denote the volume of the matrix and inhomogeneities respectively; and $\{T\}$ and $\{u\}$ are the surface traction vector due to applied loads and the surface displacement vector respectively.

The surface/interface elastic strain energy U^S associated with the surfaces stresses can be expressed as,

$$U^S = \int_{\Gamma+S} \int \sigma_{\alpha\beta}^S d\varepsilon_{\alpha\beta} d\Gamma, \quad (4.4)$$

where the superscript S denotes quantities corresponding to the surface.

The integral with respect to $d\Gamma$ is taken over the matrix-inhomogeneity interfaces Γ and the boundary surface of the matrix S when the boundary surface elastic strain energy has to be accounted. In the Gurtin-Murdoch surface stress model, it can be assumed that there exists a mathematical surface layer of zero-thickness on which a surface stress tensor exists. Therefore, the integral with respect to the surface/interface in Eq. (4.4) is similar to Eq. (4.3).

Introduce the element shape function matrix $[N(x, y)]$ such that

$$\{u\} = [N]\{\bar{u}\}, \quad (4.5)$$

where $\{u\}$ is the displacement vector at a general point within an element, and $\{\bar{u}\}$ is the nodal displacement vector.

In two-dimensional problems, these two displacement vectors can be written as,

$$\{u\} = \{u_x, u_y\}^T \quad \text{and} \quad \{\bar{u}\} = \{(\bar{u}_x)_1, (\bar{u}_y)_1, (\bar{u}_x)_2, (\bar{u}_y)_2, \dots, (\bar{u}_x)_n, (\bar{u}_y)_n\}^T, \quad (4.6)$$

where the subscript 'n' denotes number of the nodes per element.

Differentiating Eq. (4.5) with respect to the coordinates, the corresponding element strain vector can be expressed as,

$$\{\varepsilon\} = \frac{\partial\{u\}}{\partial x_i} = \left[\frac{\partial[N]}{\partial x_i} \right] \{\bar{u}\} = [B]\{\bar{u}\}, \quad (4.7)$$

where $[B]$ is a matrix containing derivatives of the element shape functions.

For simplicity, the plane shown in Fig. 4.1 is assumed to have unit thickness in the z-direction in the evaluation of all integrals. Integrating Eq. (4.2) with respect to the strains by using linear stress-strain relations for the matrix and inhomogeneity materials results in,

$$U^B = \int_{V_M} \frac{1}{2} \{\varepsilon\}^T [D]_M \{\varepsilon\} dV + \int_{V_I} \frac{1}{2} \{\varepsilon\}^T [D]_I \{\varepsilon\} dV - \int_{V_I} \{\varepsilon\}^T [D]_I \{\varepsilon^*\} dV, \quad (4.8)$$

where $[D]_M$ and $[D]_I$ are the 2-D elasticity matrices of the matrix and inhomogeneity materials respectively, and $\{\varepsilon^*\}$ is the prescribed uniform eigenstrain in the inhomogeneity.

For linear elastic orthotropic material, the elasticity matrix in plane strain case is given by:

$$[D] = \begin{bmatrix} C_{11} & C_{12} & 0 \\ C_{12} & C_{22} & 0 \\ 0 & 0 & C_{66} \end{bmatrix}, \quad (4.9)$$

while in plane stress case,

$$[D] = \begin{bmatrix} C_{11} - \frac{C_{13}^2}{C_{33}} & C_{12} - \frac{C_{13}C_{23}}{C_{33}} & 0 \\ C_{12} - \frac{C_{13}C_{23}}{C_{33}} & C_{22} - \frac{C_{23}^2}{C_{33}} & 0 \\ 0 & 0 & C_{66} \end{bmatrix}, \quad (4.10)$$

where C_{ij} is the 3D elasticity matrix component in the Voigt notation.

Substitution of Eq. (4.7) into Eq. (4.8) yields:

$$U^B = \int_{V_M} \frac{1}{2} \{\bar{u}\}^T [B]^T [D]_M [B] \{\bar{u}\} dV + \int_{V_I} \frac{1}{2} \{\bar{u}\}^T [B]^T [D]_I [B] \{\bar{u}\} dV - \int_{V_I} \{\bar{u}\}^T [B]^T [D]_I \{\epsilon^*\} dV. \quad (4.11)$$

Substitution of Eq. (4.5) into Eq. (4.3) yields:

$$W = - \int_S ([N] \{\bar{u}\})^T \{T\} dS = - \int_S \{\bar{u}\}^T ([N])^T \{T\} dS. \quad (4.12)$$

To obtain the surface elastic strain energy due to surface stress components in the conventional finite element form, the surface stress tensor has to be expressed in the (x, y) coordinate. Fig. 4.2 shows the surface normal-tangential coordinate system (n, t) and the Cartesian coordinates (x, y) . The angle between the normal direction n and the positive x -axis is denoted by θ .

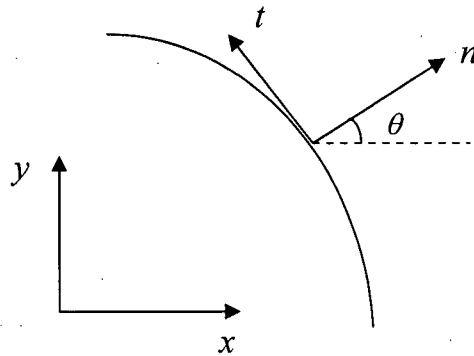


Fig. 4.2 Surface coordinates (n, t) and Cartesian coordinates (x, y) .

Note that in two-dimensional problems only the surface normal stress component in the t -direction, σ_{tt}^S , enters into the calculation of the energy and the surface stresses in the (x, y) coordinates can be expressed in terms of σ_{tt}^S as,

$$\{\sigma_{xx}^S \ \sigma_{yy}^S \ \sigma_{xy}^S\}^T = \{p^2 \ q^2 \ -pq\}^T \sigma_{tt}^S, \quad (4.13)$$

where $p = \sin \theta$, $q = \cos \theta$.

For an isotropic surface, the surface stress constitutive relation can be expressed as [26]:

$$\sigma_{\alpha\beta}^S = \tau^0 \delta_{\alpha\beta} + 2(\mu^S - \tau^0) \varepsilon_{\alpha\beta} + (\lambda^S + \tau^0) \varepsilon_{\gamma\gamma} \delta_{\alpha\beta}. \quad (4.14)$$

and the various quantities in Eq. (4.14) are defined in Chapter 2.

Using Eq. (4.14),

$$\sigma_{tt}^S = \tau^0 + K^S \varepsilon_{tt} + (\lambda^S + \tau^0) \varepsilon_{zz}, \quad (4.15)$$

where $K^S = 2\mu^S + \lambda^S - \tau^0$, and $\varepsilon_{zz} = 0$ for plane strain and $\varepsilon_{zz} = -(C_{13}\varepsilon_{xx} + C_{23}\varepsilon_{yy})/C_{33}$ for plane stress.

Standard tensor transformation rules yield,

$$\varepsilon_{tt} = p^2 \varepsilon_{xx} + q^2 \varepsilon_{yy} - 2pq \varepsilon_{xy} = \{p^2 \ q^2 \ -pq\} \{\varepsilon_{xx} \ \varepsilon_{yy} \ \varepsilon_{xy}\}^T, \quad (4.16)$$

Substituting Eq. (4.15) into Eq. (4.13) and expressing all the strains in the (x, y) coordinates yields

$$\{\sigma_{xx}^S \ \sigma_{yy}^S \ \sigma_{xy}^S\}^T = [D]_S \{\varepsilon_{xx} \ \varepsilon_{yy} \ \varepsilon_{xy}\}^T, \quad (4.17)$$

where

$$[D]_S = \begin{bmatrix} K^S p^4 + V_1^S p^2 & K^S p^2 q^2 + V_2^S p^2 & -K^S p^3 q \\ K^S p^2 q^2 + V_1^S q^2 & K^S q^4 + V_2^S q^2 & -K^S pq^3 \\ -K^S p^3 q - V_1^S pq & -K^S pq^3 - V_2^S pq & K^S p^2 q^2 \end{bmatrix}. \quad (4.18)$$

Here, $V_1^S = V_2^S = 0$ for plane strain which results in a symmetric matrix $[D]_S$, and $V_1^S = -(\lambda^S + \tau^0)C_{13}/C_{33}$ and $V_2^S = -(\lambda^S + \tau^0)C_{23}/C_{33}$ for plane stress which results in an unsymmetric matrix $[D]_S$.

By using Eq. (4.17) and Eq. (4.7), Eq. (4.4) can be expressed as:

$$\begin{aligned}
U^S &= \int_{\Gamma+S} \frac{1}{2} \{\boldsymbol{\varepsilon}\}^T [D]_s \{\boldsymbol{\varepsilon}\} d\Gamma + \int_{\Gamma+S} \{\boldsymbol{\varepsilon}\}^T \{p^2 q^2 - pq\}^T \tau^0 d\Gamma \\
&= \int_{\Gamma+S} \frac{1}{2} \{\bar{\boldsymbol{u}}\}^T [B]^T [D]_s [B] \{\bar{\boldsymbol{u}}\} d\Gamma + \int_{\Gamma+S} \{\bar{\boldsymbol{u}}\}^T [B]^T \{p^2 q^2 - pq\}^T \tau^0 d\Gamma. \quad (4.19)
\end{aligned}$$

Now invoke the stationary condition of Π , i.e., $\delta\Pi = 0$, with respect to the unknown nodal displacement vector. In view of Eq. (4.1), the variations of the three terms in Π can be expressed as,

$$\begin{aligned}
\delta U^B &= \{\delta\bar{\boldsymbol{u}}\}^T \left(\int_{V_M} [B]^T [D]_M [B] dV \right) \{\bar{\boldsymbol{u}}\} + \{\delta\bar{\boldsymbol{u}}\}^T \left(\int_{V_1} [B]^T [D]_I [B] dV \right) \{\bar{\boldsymbol{u}}\} \\
&\quad - \{\delta\bar{\boldsymbol{u}}\}^T \left(\int_{V_1} [B]^T [D]_I \{\boldsymbol{\varepsilon}^*\} dV \right), \quad (4.20)
\end{aligned}$$

$$\delta W = -\{\delta\bar{\boldsymbol{u}}\}^T \left(\int_S [N]^T \{T\} dV \right), \quad (4.21)$$

$$\delta U^S = \{\delta\bar{\boldsymbol{u}}\}^T \left(\int_{\Gamma+S} [B]^T [\bar{D}]_s [B] d\Gamma \right) \{\bar{\boldsymbol{u}}\} + \{\delta\bar{\boldsymbol{u}}\}^T \left(\int_{\Gamma+S} [B]^T \{p^2 q^2 - pq\}^T \tau^0 d\Gamma \right), \quad (4.22)$$

where $[\bar{D}]_s = \frac{1}{2} ([D]_s + [D]_s^T)$ and is a symmetric matrix.

Finally, the equilibrium equation can be expressed as,

$$[K] \{\bar{\boldsymbol{u}}\} = \{f\}, \quad (4.23)$$

where

$$[K] = \int_{V_M} [B]^T [D]_M [B] dV + \int_{V_1} [B]^T [D]_I [B] dV + \int_{\Gamma+S} [B]^T [\bar{D}]_s [B] d\Gamma, \quad (4.24)$$

is the total stiffness matrix obtained by assembling the element stiffness matrices, and

$$\{f\} = \int_S [N]^T \{T\} dV + \int_{V_1} [B]^T [D]_I \{\boldsymbol{\varepsilon}^*\} dV - \int_{\Gamma+S} [B]^T \{p^2 q^2 - pq\}^T \tau^0 d\Gamma, \quad (4.25)$$

is the total equivalent nodal load vector obtained by assembling element load vectors.

From Eqs. (4.23)-(4.25), it can be seen that presence of surface stresses changes the stiffness matrices and nodal load vectors of the elements that have a side on the surface/interface on which surface stresses exist. Moreover, the presence of a non-zero residual surface stress τ^0 produces an additional term for the nodal force vector. Residual

surface stress also has an effect on the stiffness of an element as the matrix $[D]_s$ is a function of τ^0 . In the absence of surface stress effects, the above equations reduce to the classical elasticity case. In the following numerical study, the effect of τ^0 is not presented and $K^s = \pm 10 \text{ N/m}$, and the plane strain case is considered without loss of any generality.

4.2 Finite Element Simulation of Inhomogeneity Problems

A computer code based on the finite element formulation presented in the preceding section was developed. The commercial software package Hypermesh is used to generate a two-dimensional finite element mesh and 8-node isoparametric elements are used to discretize the domain. The mesh information is then read by a FORTRAN based finite element program developed by the author. All area and line integrals are computed by using 3×3 and 3 Gauss integration schemes respectively. The linear equation system is solved by an IMSL subroutine. Stresses in an element are first calculated at the 2×2 Gauss integration points by using basic relations in elasticity and then extrapolated to the node points by using a bilinear extrapolation. The final nodal stress is the average of the stresses of the node calculated from different elements associated with the node.

4.2.1 Elastic Field Around a Hole in a Finite Plate

A finite plate of isotropic aluminum containing a nanoscale elliptical hole is subjected to uniform remote traction in the y -direction as shown in Fig. 4.3. The properties of aluminum are given in Chapter 2. The hole with a major axis length equal to $2a$ and minor axis length equal to $2b$ is located at the middle of the plate. The origin of the Cartesian coordinate system (x, y) is at the center of the hole and the normal-tangential coordinate system (n, t) at a point on the surface of the hole is as shown in Fig. 4.3. First consider the special case of a circular hole ($a=b=R$). Surface stresses are present around the surface of the hole and do not exist along the outer boundary of the plate.

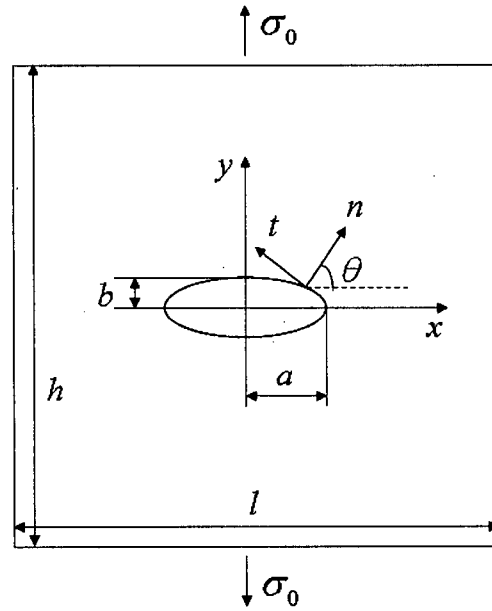


Fig. 4.3. A nanoscale elliptical hole in a finite plate.

Figure 4.4 shows the variation of nondimensional hoop stress with the hole radius for $2R/l=0.05$ and $2R/h=0.05$. This case approximates the behaviour of a circular hole in an infinite plane and the corresponding analytical solution is also shown in Fig. 4.4. The agreement between the two solutions is very good and confirms the high accuracy of the present finite element solutions. An interesting observation from Fig. 4.4 is the unstable behaviour of the solution below some hole radius when $K^S < 0$. Similar behaviour was noted earlier in the case of the analytical solution of an elliptical hole. It is noted that stiffness matrix of the finite element mesh becomes non-positive definite below a certain R value when $K^S < 0$. The reason is that, for $K^S < 0$, the surface elastic energy is negative and it could dominate over the bulk elastic energy for small values of R . As found in Chapter 3 using the analytical solution, hoop stress can also be singular in the case of an infinite plane with a circular hole but for R less than 1nm. However, in the case of finite element analysis, the plane has finite dimensions and this causes the unstable behaviour of the solution to occur at a R value greater than 1nm. Such unstable behaviour does not happen for $K^S > 0$ in which case hoop stress becomes smaller as R decreases. For $K^S > 0$, the total stiffness matrix remain positive definite for all values of R .

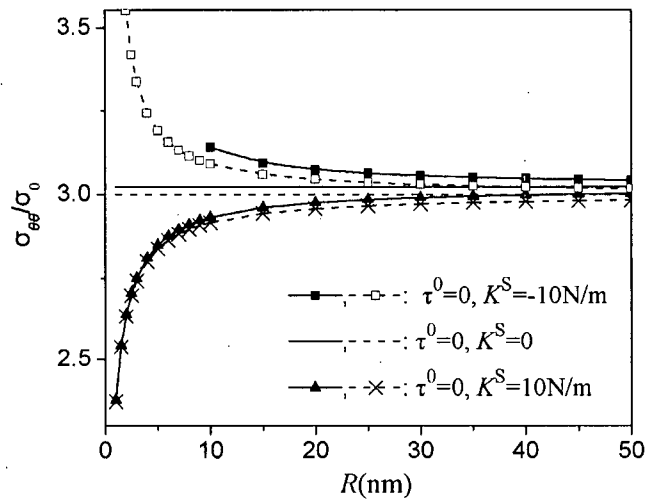


Fig. 4.4 Comparison of analytical and finite element hoop stress solutions (dash lines for analytical solution of infinite plate and solid lines for finite plate with $2R/l=0.05$ and $2R/h=0.05$).

Consider next the case of a circular hole in a finite plate. The distance between the center of the hole and the top and bottom edges is kept at ten times the radius of the hole, i.e., $2R/h=0.1$, and hoop stress at $\theta = 0$ is shown in Fig. 4.5 for two values of the length ratio ($2R/l=0.1$ and 0.4). The results are similar to the case of an infinite plane with a circular hole [Fig. 2.2(b) in Chapter 2] and Fig. 4.4, but the stresses are due to the plate boundary effects. As in the case of Fig. 4.4, hoop stress becomes highly oscillatory and singular at some radii when $K^S < 0$. The radius below which this unstable behaviour occurs increases as the plate becomes smaller.

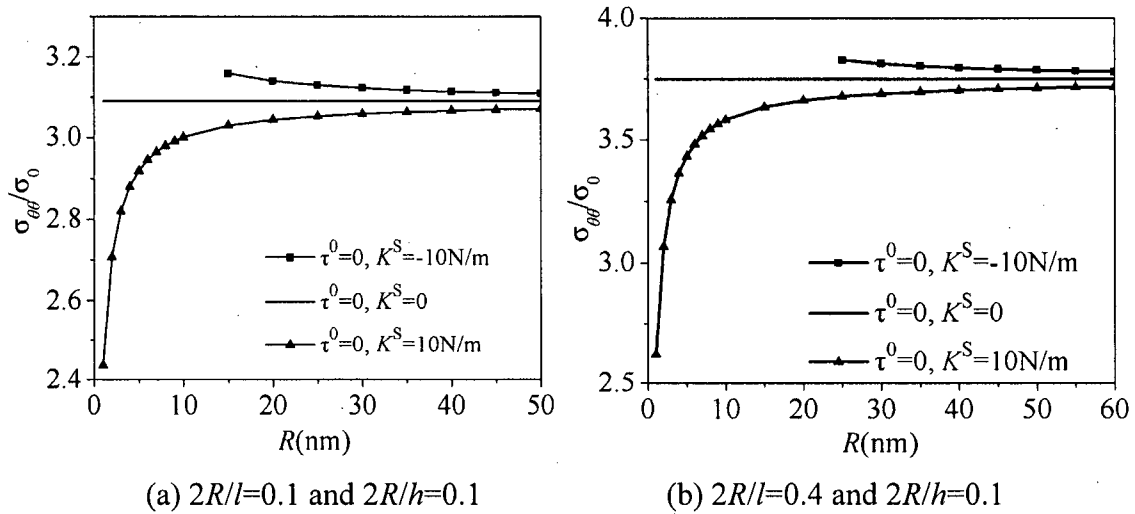


Fig. 4.5. Variation of nondimensional hoop stress at $\theta = 0$ of a finite plate with R .

Fig. 4.6 shows the variation of nondimensional hoop stress on hole surface with angle θ . The solution behaviour is very similar to the infinite plane solution in Chapter 2. The maximum value of hoop stress increases as the plate dimensions get smaller. Note that although the R values corresponding to $K^S = 10$ and $K^S = -10$ are different, hoop stress solutions for the two cases are quite close to each other. Fig. 4.7 shows the nondimensional hoop stress at $\theta = 0$ for various values of $2R/l$. In this figure, $R=30\text{nm}$ for $K^S < 0$ as the stress is unstable for R less than 30nm when $2R/l=0.5$. As $2R/l$ increases, hoop stress corresponding to the classical and current cases increase nonlinearly.

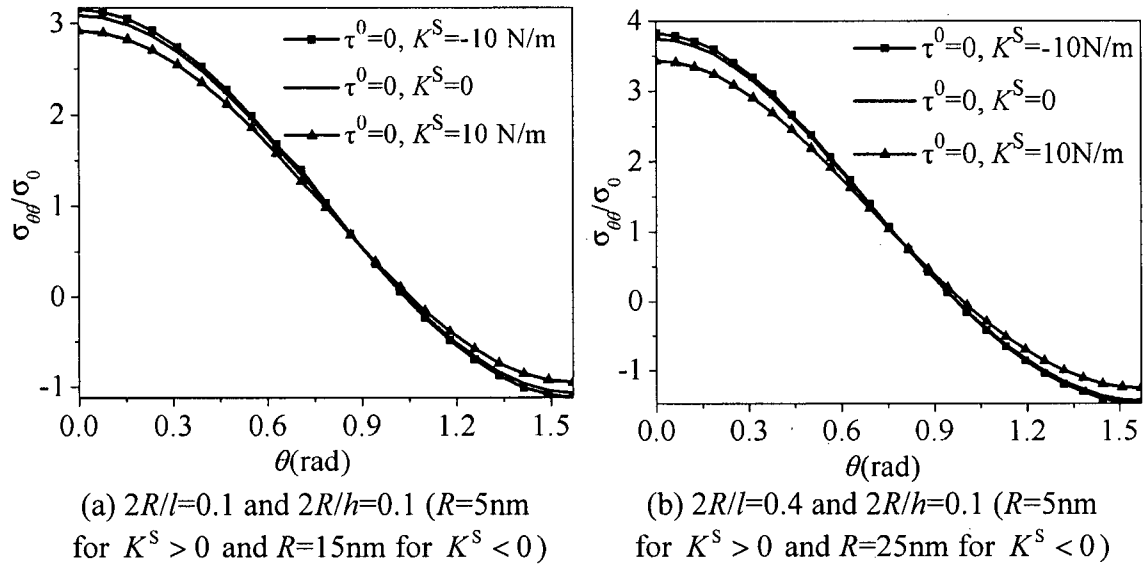


Fig. 4.6. Variation of nondimensional hoop stress at hole surface with θ .

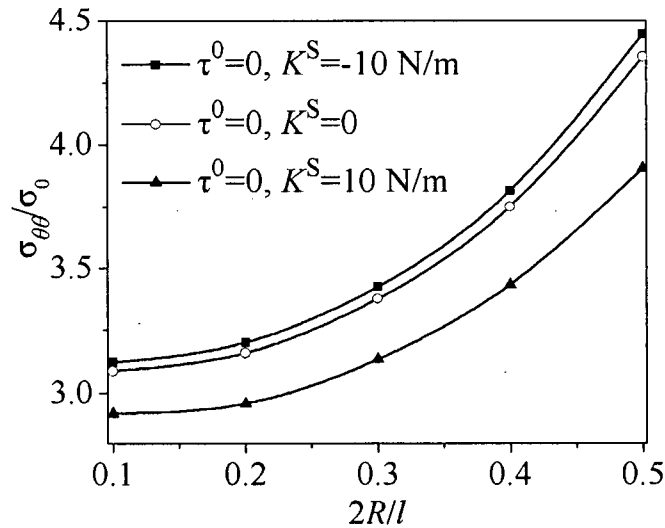


Fig. 4.7 Variation of nondimensional hoop stress at $\theta = 0$ with $2R/l$ ($2R/h=0.1$; $R=5\text{nm}$ for $K^S > 0$ and $R=30\text{nm}$ for $K^S < 0$).

Consider now the case of an elliptical hole with $a/b=1.5$ (Fig. 4.3). Fig. 4.8 shows the variation of the nondimensional tangential stress on the hole surface with R [$=(a+b)/2$] and θ for $2b/h=0.1$ and $2a/l=0.1$ and 0.4 . The results are similar to the case of an infinite plane containing an elliptic hole with $a/b=1.5$ [Figs. 3.3 and 3.5(b) in Chapter 3].

As in the case of analytical solution, hoop stress becomes unstable for R less than 14nm and 24nm for $2a/l = 0.1$ and 0.4 respectively. Note that stress instability starts when R is less than 6nm for an infinite plane with an identical elliptical hole (Chapter 3). Fig. 4.9 shows the nondimensional hoop stress at $\theta = 0$ for various values of $2a/l$ and the behavior is similar to the case of a circular hole.

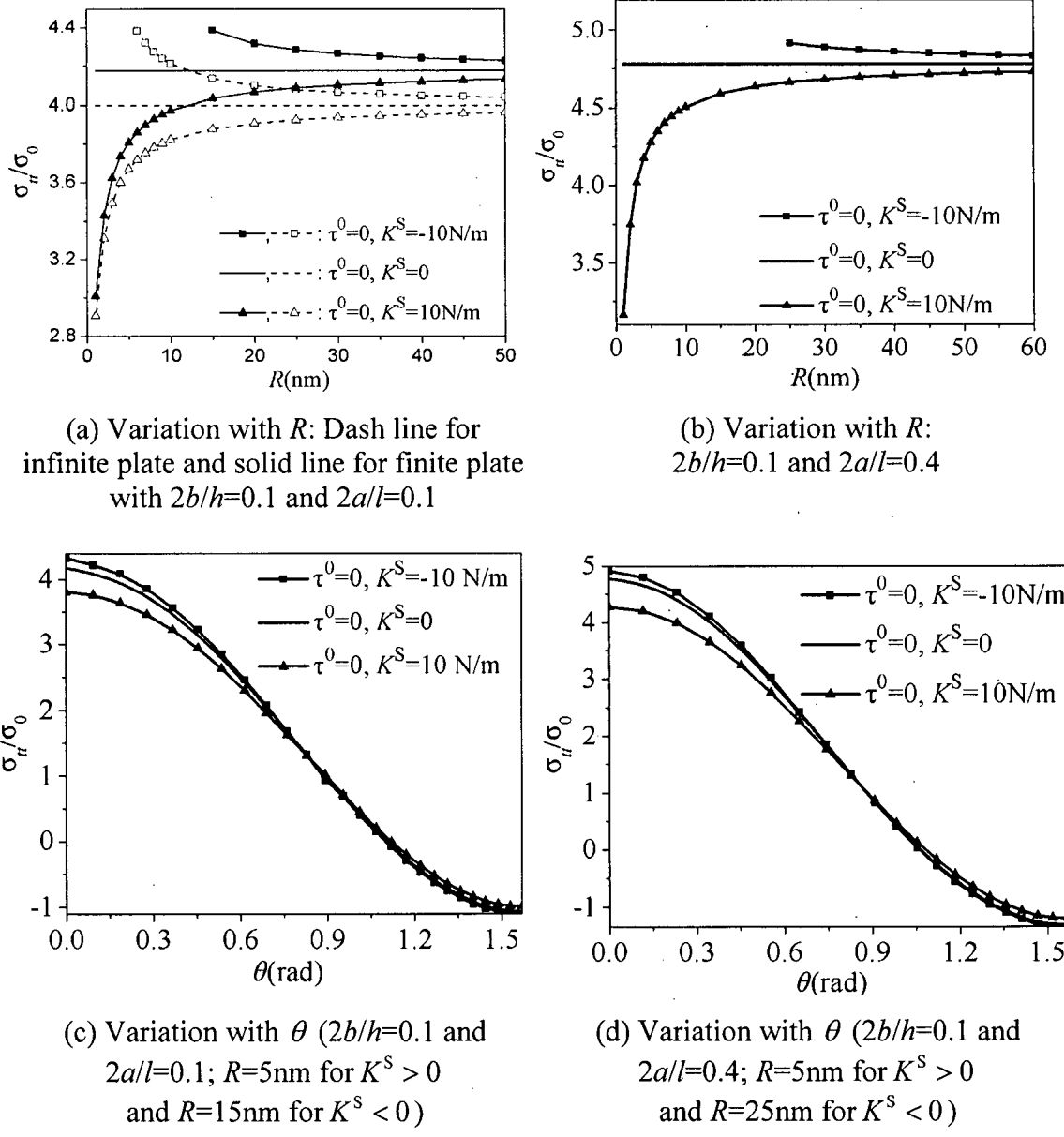


Fig. 4.8 Variation of nondimensional tangential stress of an elliptical hole with R and θ ($a/b=1.5$).

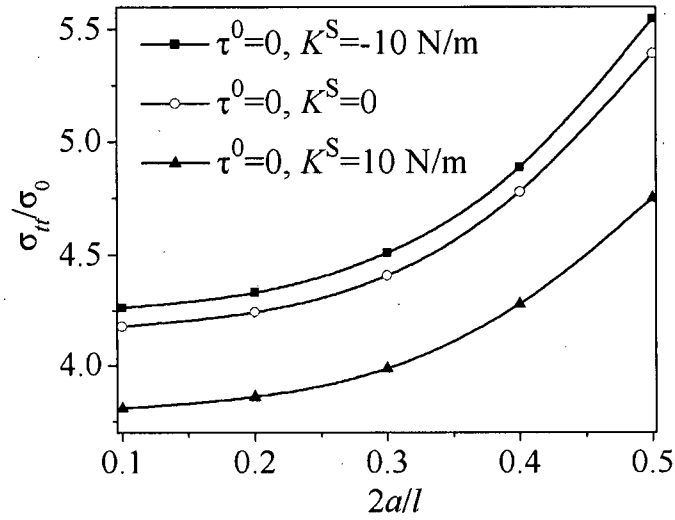


Fig. 4.9 Variation of nondimensional hoop stress at $\theta = 0$ with $2a/l$ ($2b/h=0.1$; $R=5\text{nm}$ for $K^S > 0$ and $R=30\text{nm}$ for $K^S < 0$).

A remotely loaded semi-infinite plate of isotropic aluminum with a circular hole as shown in Fig. 4.10 is considered. The objective is to consider the interaction between the hole and free surface. In the finite element analysis, the distances between the center of the hole and the left, right and bottom edges are set to ten times the radius of the hole, i.e., $h/R=10$ and $l/2R=10$ to simulate the case of a semi-infinite medium. The influence of free surface is controlled by the distance between the center of the hole and top surface which is denoted by D . The origins of the Cartesian coordinate system (x, y) and polar coordinate system (r, θ) are located at the center of the hole.

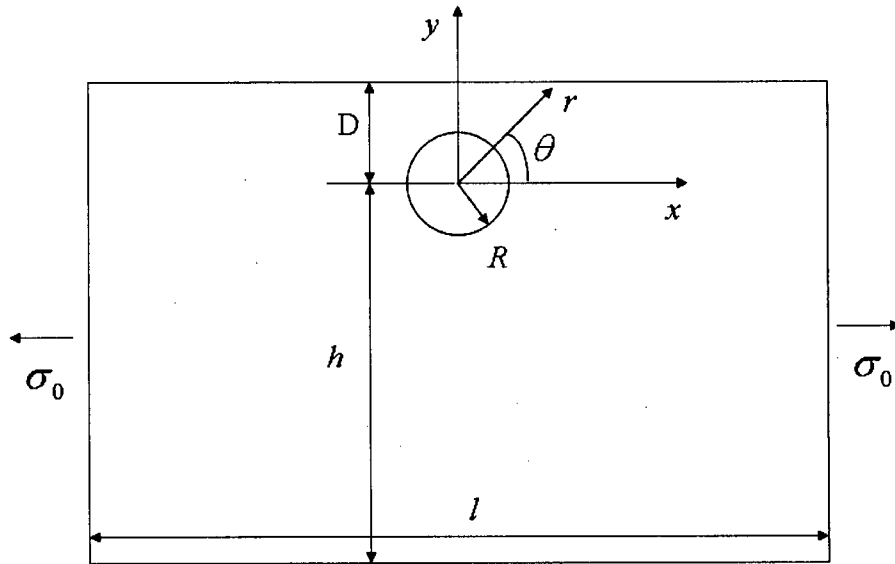
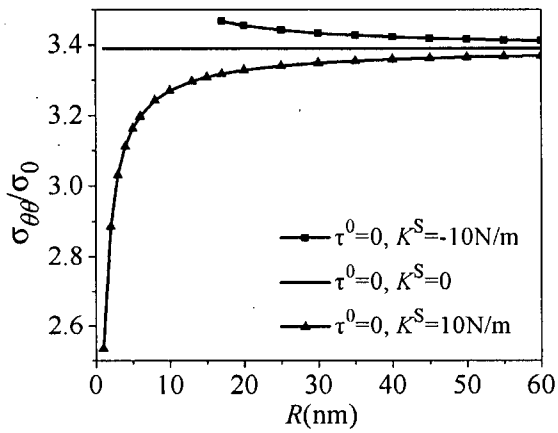
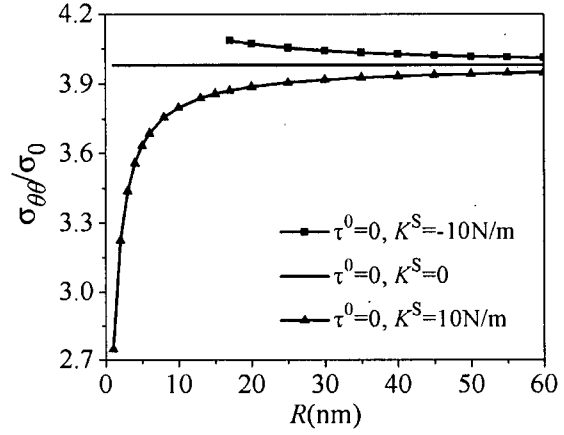


Fig. 4.10 A nanoscale circular hole in a semi-infinite plate.

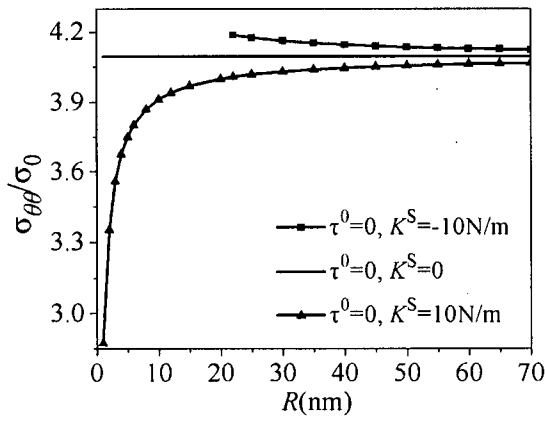
Fig. 4.11 shows the variation of nondimensional hoop stress at $\theta = \pi/2$ $\theta = -\pi/2$ with hole radius R for $D/R=2$ and 1.1 . The stress field is unstable for R less than 17nm and 22nm for $D/R=2$ and 1.1 respectively when K^s is negative. As expected hoop stress at $\theta = -\pi/2$ is smaller than that at $\theta = \pi/2$. A substantial increase in hoop stress is noted at $\theta = \pi/2$ when $D/R=1.1$. Fig. 4.12 shows the variation of nondimensional hoop stress along the hole surface. Hoop stress is not symmetric with respect to $\theta = 0$ in the present case and the dependence on θ becomes quite complex when $D/R=1.1$. The surface stress effect is much more pronounced on the portion of the hole surface that is closer to the free surface when $D/R=1.1$.



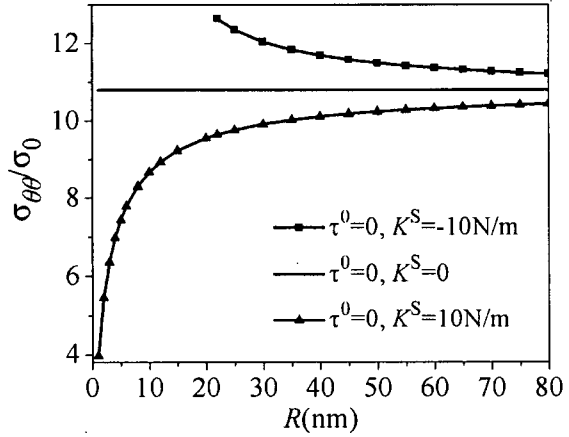
(a) $D/R=2$ ($\theta = -\pi/2$)



(b) $D/R=2$ ($\theta = \pi/2$)

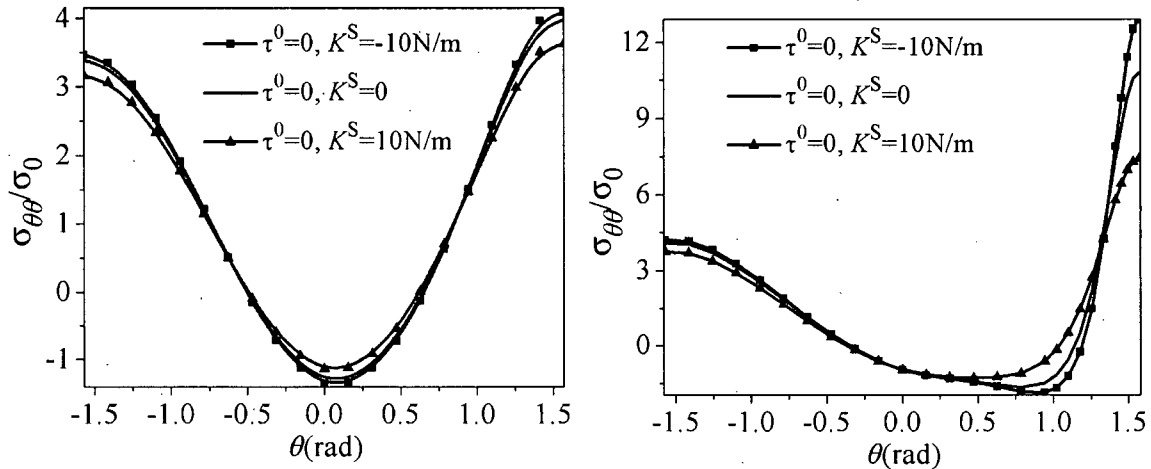


(c) $D/R=1.1$ ($\theta = -\pi/2$)



(d) $D/R=1.1$ ($\theta = \pi/2$)

Fig. 4.11 Variation of nondimensional hoop stress at $\theta = \pm \pi/2$ with hole radius for two different D/R values ($D/R=2$ and 1.1).



(a) $D/R=2$; $R=5\text{nm}$ for $K^S > 0$ and $R=17\text{nm}$ for $K^S < 0$

(b) $D/R=1.1$; $R=5\text{nm}$ for $K^S > 0$ and $R=22\text{nm}$ for $K^S < 0$

Fig. 4.12 Variation of nondimensional hoop stress on hole surface with angle θ ($D/R=2$ and 1.1).

Fig. 4.13 shows the variation of nondimensional hoop stress at $\theta = \pi/2$ and $\theta = -\pi/2$ with D/R . As D/R decreases, hoop stress increases rapidly at both points but the influence at $\theta = \pi/2$ is higher. The surface stress effect is more pronounced for positive K^S values at $\theta = \pi/2$. When $K^S = 10\text{N/m}$ and $R = 5\text{nm}$, the increases of nondimensional hoop stress due to surface stress effect are 6.7% for $D/R=2$ and 8.4% for $D/R=1.1$ at $\theta = -\pi/2$, and the changes are 8.7% for $D/R=2$ and 31.2% for $D/R=1.1$ at $\theta = \pi/2$.

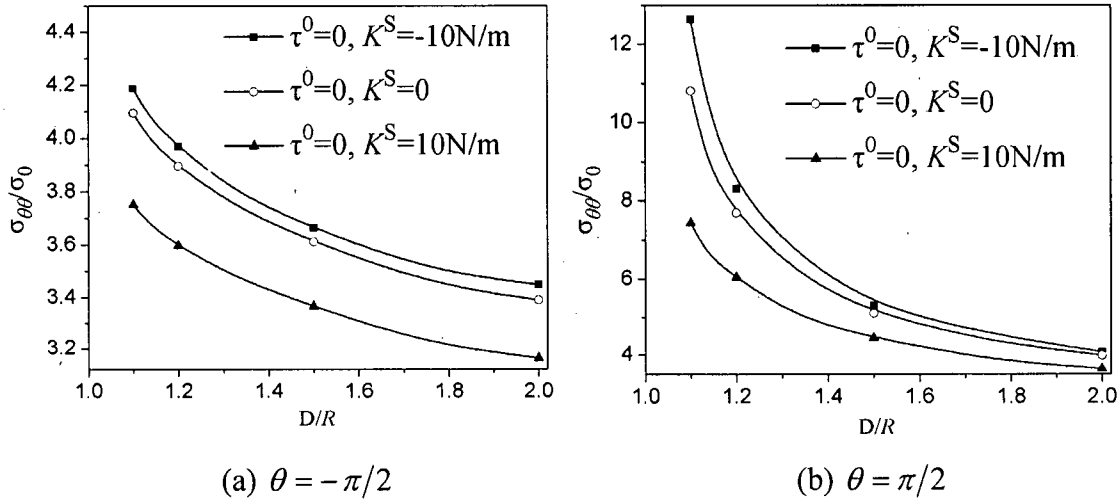


Fig. 4.13 Variation of nondimensional hoop stress with D/R ($R=5\text{nm}$ for $K^S > 0$ and $R=22\text{nm}$ for $K^S < 0$).

4.2.2 Elastic Field of a Finite Plate with Two Circular Inhomogeneities

This section considers a finite plate of GaAs, containing two circular InAs inhomogeneities with identical radii as shown in Fig. 4.14. Both the matrix and inhomogeneities materials are assumed to be isotropic and their properties are given in Chapter 2. The plate is subjected to uniform remote tension in the vertical direction. The two inhomogeneities are at a distance $2D$ between their centers, and are located symmetrically in the plate. Let $l/R=10$ and $h/R=20$, so that the effect of the plate edges on the elastic field in and around the inhomogeneities is very small when compared to the interaction between the two inhomogeneities if the distance between them is small. Only one quarter of the problem has to be considered in the finite element analysis and the Cartesian coordinate system (x, y) and polar coordinate system (r, θ) are defined as shown in Fig. 4.14.

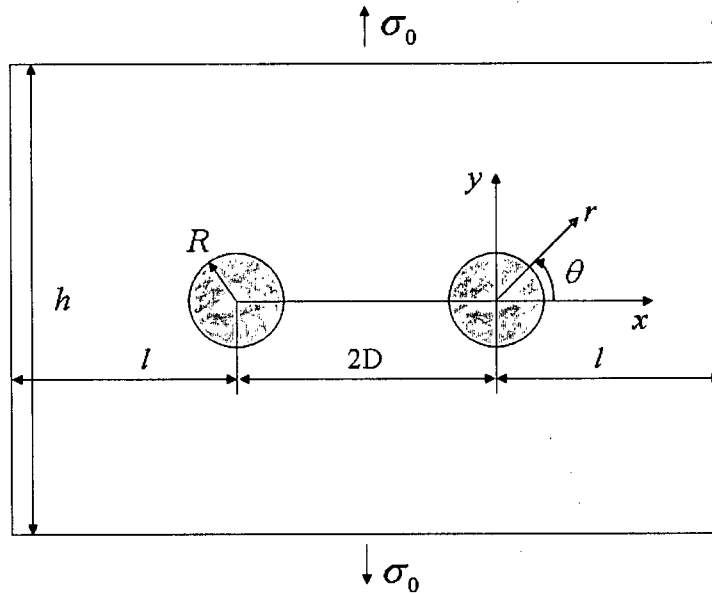


Fig. 4.14 Two circular inhomogeneities in a finite plate.

Fig. 4.15 and 4.16 shows the variation of nondimensional hoop stress in the matrix and inhomogeneity at two locations ($\theta = 0$ and $\theta = \pi$) on their interface for different values of radius R and angle θ when $D/R = 1.1$ and 2.0 respectively. As D/R decreases, the interaction is more significant. This can be seen by comparing Fig. 4.15 and Fig. 4.16. The general variation of hoop stress is similar to the case of a single inclusion presented in Chapter 2. Hoop stresses in both the matrix and inhomogeneity are smaller at $\theta = 0$ when compared to $\theta = \pi$ and so is the surface stress effect. The stress is unstable for R less than 7nm for $K^S = -10\text{N/m}$.

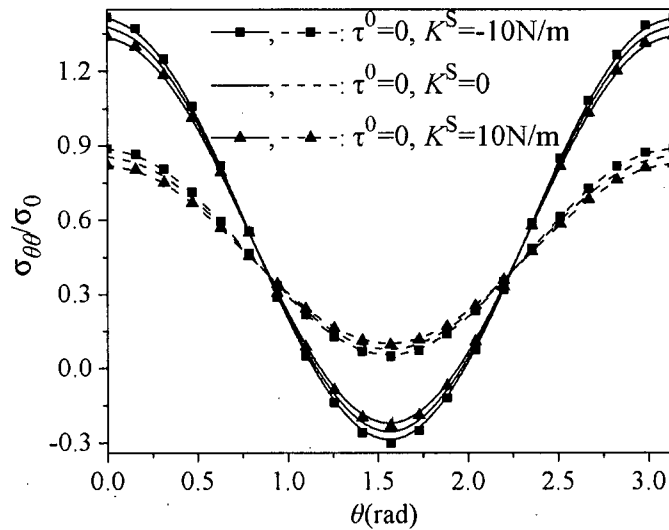
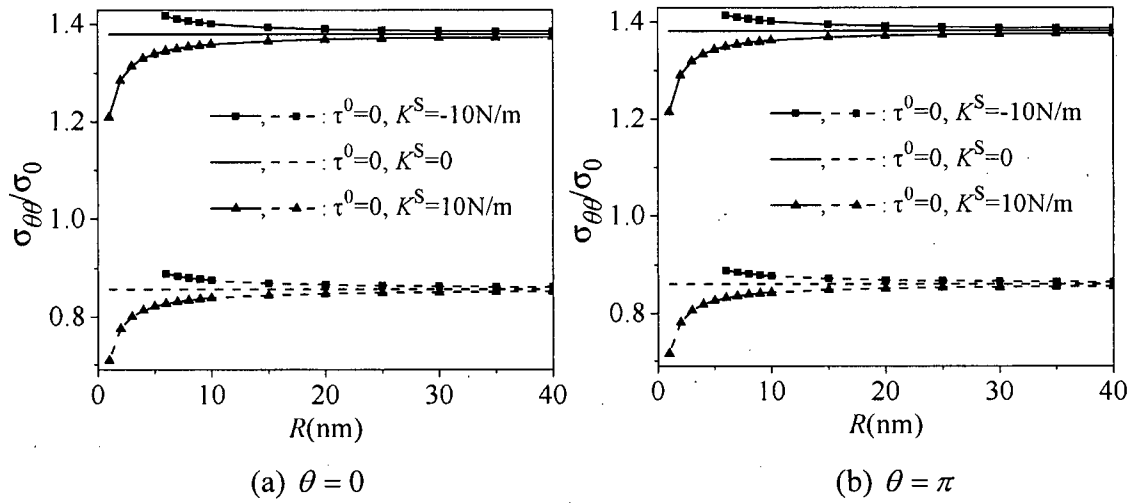


Fig. 4.15 Variation of nondimensional interfacial hoop stress with radius and angle ($D/R=2$; Solid lines for matrix and dash lines for inhomogeneity).

diminishes rapidly with increasing D/R and the interaction between the inhomogeneities vanishes when $D/R > 2$ but substantial influence can be seen at $\theta = \pi$ when D/R less than 1.5. The surface stress effect is a little more pronounced at $\theta = \pi$ than at $\theta = 0$.

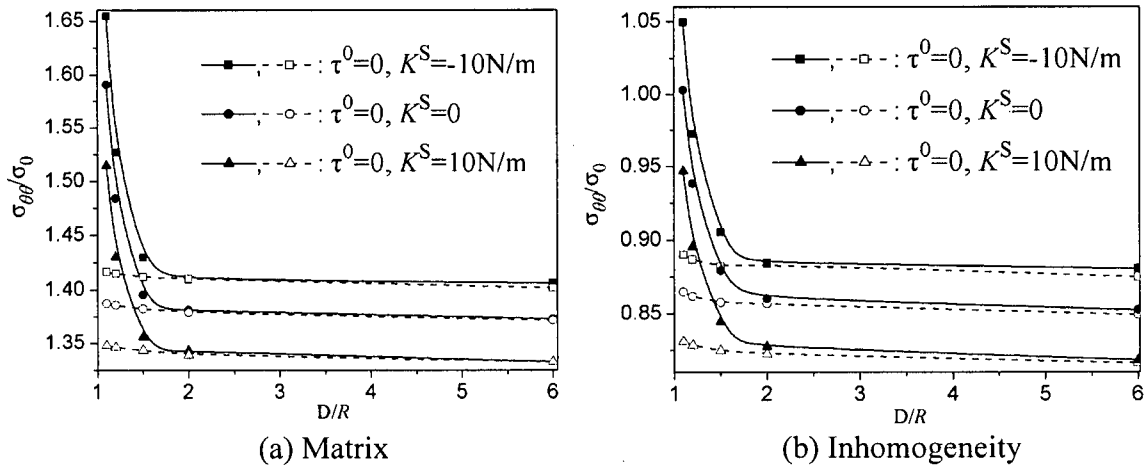


Fig. 4.17 Variation of nondimensional hoop stress with D/R ($R=5\text{nm}$ for $K^S > 0$ and $R=7\text{nm}$ for $K^S < 0$; Solid lines for $\theta = \pi$ and dash lines for $\theta = 0$).

4.2.3 Elastic Field Around a Circular Hole in a Finite Anisotropic Plate

Consider a circular hole ($a=b=R$) embedded in the middle of a finite plate under uniform remote loading in the y -direction (Fig. 4.3). The plate under consideration is FCC Al which has cubic symmetry. The coordinate directions are assumed to be the crystallographic directions and the three independent elastic constants are: $C_{11} = 118.10\text{GPa}$, $C_{12} = 62.293\text{GPa}$ and $C_{66} = 36.706\text{GPa}$ [24]. The surface properties are assumed to be isotropic. Therefore, the new FEM formulation developed in section 4.1 is also applicable in the case of plane strain state. Figs. 4.18 and 4.19 shows the variation of nondimensional hoop stress with the hole radius and angle respectively for $2R/l=0.05$ and $2R/h=0.05$. The classical nondimensional hoop stress at $\theta = 0$ is a little far from 3 due to the anisotropic properties of Aluminum. The surface stress effects are similar to that in the isotropic case (Figs. 4.4 and 4.6). The hoop stress is also found to become unstable for the radius less than 10nm when the surface elastic modulus, K^S , is

negative. Fig. 4.20 shows the variation of nondimensional normal displacement along the hole surface for both isotropic and anisotropic cases when $2R/l=0.05$ and $2R/h=0.05$. In both cases, the nondimensional displacements are increased or decreased when $K^S < 0$ or $K^S > 0$.

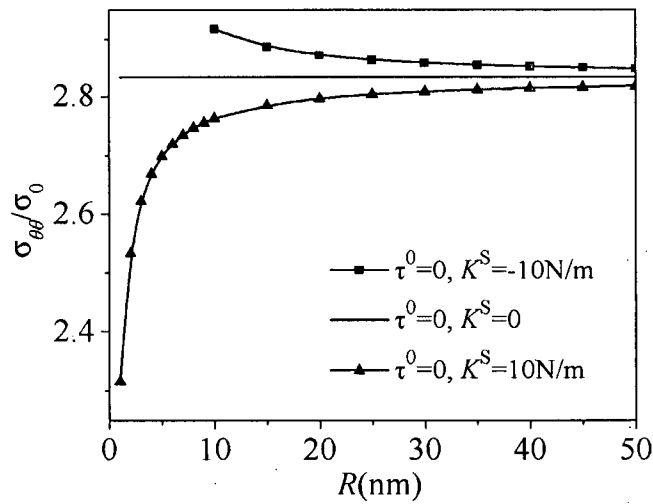


Fig. 4.18 Variation of nondimensional hoop stress on hole surface at $\theta = 0$ with R ($2R/l=0.05$ and $2R/h=0.05$).

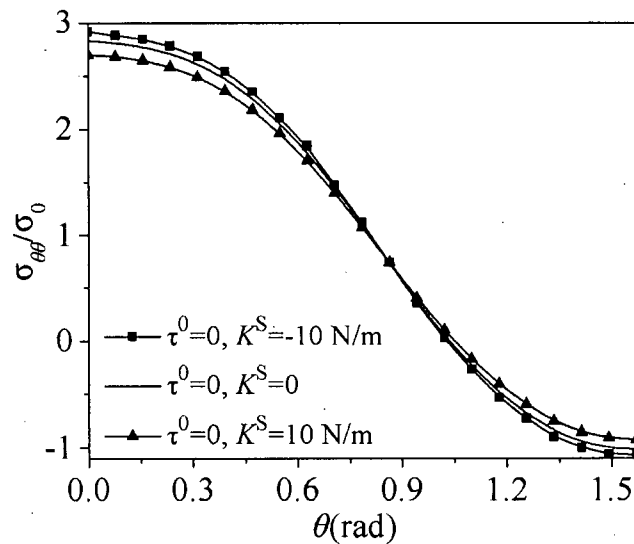


Fig. 4.19 Variation of nondimensional hoop stress along hole surface with θ ($2R/l=0.05$ and $2R/h=0.05$).

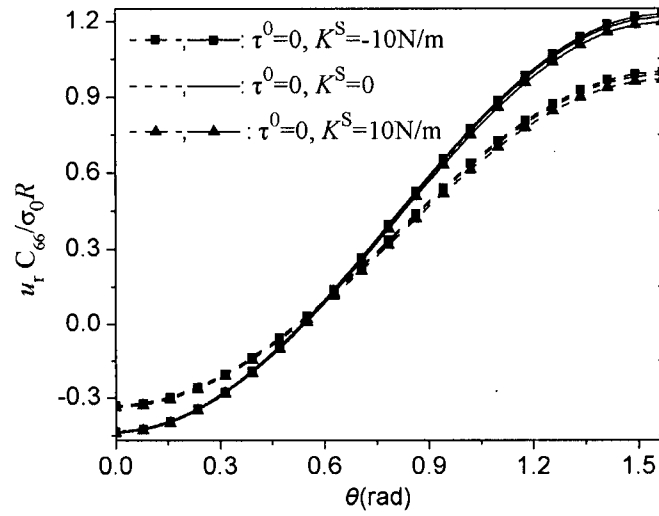


Fig. 4.20 Variation of nondimensional normal displacement with θ ($2R/l=0.05$ and $2R/h=0.05$; Solid lines for anisotropic case and dash lines for isotropic case).

Chapter 5

SUMMARY AND CONCLUSIONS

5.1 Summary and Major Findings

The major findings and conclusions of the current study are given below.

(1) Based on the Gurtin-Murdoch surface/interface elasticity model, a closed-form analytical solution is obtained for the elastic field of an infinite isotropic elastic matrix containing a nanoscale circular inhomogeneity under arbitrary remote loading or a uniform eigenstrain in the inhomogeneity. The extension of the complex potential function method of Muskhelishvili is demonstrated for the first time for nanoscale inhomogeneity problems. The new solution reduces to the classical elasticity solution in the absence of surface stress effects. The stress state shows strong dependency on inhomogeneity radius, surface elastic constants and residual surface stress when the inhomogeneity radius is less than 10nm. Hoop stress around matrix-inhomogeneity interface can be increased or decreased due to surface stress effects and can be singular for an inhomogeneity with radius less than 1nm when the surface stress modulus, K^S , is negative. The Eshelby tensor for a uniform eigenstrain is uniform but becomes size-dependent for a nanoscale circular inhomogeneity. The effect of surface stresses becomes negligible at a distance greater than three to four times the radius of the inhomogeneity. The circular nanoscale inhomogeneity solution presented in this thesis is a benchmark solution in nanomechanics and can be used in the validation of numerical methods such as the finite element method and in the study of effective properties of nanocomposites with dilute concentrations of reinforcing particles.

(2) Following the successful derivation of the closed-form analytical solution for a circular inhomogeneity, the complex potential function method is extended to consider the case of a nanoscale elliptical inhomogeneity. The elliptical inhomogeneity problem is fundamentally important to the manufacture of nanocomposites and quantum dots as it allows some basic understanding of the optimum shape of inhomogeneities for enhanced properties and load transfer. The analytic potential functions, which are expressed by

infinite power series, can only be obtained approximately for an elliptical inhomogeneity. The elastic field is therefore investigated through a comprehensive numerical study. As in the case of a circular inhomogeneity, the elastic state is size-dependent, and hoop stress around a hole or an inhomogeneity interface is decreased or increased depending on whether K^S is positive or negative. An interesting feature of the elliptical inhomogeneity solution is the instability of the elastic field below a certain value of the sum of the half-lengths of the major and minor axes of the inhomogeneity for negative K^S values. Such unstable phenomenon does not occur when K^S is positive. The reason for this behaviour is the non-positive definite nature of the elastic energy associated with the surface stresses when K^S is negative and its dominance over the bulk strain energy for very small dimensions of the inhomogeneity. In such situations, the Gurtin-Murdoch model essentially breaks down and atomistic or other models need to be chosen. The Eshelby tensor for a uniform eigenstrain is size-dependent and no longer uniform in the case of an elliptical inhomogeneity.

(3) The classical finite element method (FEM) is extended in this thesis to develop a new formulation for the analysis of two-dimensional problems involving an elastic matrix with arbitrary shaped nanoscale inhomogeneities. The formulation is based on the Gurtin-Murdoch continuum model and the principle of minimum total potential energy. The influence of the surface stresses appears in the formulation through a term corresponding to surface elastic strain energy due to surface stresses. It is found that the stiffness matrix associated with the surface stresses can be positive definite or non-positive definite depending on the values of the surface elastic constants. This can lead to a total stiffness matrix that is non-positive definite and the resulting elastic field shows unstable and singular behaviour. Unstable behaviour of the elastic field is noted in the finite element analysis for all negative values of K^S when the characteristic dimension of the inhomogeneity is below a certain value. As the dimensions of the matrix domain are increased, the finite element solutions become very close to the analytical solution for an infinite matrix. This confirms the high accuracy of the present finite element scheme.

(4) The stress field of a finite plate with a nanoscale circular or elliptical hole under remote tension is studied by using the FEM. As the ratio of the width of the plate to the hole radius decreases, the surface stress effects become more pronounced, and the hole size below which the elastic field becomes unstable for negative K^S also increases. Surface stress effects are more significant in the case of an elliptical hole in a finite plate and further increase as the ellipse becomes flatter. The stress field of a semi-infinite plate with a circular hole near the free edge is obtained by using the FEM. When the distance between the centre of the hole and the free edge is greater than three times the radius of the hole, the edge effect is quite small. As the hole approaches the edge, the edge effect and the surface stress effects result in a significant increase of hoop stress. The stress field of a finite plate with two identical circular inhomogeneities is also studied by using the FEM. The general trend of the solution is similar to that of a single circular inhomogeneity. As the distance between the two inhomogeneities decreases, their interaction becomes more significant and the surface stress effect becomes more pronounced. Unstable behaviour of the elastic field is also noted in this case when the inhomogeneity radius is below a certain value and K^S is negative. The elastic field of a circular hole in an anisotropic matrix is shown and the result is found to be similar to that of the isotropic case.

5.2 Suggestions for Future Work

Current understanding of mechanics of nanomaterials is very limited. The study of nanoscale inhomogeneity problems has important implications in the development of nanomaterials with superior properties. The present study has examined some basic problems related to nanoscale inhomogeneities and further studies are necessary to advance the development of nanomaterials and the scientific base for nanotechnology. It is therefore recommended that following studies be undertaken to advance the current state-of-the-art of mechanics of nanomaterials.

(1) Isotropic behavior of matrix, inhomogeneity and surface/interface is assumed in the analytical solutions derived in this thesis. However, anisotropic behaviour is more practically useful in nanotechnology applications. Benchmark analytical solutions for a

circular (2-D) and spherical (3-D) inhomogeneity in an anisotropic matrix will be useful to gain some fundamental understanding of the behaviour of nanocomposites and other nanomaterials. The extension and numerical implementation of the new FEM formulation developed in the current study to include a range of anisotropic material models for both bulk and surface responses and multiple inhomogeneities of different shapes will be useful to the study of nanomaterials and calculation of effective properties of nanocomposites.

(2) Inhomogeneities are assumed to be perfectly bonded to the matrix in the present study. It is useful to examine the cases of slip, twist and wrinkling of the inhomogeneity surface/interface to gain some fundamental understanding of the failure modes of nanocomposites and other nanomaterials. In addition, the matrix and inhomogeneity materials are assumed to be perfectly elastic in the present study but plastic deformations can play a significant role at the nanoscale. Consideration of plasticity effects may be useful in examining the instability of elastic field that is observed for negative values of K^s when the inhomogeneity characteristic dimensions are below a certain value. Such unusual behaviour may not be present in the case of an elasto-plastic model.

(3) This thesis establishes the necessary framework to conduct a finite element study of a unit cell of a nanocomposite material. A comprehensive study of a unit cell taking into account different inhomogeneity shapes and sizes, anisotropic behaviour of the matrix/inhomogeneities, interface effects, inhomogeneity densities and distributions, etc. will be very useful to the study of effective properties of nanocomposites.

(4) Experimental studies and atomistic simulations are recommended to validate the applicability of the Gurtin-Murdoch model and the analytical and FEM solutions obtained in the thesis.

BIBLIOGRAPHY

- [1] Feynman, R.P., "There is plenty of room at the bottom", In: Gilbert, H.D. (Eds), *Miniaturization*, Reinhold, New York, 1961.
- [2] Smalley, R. E., "Congressional hearings", Summer 1999.
- [3] "Nanotechnology – a revolution in the making -- vision for R&D in the next decade", A report of the interagency working group on the nanoscience, engineering, and technology, presented to the OSTP committee on technology, March 10, 1999.
- [4] Klabunde, K.J., "Introduction to nanotechnology", In: Klabunde, K.J., (Eds), *Nanoscale Materials in Chemistry*, John Wiley & Sons, New York, 2001.
- [5] Dai, H., Hafner, J.H., Rinzler, A.G., Colbert, D.T. and Smalley, R.E., "Nanotubes as nanoprobe in scanning probe microscopy", *Nature*, Vol. 384 (14), pp. 147-150, 1996.
- [6] Kassner, M.E. et al, "New directions in mechanics", *Mech. Mater.*, Vol. 37(2-3), pp. 231-259, 2005.
- [7] Kouris, D. and Gao, H., "Nanomechanics of surfaces and interfaces", *ASME J. Appl. Mech.*, Vol. 69(4), pp. 405-406, 2002.
- [8] Maranganti, R. and Sharma, P., "A review of strain field calculations in embedded quantum dots and wires", In: Reith, M. and Schommers, W., (Eds.), *Handbook of Theoretical and Computational Nanotechnology*, American Scientific Publishers, Stevenson Ranch, California (Chapter 118), 2006.
- [9] Ji, B. and Gao, H., "A study of fracture mechanisms in biological nanocomposites via the virtual internal bond model", *Mater. Sci. Eng. A*, Vol. 366(1), 96-103, 2004.
- [10] Streit, F.H., Cammarata, R.C. and Sieradzki, K., "Surface-stress effects on elastic properties. I. Thin metal films", *Phys. Rev. B*, Vol. 49(15), pp. 10699–10706, 1994.
- [11] Dingreville, R., Qu, J. and Cherkaoui, M., "Surface free energy and its effect on the elastic behavior of nano-sized particles, wires and films", *J. Mech. Phys. Solids*, Vol. 53(8), pp. 1827-1954, 2005.
- [12] Yakobson, B.I., "Nanomechanics", In: William, A. et al. (Eds), *Handbook of Nanoscience, Engineering and Technology* (Chapter 17), CRC Press, Boca Raton, 2003.

- [13] Wong, E.W., Sheehan, P.E. and Lieber, C.M., "Nanobeam mechanics: elasticity, strength, and toughness of nanorods and nanotubes", *Science*, Vol. 277(5334), pp. 1971-1975, 1997.
- [14] Cuenot, S., Frétiigny, C., Demoustier-Champagne S. and Nysten, B., "Surface tension effect on the mechanical properties of nanomaterials measured by atomic force microscopy", *Phys. Rev. B*, Vol. 69(16), pp. 165410-1–165410-5, 2004.
- [15] Singh, R.P., Zhang, M. and Chan, D., "Toughening of a brittle thermosetting polymer: effects of reinforcement particle size and volume fraction", *J. Mater. Sci.*, Vol. 37(4), pp. 781-788, 2002.
- [16] Cadek, M. et al., "Reinforcement of polymers with carbon nanotubes: the role of nanotube surface area", *Nano Lett.*, Vol. 4(2), pp. 353-356, 2004.
- [17] Sun, C.T. and Zhang, H., "Size-dependent elastic moduli of platelike nanomaterials", *J. Appl. Phys.*, Vol. 93(2), pp. 1212-1218, 2002.
- [18] Liang, H., Upmanyu, M. and Huang, H., "Size-dependent elasticity of nanowires: nonlinear effects", *Phys. Rev. B*, Vol. 71(24), pp. 241403-1–241403-4, 2005.
- [19] Rubin, M.B. and Benveniste, Y., "A cosserat shell model for interphases in elastic media", *J. Mech. Phys. Solids*, Vol. 52(5), pp. 1023-1052, 2004.
- [20] Gibbs, J.W., *The Scientific Papers of J. Willard Gibbs*. Vol. 1. Longmans Green, London, 1906.
- [21] Cammarata, R.C., "Surface and interface stress effects in thin films", *Prog. Surf. Sci.*, Vol. 46(1), 1–38, 1994.
- [22] Shuttleworth, R., "The surface tension of solids", *Proc. Phys. Soc. A*, Vol. 63, pp. 444-457, 1950.
- [23] Nix, W.D. and Gao, H., "An atomistic interpretation of interface stress", *Scr. Mater.*, Vol. 39(12), pp. 1653–1661, 1998.
- [24] Miller, R.E. and Shenoy, V.B., "Size-dependent elastic properties of nanosized structural elements". *Nanotechnology*, Vol. 11(3), pp. 139-147, 2000.
- [25] Shenoy, V.B., "Atomistic calculations of elastic properties of metallic fcc crystal surfaces", *Phys. Rev. B*, Vol. 71(9), pp. 094104-1–094104-11, 2005.
- [26] Gurtin, M.E. and Murdoch, A.I., "A continuum theory of elastic material surfaces", *Arch. Rat. Mech. Anal.*, Vol. 57(4), pp. 291-323, 1975.

- [27] Gurtin, M.E., Weissmuller, J. and Larché, F., "A general theory of curved deformable interfaces in solids at equilibrium", *Philos. Mag. A*, Vol. 78(5), pp. 1093-1109, 1998.
- [28] Gurtin, M.E. and Murdoch, A.I., "Surface stress in solids", *Int. J. Solids Struct.*, Vol. 14(6), pp. 431-440, 1978.
- [29] Weissmüller, J. and Cahn, J.W., "Mean Stresses in microstructures due to interface stresses: A generalization of a capillary equation for solids", *Acta Mater.*, Vol. 45(5), pp. 1899-1906, 1997.
- [30] Ibach, H., "The role of surface stress in reconstruction, epitaxial growth and stabilization of mesoscopic structures", *Surf. Sci. Rep.*, Vol. 29(5-6), pp. 195-263, 1997.
- [31] Sharma, P., Ganti, S. and Bhate, N., "Effect of surfaces on the size-dependent elastic state of nano-inhomogeneities", *Appl. Phys. Lett.*, Vol. 82(4), pp. 535-537, 2003.
- [32] Sharma, P. and Ganti, S., "Size-dependent Eshelby's tensor for embedded nano-inclusions incorporating surface/interface energies", *ASME J. Appl. Mech.*, Vol. 71(5), pp. 663-671, 2004.
- [33] Duan, H.L., Wang, J., Huang, Z.P. and Karihaloo, B.L., "Size-dependent effective elastic constants of solids containing nano-inhomogeneities with interface stress", *J. Mech. Phys. Solids*, Vol. 53(7), pp. 1574-1596, 2005.
- [34] Eshelby, J.D., "The determination of the elastic field of an ellipsoidal inclusion and related problems", *Proc. R. Soc. London, Ser. A*, Vol. 241, 376-396, 1957.
- [35] Eshelby, J.D., "The elastic field outside an ellipsoidal inclusion", *Proc. R. Soc. London, Ser. A*, Vol. 252, pp. 561-569, 1959.
- [36] Eshelby, J.D., "Elastic inclusions and inhomogeneities", In: Sneddon, I.N. and Hill, R. (Eds), *Progress in Solid Mechanics 2*, North Holland, Amsterdam, pp. 89-140, 1961.
- [37] Mura, T., *Micromechanics of Defects in Solids*, Martinus Nijhoff, Dordrecht, Netherlands, 1987.
- [38] Nemat-Nasser, S. and Hori, M., *Micromechanics: Overall Properties of Heterogeneous Solids*, Elsevier, New York, 1999.
- [39] Markov, K. and Preziosi, L., *Heterogeneous Media: Micromechanics Modeling Methods and Simulations*, Birkhauser Verlag, Switzerland, 2000.

- [40] Yang, F., "Size-dependent effective modulus of elastic composite materials: spherical nanocavities at dilute concentrations", *J. Appl. Phys.*, Vol. 95 (7), pp. 3516-3520, 2004.
- [41] Duan, H.L., Wang, J., Huang, Z.P. and Karihaloo, B.L., "Eshelby formalism for nano-inhomogeneities", *Proc.R. Soc. A*, Vol. 461(2062), pp. 3335-3353, 2005.
- [42] Gao, W., Yu, S.W. and Huang, G.Y., "Finite element characterization of the size-dependent mechanical behavior in nanosystems", *Nanotechnology*, Vol. 17(4), pp. 1118-1122, 2006.
- [43] Muskhelishvili, N.I., *Some Basic Problems of the Mathematical Theory of Elasticity*. P. Noordhoff Ltd., Groningen, The Netherlands, 1963.
- [44] Ruud, J.A., Witvrouw, A. and Spaepen, F., "Bulk and interface stresses in silver-nickel multilayered thin films", *J. Appl. Phys.*, Vol. 74(4), pp. 2517-2523, 1993.
- [45] Josell, D., Bonevitch, J.E., Shao, I. and Cammarata, R.C., "Measuring the interface stress: Silver/nickel interfaces", *J. Mater. Res.*, Vol. 14(11), pp. 4358-4365, 1999.
- [46] Meyers, M.A. and Chawla, K.K., *Mechanical Behavior of Materials*. Prentice Hall, Englewood Cliffs, NJ, pp. 92, 1999.
- [47] Zhou, L.G. and Huang, H., "Are surfaces elastically softer or stiffer?", *Appl. Phys. Lett.*, Vol. 84(11), pp. 1940-1942, 2004.
- [48] Li, Z.R., Lim, C.W. and He, L.H., "Stress concentration around a nano-scale spherical cavity in elastic media: effect of surface stress", *Eur. J. Mech. A/Solids*, Vol. 25(2), pp. 260-270, 2006.
- [49] Sharma, P. and Ganti, S., "Interfacial elasticity corrections to size-dependent strain-state of embedded quantum dots", *Phys. Stat. Sol. B*, Vol. 234(3), pp. R10-R12, 2002.
- [50] England, A.H., *Complex Variable Methods in Elasticity*. Wiley-Interscience, London, 1971.
- [51] Stagni, L., "Elastic field perturbation by an elliptic inhomogeneity with a sliding interface", *J. Appl. Math. Phys. (ZAMP)*, Vol. 42(6), pp. 811-820, 1991.
- [52] Shen, H., Schiavone, P., Ru, C.Q. and Mioduchowski, A., "Interfacial thermal stress analysis of an elliptic inclusion with a compliant interphase layer in plane elasticity", *Int. J. Solids Struct.*, Vol. 38(42-43), pp. 7587-7606, 2001.

- [53] Shen, H., Schiavone, P., Ru, C.Q. and Mioduchowski, A., "An elliptic inclusion with imperfect interface in anti-plane shear", *Int. J. Solids Struct.*, Vol. 37(33), pp. 4557-4575, 2000.

APPENDICES

Appendix A

Using the expression for the curvature $\frac{1}{R_0} = \frac{(1-m^2)/R}{|m'(\xi)/R|^3}$ (see Appendix B) and

Eq. (3.9), the interface stress in the matrix can be expressed as:

$$\begin{aligned} \left(\frac{\frac{1}{2}\sigma_{ii}^S}{R_0}\right)_M m'(\xi) \overline{m'(\xi)}/R &= \frac{(1-m^2)}{|m'(\xi)/R|^3} \left[\frac{\frac{1}{2}\tau^0 m'(\xi) \overline{m'(\xi)}}{R^2} + \Lambda_1 \left(\frac{\Theta_M(\xi)\xi^2}{R} + \frac{\overline{\Theta_M(\xi)\xi^2}}{R} \right) \right. \\ &\quad \left. + (\Lambda_1 + \Lambda_4)\Lambda_2 \left(\frac{\phi_M'(\xi)m'(\xi)}{R} + \frac{\overline{\phi_M'(\xi)m'(\xi)}}{R} \right) \right], \quad \text{on } \Gamma, \quad (\text{A.1}) \end{aligned}$$

where

$$\Lambda_1 = \frac{K^S}{8\mu_M R}, \quad K^S = 2\mu^S + \lambda^S - \tau^0, \quad \Lambda_2 = \frac{2\mu_M}{Q_M}, \quad \Lambda_4 = \frac{\lambda^S + \tau^0}{4\mu_M R} \frac{\nu_M}{\nu_M - 1}. \quad (\text{A.2})$$

By using Eqs. (3.9), (3.35) and (3.36), the derivative term in Eq. (3.38) is written as:

$$\begin{aligned} &i \frac{\frac{1}{2}\partial(\sigma_{ii})_M}{\partial t} m'(\xi) \overline{m'(\xi)}/R \\ &= \frac{1}{|m'(\xi)/R|^3} \left\{ -\frac{\Lambda_1 \Theta_M'(\xi)}{R} [-m\xi + (1+m^2)\xi^3 - m\xi^5] - \frac{\Lambda_1 \Theta_M(\xi)}{R} [2(1+m^2)\xi^2 - 4m] \right. \\ &\quad \left. + \frac{\Lambda_1 \overline{\Theta_M'(\xi)}}{R} [-m\xi^{-5} + (1+m^2)\xi^{-3} - m\xi^{-1}] + \frac{\Lambda_1 \overline{\Theta_M(\xi)}}{R} [2(1+m^2)\xi^{-2} - 4m] \right. \\ &\quad \left. - \Lambda_2 (\Lambda_1 + \Lambda_4) \left[\frac{\phi_M''(\xi)m'(\xi)}{R} - \frac{\phi_M'(\xi)m''(\xi)}{R} \right] \frac{(m'(\xi))^2 \xi}{R^2} \right. \\ &\quad \left. + \Lambda_2 (\Lambda_1 + \Lambda_4) \left[\frac{\overline{\phi_M''(\xi)m'(\xi)}}{R} - \frac{\overline{\phi_M'(\xi)m''(\xi)}}{R} \right] \frac{(m'(\xi))^2 \bar{\xi}}{R^2} \right\}, \quad \text{on } \Gamma. \quad (\text{A.3}) \end{aligned}$$

In the inclusion, considering the effect of eigenstrain, the actual strain is regarded as the sum of elastic strain and eigenstrain. However, the calculation is the same as that in the matrix and the result is similar. In Eqs. (A.1)-(A.3), ϕ_M and Θ_M are replaced by ϕ_I

and Θ_1 , respectively; Λ_1 and Λ_2 by Λ_6 and Λ_7 , respectively; Λ_4 by Λ_5 ; τ^0 by $\tau^0 + 8(\Lambda_6 + \Lambda_5)\mu_1 R \varepsilon^*$, and others keep the same. Here,

$$\Lambda_5 = \frac{\lambda^S + \tau^0}{4\mu_1 R} \frac{\nu_1}{\nu_1 - 1}, \quad \Lambda_6 = \frac{K^S}{8\mu_1 R}, \quad \Lambda_7 = \frac{2\mu_1}{Q_1}. \quad (\text{A.4})$$

Multiplying Eq. (3.38) by a factor $\frac{m'(\xi)\overline{m'(\xi)}/R}{m'(\xi)/R}$ and using Eqs. (3.17), (3.18),

(3.24), (3.25), (A.1) and (A.3) yields:

$$\begin{aligned} \frac{m'(\xi)\overline{m'(\xi)}/R}{m'(\xi)/R} \left[\frac{\sigma_u^S}{R_0} + i \frac{\partial \sigma_u^S}{\partial t} \right] &= \frac{1}{m'(\xi)/R} \frac{1}{|m'(\xi)/R|^3} \left[g_0 + h_0 + (g_1 + h_1)e^{-i\theta} + (g_2 + h_2)e^{i\theta} \right. \\ &+ (g_3 + h_3)e^{-2i\theta} + (g_4 + h_4)e^{2i\theta} + (g_5 + h_5)e^{-3i\theta} + (g_6 + h_6)e^{3i\theta} + h_7e^{-4i\theta} + h_8e^{4i\theta} \\ &\left. + \sum_{n=1}^{\infty} S_n e^{i(n+3)\theta} + \sum_{n=1}^{\infty} T_n e^{-i(n+3)\theta} + \sum_{n=1}^{\infty} U_n e^{i(n+4)\theta} + \sum_{n=1}^{\infty} V_n e^{-i(n+4)\theta} \right], \quad \text{on } \Gamma, \quad (\text{A.5}) \end{aligned}$$

where

$$\begin{aligned} g_0 &= \frac{1}{2}\tau^0(1-m^4) + \Lambda_2(\Lambda_1 + \Lambda_4)(2-2m^2)A + 4\Lambda_1 m(D_0 - \overline{D}_0) \\ &+ \Lambda_2(\Lambda_1 + \Lambda_4)[(5m-m^3)A_1 + (-3m-m^3)\overline{A}_1] + 12\Lambda_2(\Lambda_1 + \Lambda_4)m^2(A_3 + \overline{A}_3) \\ &+ \Lambda_1(1-m^2)(D_2 + \overline{D}_2) + 4\Lambda_1 m(-D_4 + \overline{D}_4), \\ g_1 &= 14\Lambda_2(\Lambda_1 + \Lambda_4)mA_2 + 6\Lambda_2(\Lambda_1 + \Lambda_4)m^2\overline{A}_2 - 20\Lambda_2(\Lambda_1 + \Lambda_4)m^2A_4 \\ &+ 2\Lambda_1 D_3 + 3\Lambda_1 m\overline{D}_3 - 5\Lambda_1 mD_5, \\ g_2 &= -6\Lambda_2(\Lambda_1 + \Lambda_4)m^2A_2 + \Lambda_2(\Lambda_1 + \Lambda_4)(-10m-4m^3)\overline{A}_2 + 20\Lambda_2(\Lambda_1 + \Lambda_4)m^2\overline{A}_4 \\ &- 3\Lambda_1 mD_3 - 2\Lambda_1 m^2\overline{D}_3 + 5\Lambda_1 m\overline{D}_5, \\ g_3 &= -\frac{1}{2}\tau^0 m(1-m^2) + \Lambda_2(\Lambda_1 + \Lambda_4)(m-m^3)A + \Lambda_1(3+m^2)\overline{D}_0 \\ &+ \Lambda_2(\Lambda_1 + \Lambda_4)[(-3+m^2)A_1 + 2m^2\overline{A}_1 + (27m+3m^3)A_3 - 30m^2A_5] \\ &+ 2\Lambda_1 m(D_2 + \overline{D}_2) + \Lambda_1(3+m^2)D_4 - 6\Lambda_1 mD_6, \\ g_4 &= -\frac{1}{2}\tau^0 m(1-m^2) + \Lambda_2(\Lambda_1 + \Lambda_4)(3m^3-3m)A - \Lambda_1(1+3m^2)D_0 \\ &+ \Lambda_2(\Lambda_1 + \Lambda_4)[-2m^2A_1 + (1+m^2)\overline{A}_1 + (-21m-9m^3)\overline{A}_3 + 30m^2\overline{A}_5] \\ &- 2\Lambda_1 mD_2 - 2\Lambda_1 m\overline{D}_2 + \Lambda_1(-1-3m^2)\overline{D}_4 + 6\Lambda_1 m\overline{D}_6, \end{aligned}$$

$$\begin{aligned}
g_5 &= \Lambda_2(\Lambda_1 + \Lambda_4) [(-8 - 2m^2)A_2 + (44m + 8m^3)A_4 - 42m^2A_6] \\
&\quad + \Lambda_1 m D_3 + \Lambda_1(4 + 2m^2)D_5 - 7\Lambda_1 m D_7, \\
g_6 &= \Lambda_2(\Lambda_1 + \Lambda_4) [(4 + 6m^2)\bar{A}_2 + (-36m - 16m^3)\bar{A}_4 + 42m^2\bar{A}_6] \\
&\quad - \Lambda_1 m \bar{D}_3 + \Lambda_1(-2 - 4m^2)\bar{D}_5 + 7\Lambda_1 m \bar{D}_7, \\
S_n &= \Lambda_2(\Lambda_1 + \Lambda_4) [m(n - n^2)\bar{A}_n + (n + 2)[n + 2 + (2n + 3)m^2]\bar{A}_{n+2}] \\
&\quad + \Lambda_2(\Lambda_1 + \Lambda_4) \{ (n + 4)[m + m^3 - (n + 5)(2m + m^3)]\bar{A}_{n+4} + (n + 6)(n + 7)m^2\bar{A}_{n+6} \} \\
&\quad + \Lambda_1(n - 1)m\bar{D}_{n+3} + \Lambda_1[3 + m^2 - (n + 5)(1 + m^2)]\bar{D}_{n+5} + \Lambda_1(n + 7)m\bar{D}_{n+7}, \\
T_n &= \Lambda_2(\Lambda_1 + \Lambda_4) [(n^2 - n)mA_n - (n + 2)(2nm^2 + m^2 + n + 4)A_{n+2}] \\
&\quad + \Lambda_2(\Lambda_1 + \Lambda_4) [(n + 4)(nm^3 + 2m^3 + 2nm + 11m)A_{n+4} - (n + 6)(n + 7)m^2A_{n+6}] \\
&\quad + \Lambda_1(1 - n)mD_{n+3} + \Lambda_1[(n + 5)(1 + m^2) - (1 + 3m^2)]D_{n+5} - \Lambda_1(n + 7)mD_{n+7}, \tag{A.6}
\end{aligned}$$

$$\begin{aligned}
h_0 &= \frac{1}{2} [\tau^0 + 8(\Lambda_5 + \Lambda_6)\mu_1 R \varepsilon^*] (1 - m^4) + \Lambda_6 [4m(O_0 - \bar{O}_0) + (1 - m^2)(P_2 + \bar{P}_2) + 4m(\bar{P}_4 - P_4)] \\
&\quad + \Lambda_7(\Lambda_5 + \Lambda_6) [(1 - 5m^2)E_1 + (1 + 3m^2)\bar{E}_1 + 12m(E_3 - \bar{E}_3)] \\
&\quad + \Lambda_7(\Lambda_5 + \Lambda_6) [(5m - m^3)F_1 + (-3m - m^3)\bar{F}_1 + 12m^2(\bar{F}_3 - F_3)], \\
h_1 &= -5\Lambda_6 m \bar{O}_1 + 3\Lambda_6 m P_1 + 2\Lambda_6 \bar{P}_1 + 2\Lambda_6 P_3 + 3\Lambda_6 m \bar{P}_3 - 5\Lambda_6 m P_5 \\
&\quad + \Lambda_7(\Lambda_5 + \Lambda_6) [6mE_2 + (4 + 10m^2)\bar{E}_2 - 20m\bar{E}_4] \\
&\quad + \Lambda_7(\Lambda_5 + \Lambda_6) (14mF_2 + 6m^2\bar{F}_2 - 20m^2F_4), \\
h_2 &= 5\Lambda_6 m O_1 - 2\Lambda_6 m^2 P_1 - 3\Lambda_6 m \bar{P}_1 - 3\Lambda_6 m P_3 - 2\Lambda_6 m^2 \bar{P}_3 + 5\Lambda_6 m \bar{P}_5 \\
&\quad - \Lambda_7(\Lambda_5 + \Lambda_6) (14m^2 E_2 + 6m\bar{E}_2 - 20mE_4) \\
&\quad + \Lambda_7(\Lambda_5 + \Lambda_6) [-6m^2 F_2 + (-10m - 4m^3)\bar{F}_2 + 20m^2 \bar{F}_4], \\
h_3 &= -\frac{1}{2} m (1 - m^2) [\tau^0 + 8(\Lambda_6 + \Lambda_5)\mu_1 R \varepsilon^*] + \Lambda_6 (3 + m^2) \bar{O}_0 - 6\Lambda_6 m \bar{O}_2 \\
&\quad + 2\Lambda_6 m (P_2 + \bar{P}_2) + \Lambda_6 (3 + m^2) P_4 - 6\Lambda_6 m P_6 \\
&\quad + \Lambda_7(\Lambda_5 + \Lambda_6) [2mE_1 - (m + m^3)\bar{E}_1 + (3 + 9m^2)\bar{E}_3 - 30m\bar{E}_5] \\
&\quad + \Lambda_7(\Lambda_5 + \Lambda_6) [(-3 + m^2)F_1 + 2m^2\bar{F}_1 + (27m + 3m^3)F_3 - 30m^2F_5], \\
h_4 &= -\frac{1}{2} m (1 - m^2) [\tau^0 + 8(\Lambda_6 + \Lambda_5)\mu_1 R \varepsilon^*] - \Lambda_6 (1 + 3m^2) O_0 + 6\Lambda_6 m O_2
\end{aligned}$$

$$\begin{aligned}
& -2\Lambda_6 m(P_2 + \bar{P}_2) - \Lambda_6(1 + 3m^2)\bar{P}_4 + 6\Lambda_6 m\bar{P}_6 \\
& + \Lambda_7(\Lambda_5 + \Lambda_6) \left[(3m^3 - m)E_1 - 2m\bar{E}_1 - (3 + 27m^2)E_3 + 30mE_5 \right] \\
& + \Lambda_7(\Lambda_5 + \Lambda_6) \left[-2m^2F_1 + (1 + m^2)\bar{F}_1 - (21m + 9m^3)\bar{F}_3 + 30m^2\bar{F}_5 \right], \\
h_5 = & \Lambda_6(4 + 2m^2)\bar{O}_1 - 7\Lambda_6 m\bar{O}_3 + \Lambda_6 m\bar{P}_1 + \Lambda_6 mP_3 + \Lambda_6(4 + 2m^2)P_5 - 7\Lambda_6 mP_7 \\
& - \Lambda_7(\Lambda_5 + \Lambda_6) \left[(6m + 4m^3)\bar{E}_2 - (16 + 36m^2)\bar{E}_4 + 42m\bar{E}_6 \right] \\
& + \Lambda_7(\Lambda_5 + \Lambda_6) \left[(-8 + 2m^2)F_2 + (44m + 8m^3)F_4 - 42m^2F_6 \right], \\
h_6 = & -\Lambda_6(2 + 4m^2)O_1 + 7\Lambda_6 mO_3 - \Lambda_6 mP_1 - \Lambda_6 m\bar{P}_3 - \Lambda_6(2 + 4m^2)\bar{P}_5 + 7\Lambda_6 m\bar{P}_7 \\
& + \Lambda_7(\Lambda_6 + \Lambda_5) \left[(2m + 8m^3)E_2 - (8 + 44m^2)E_4 + 42mE_6 \right] \\
& + \Lambda_7(\Lambda_6 + \Lambda_5) \left[(4 + 6m^2)\bar{F}_2 - (36m + 16m^3)\bar{F}_4 + 42m^2\bar{F}_6 \right], \\
h_7 = & \Lambda_6(5 + 3m^2)\bar{O}_2 - 8\Lambda_6 m\bar{O}_4 + \Lambda_6(5 + 3m^2)P_6 - 8\Lambda_6 mP_8 \\
& + \Lambda_7(\Lambda_6 + \Lambda_5) \left[-(15m + 9m^3)\bar{E}_3 + (25 + 55m^2)\bar{E}_5 - 56m\bar{E}_7 \right] \\
& + \Lambda_7(\Lambda_6 + \Lambda_5) \left[-(15 + 9m^2)F_3 + (65m + 15m^3)F_5 - 56m^2F_7 \right], \\
h_8 = & -\Lambda_6(3 + 5m^2)O_2 + 8\Lambda_6 mO_4 - \Lambda_6(3 + 5m^2)\bar{P}_6 + 8\Lambda_6 m\bar{P}_8 \\
& + \Lambda_7(\Lambda_6 + \Lambda_5) \left[(9m + 15m^3)E_3 - (15 + 65m^2)E_5 + 56mE_7 \right] \\
& + \Lambda_7(\Lambda_6 + \Lambda_5) \left[(9 + 15m^2)\bar{F}_3 - (55m + 25m^3)\bar{F}_5 + 56m^2\bar{F}_7 \right], \\
U_n = & n\Lambda_6 mO_n - \Lambda_6 \left[n + 3 + (n + 5)m^2 \right] O_{n+2} + (n + 8)\Lambda_6 mO_{n+4} \\
& + n\Lambda_6 m\bar{P}_{n+4} - \Lambda_6 \left[n + 3 + (n + 5)m^2 \right] \bar{P}_{n+6} - (n + 8)\Lambda_6 m\bar{P}_{n+8} \\
& - n(n + 1)\Lambda_7(\Lambda_6 + \Lambda_5)m^2 E_{n+1} + \Lambda_7(\Lambda_6 + \Lambda_5)(n + 3) \left[(2n + 3)m + (n + 5)m^2 \right] E_{n+3} \\
& - \Lambda_7(\Lambda_6 + \Lambda_5)(n + 5) \left[n + 3 + (2n + 13)m^2 \right] E_{n+5} + (n + 7)(n + 8)\Lambda_7(\Lambda_6 + \Lambda_5)mE_{n+7} \\
& - n(n + 1)\Lambda_7(\Lambda_6 + \Lambda_5)m\bar{F}_{n+1} + \Lambda_7(\Lambda_6 + \Lambda_5)(n + 3) \left[n + 3 + (2n + 5)m^2 \right] \bar{F}_{n+3} \\
& + \Lambda_7(\Lambda_6 + \Lambda_5) \left\{ -(n + 5) \left[(2n + 11)m + (n + 5)m^3 \right] \bar{F}_{n+5} + (n + 7)(n + 8)m^2 \bar{F}_{n+7} \right\}, \\
V_n = & -n\Lambda_6 m\bar{O}_n + \Lambda_6 \left[n + 3 + (n + 3)m^2 \right] \bar{O}_{n+2} - (n + 8)\Lambda_6 m\bar{O}_{n+4} \\
& - n\Lambda_6 mP_{n+4} + \Lambda_6 \left[n + 5 + (n + 3)m^2 \right] P_{n+6} - (n + 8)\Lambda_6 mP_{n+8} \\
& + n(n + 1)\Lambda_7(\Lambda_6 + \Lambda_5)m^2 \bar{E}_{n+1} - \Lambda_7(\Lambda_6 + \Lambda_5)(n + 3) \left[(2n + 5)m + (n + 3)m^2 \right] \bar{E}_{n+3} \\
& - \Lambda_7(\Lambda_6 + \Lambda_5)(n + 5) \left[n + 5 + (2n + 11)m^2 \right] \bar{E}_{n+5} - (n + 7)(n + 8)\Lambda_7(\Lambda_6 + \Lambda_5)m\bar{E}_{n+7}
\end{aligned}$$

$$\begin{aligned}
& +n(n+1)\Lambda_7(\Lambda_6+\Lambda_5)mF_{n+1}-\Lambda_7(\Lambda_6+\Lambda_5)(n+3)[n+5+(2n+3)m^2]F_{n+3} \\
& +\Lambda_7(\Lambda_6+\Lambda_5)\{(n+5)[(2n+13)m+(n+3)m^3]F_{n+5}-(n+7)(n+8)m^2F_{n+7}\}. \quad (\text{A.7})
\end{aligned}$$

Appendix B

In the (x_1, x_2) -coordinate system, the equation of ellipse is:

$$\frac{x_1^2}{a^2} + \frac{x_2^2}{b^2} = 1, \quad (\text{B.1})$$

where a and b are the semi-axes of the ellipse.

Write the variable x_2 and its derivatives with respect to x_1 as a function of x_1 and x_2 in the first quadrant:

$$x_2 = b\sqrt{1 - \frac{x_1^2}{a^2}}, \quad x_2' = -\frac{b^2}{a^2} \frac{x_1}{x_2}, \quad x_2'' = -\frac{b^4}{a^2} \frac{1}{x_2^3}. \quad (\text{B.2})$$

Thereafter, the curvature can be written as:

$$\frac{1}{R_0} = \frac{|x_2''|}{(1+x_2'^2)^{3/2}} = \frac{\left| \frac{b^4}{a^2} \frac{1}{x_2^3} \right|}{\left(1 + \frac{b^4}{a^4} \frac{x_1^2}{x_2^2} \right)^{3/2}}. \quad (\text{B.3})$$

Note that

$$x_1 = \frac{z+\bar{z}}{2}, \quad x_2 = \frac{z-\bar{z}}{2i}, \quad a = R(1+m), \quad b = R(1-m), \quad z = R\left(\xi + \frac{m}{\xi}\right). \quad (\text{B.4})$$

The curvature is expressed in terms of the complex variable ξ as follows:

$$\frac{1}{R_0} = \frac{8b^4}{a^2} \frac{1}{\left[(z-\bar{z})^2 - \frac{b^4}{a^4} (z+\bar{z})^2 \right]^{3/2}} = \frac{(1-m^2)}{R} \frac{1}{|m'(\xi)/R|^3}. \quad (\text{B.5})$$

Appendix C

For any integer k ,

$$\begin{aligned}
\int_0^{2\pi} (1+b^* \sin^2 \theta)^{-3/2} \sin(k\theta) d\theta &= 0, \\
\int_0^{2\pi} (1+b^* \sin^2 \theta)^{-3/2} \cos(2k+1)\theta d\theta &= 0. \quad (\text{C.1})
\end{aligned}$$

Therefore,

$$\begin{aligned}
& \int_0^{2\pi} (1+b^* \sin^2 \theta)^{-3/2} \cos[2(k+1)\theta] d\theta \\
&= \int_0^{2\pi} (1+b^* \sin^2 \theta)^{-3/2} [\cos 2k\theta \cos 2\theta - \sin 2k\theta \sin 2\theta] d\theta \\
&= \int_0^{2\pi} (1+b^* \sin^2 \theta)^{-3/2} \cos 2k\theta \cos 2\theta d\theta - \frac{4k}{b^*} \int_0^{2\pi} (1+b^* \sin^2 \theta)^{-3/2} (1+b^* \sin^2 \theta) \cos 2k\theta d\theta \\
&= \frac{1+2k}{2} \int_0^{2\pi} (1+b^* \sin^2 \theta)^{-3/2} [\cos 2(k+1)\theta + \cos 2(k-1)\theta] d\theta \\
&\quad - \frac{4k+2kb^*}{b^*} \int_0^{2\pi} (1+b^* \sin^2 \theta)^{-3/2} \cos(2k\theta) d\theta. \tag{C.2}
\end{aligned}$$

Now define

$$I_{2k} = \frac{1}{2\pi} \int_0^{2\pi} (1+b^* \sin^2 \theta)^{-3/2} \cos(2k\theta) d\theta, \tag{C.3}$$

which leads to the relation $I_{2k} = I_{-2k}$, and Eq. (C.2) becomes

$$I_{2(k+1)} = \frac{1+2k}{2} (I_{2(k+1)} + I_{2(k-1)}) - \frac{4k+2kb^*}{b^*} I_{2k}. \tag{C.4}$$

Using the Fourier series in the complex form,

$$(1+b^* \sin^2 \theta)^{-3/2} = I_0 + \sum_{k=1}^{\infty} I_{2k} (e^{i2k\theta} + e^{-i2k\theta}). \tag{C.5}$$

For a large integer k , the right-hand side of Eq. (C.5) approaches a geometric series. To find the ratio of this geometric series, assume that for large k ,

$$\frac{I_{2(k+1)}}{I_{2k}} = \eta. \tag{C.6}$$

For large k , Eq. (C.4) can be approximately reduced to:

$$0 = I_{2(k+1)} + I_{2(k-1)} - \frac{4+2b^*}{b^*} I_{2k}.$$

Combined with Eq. (C.6), the above expression leads to

$$0 = \eta^2 + 1 - \frac{4+2b^*}{b^*} \eta. \tag{C.7}$$

Noting the expression for b^* in Eq. (3.40), the solution of Eq. (C.7) is

$$\eta = \frac{2+b^*}{b^*} - \sqrt{\left(\frac{2+b^*}{b^*}\right)^2 - 1} = m < 1, \quad (\text{C.8})$$

which implies that the geometric series is convergent. Now rewrite Eq. (C.5) as:

$$(1+b^* \sin^2 \theta)^{-3/2} = I_0 + \sum_{k=1}^{J-1} I_{2k} (e^{i2k\theta} + e^{-i2k\theta}) + \sum_{k=0}^{\infty} I_{2(J+k)} [e^{i2(J+k)\theta} + e^{-i2(J+k)\theta}]$$

and consider the third term on the right-hand side as a geometric series for large integer J (approximately). Therefore,

$$\begin{aligned} (1+b^* \sin^2 \theta)^{-3/2} &\cong I_0 + \sum_{k=1}^{J-1} I_{2k} (e^{i2k\theta} + e^{-i2k\theta}) + I_{2J} \left[\frac{e^{i2J\theta}}{1-me^{i2\theta}} + \frac{e^{-i2J\theta}}{1-me^{-i2\theta}} \right] \\ &= I_0 + \sum_{k=1}^{J-1} I_{2k} (e^{i2k\theta} + e^{-i2k\theta}) + I_{2J} \frac{e^{i2J\theta} + e^{-i2J\theta} - m[e^{i2(J-1)\theta} + e^{i2(1-J)\theta}]}{(1-me^{i2\theta})(1-me^{-i2\theta})}. \end{aligned} \quad (\text{C.9})$$

Appendix D

Consider the following equations ($|\xi| = 1$):

$$\frac{1}{1-me^{\pm i2\theta}} = \sum_{n=0}^{\infty} (me^{\pm i2\theta})^n, \quad \frac{1}{m(\xi)/R} = \frac{1}{1-me^{-i2\theta}} = \sum_{n=0}^{\infty} (me^{-i2\theta})^n. \quad (\text{D.1})$$

Therefore,

$$\begin{aligned} &\frac{1}{m(\xi)/R} \frac{1}{(1-me^{i2\theta})(1-me^{-i2\theta})} \\ &= \sum_{n=0}^{\infty} (me^{-i2\theta})^n \sum_{n=0}^{\infty} (me^{i2\theta})^n \sum_{n=0}^{\infty} (me^{-i2\theta})^n \\ &= \sum_{n=0}^{\infty} (me^{-i2\theta})^n \frac{1}{1-m^2} \left[\sum_{n=1}^{\infty} (me^{-i2\theta})^n + \sum_{n=0}^{\infty} (me^{i2\theta})^n \right] \\ &= \frac{1}{1-m^2} \left\{ \sum_{n=1}^{\infty} n(me^{-i2\theta})^n + \frac{1}{1-m^2} \left[\sum_{n=1}^{\infty} (me^{-i2\theta})^n + 1 + \sum_{n=1}^{\infty} (me^{i2\theta})^n \right] \right\} \\ &= \frac{1}{(1-m^2)^2} \left\{ \sum_{n=1}^{\infty} [m^n + (1-m^2)nm^n] e^{-i2n\theta} + 1 + \sum_{n=1}^{\infty} (me^{i2\theta})^n \right\}. \end{aligned} \quad (\text{D.2})$$